Implementation of a Universal Fine-Structure Splitting Eraser for Quantum Dots

by

Maeve Wentland

A thesis
presented to the University of Waterloo
in fulfillment of the
thesis requirement for the degree of
Master of Science
in
Physics (Quantum Information)

Waterloo, Ontario, Canada, 2023

© Maeve Wentland 2023

Author's Declaration

I hereby declare that I am the sole author of this thesis. This is a true copy of the thesis, including any required final revisions, as accepted by my examiners.

I understand that my thesis may be made electronically available to the public.

Abstract

Entangled photons are an important resource for different applications in quantum computation, quantum information, and quantum communication. Sources based on semiconductor quantum dots have successfully obtained on-demand, highly entangled photon pairs with a high repetition rate. However, the fidelity of the photon pair to a Bell state is reduced due to fine structure splitting (FSS) in the exciton state of the biexciton-exciton cascade. The FSS causes the exciton to precess during its lifetime resulting in a time-dependent entangled state which, when larger than the linewidth of a photon ($\approx$1 μeV), can reveal 'which-path' information for the exciton and biexciton cascade. A detector with a small timing jitter can resolve the dynamics of the entangled photon states. Real-world applications make it desirable to remove the FSS. Current techniques to remove the FSS include applying a strain, electric, or magnetic field. These techniques require post-processing of QD sources and are difficult to implement in conjunction with nanostructures such as nanowires or micropillar cavities. Here, we present an all-optical method of removing the FSS, which requires no post-processing of the source and works for any quantum dot sources. We propose frequency shifting single photons by emulating a fast-rotating half-waveplate using an electro-optical lithium niobate waveguide. In this thesis we show this method is capable of frequency shifting photons with high efficiency (88.4%). We also examine how the efficiency is affected by the frequency that we are shifting by, and how the the set-up performs when operating over an extended period of time. We also examine several electro-optical devices to see if their behaviour is consistent and predictable.

In this thesis we also examine the building blocks for implementing a quantum circuit using entangled photons on a silicon nitride chip. These chips can be used instead of traditional free-space optics which take up a significant footprint, make it challenging to switch between experiments, and face losses because of coupling inefficiencies and attentuation. Silicon nitride is a low-loss waveguide material that, unlike the more traditional silicon, allows for the transmission of near-infrared photons. However, the newer material doesn't have significant libraries of pre-built components that can be used to create larger circuits. We examine the process of simulating, building, and integrating two of these components into a open-source library. This is the start of a process of integrating quantum dot entangled sources with building scalable quantum systems.

Acknowledgements

I want to thank everyone who supported me as I completed this thesis. First, my supervisor, Dr. Micheal Reimer, who provided me with the knowledge, tools and time to complete this work with its many unexpected turns. A special thanks goes to Sonell Malik, who worked alongside me in the lab. Also, to everyone in the quantum photonic devices group who helped make this project progress: Brady Cunard, Sayan Gangopadhyay, Jack deGooyer, Matteo Pennechietti, Nachiket Sherlekar, Lin Tian, and Sasan Vosoogh-Grayli.

I would also like to thank my friends and family, both here in Ontario and elsewhere, who cheered me on and kept me sane. Finally, the biggest thank you to my family: Paula, Craig, Emma and Babbage for their unfailing support in anything I put my mind to.

Table of Contents

List of Figures

List of Tables

List of Abbreviations

AC	Alternating Current
ANT	Applied Nanotools
CCW	Counter-Clockwise
CMC	Canadian Microsystems
CML	Compact Model Library
CW	Clockwise
DAC	Digital to Analog Converter
DC	Direct Current
EF	Entanglement of Formation
EOM	Electro-Optic Modulator
FSS	Fine-Structure Splitting
GDS	Graphic Data System
HWP	Half-Wave Plate
LCP	Left-Circularly Polarized
$LiNbO_3$	Lithium Niobate
N_{eff}	Effective Index
N_g	Group Index
NMR	Nuclear Magnetic Resonance
PBS	Polarizing Beam Splitter
PDK	Personal Development Kit
QD	Quantum Dot

QWP	Quarter-Wave Plate
RCP	Right-Circularly Polarized
RF	Radio Frequency
SAM	Spin Angular Momentum
SiN	Silicon Nitride
SiO_2	Silicon Dioxide
SPDC	Spontaneous Parametric Down-Conversion
TE	Transverse Electric
TM	Transverse Magnetic
X	Exciton
XX	Biexciton
ZnO	Zinc Oxide

Chapter 1

Introduction

The properties of light have been a source of scientific study and fascination as early as ancient Greece [7]. The debate between light being a particle or a wave was sparked in the 18th century between Newton and Huygens [8] and was not resolved until Einstein's seminal paper on the quantized property of light was published in 1905 [9]. Einstein, along with Rosen and Podolsky, continued to describe the theory behind entanglement, which initiated the study of quantum mechanics [10]. The theory was controversial at the time; Einstein himself was not satisfied with the explanation, notably saying, "God does not play dice with the universe"[11]. Schrödinger also wrote about the perceived problems of the Copenhagen explanation of quantum phenomena with his famous thought experiment featuring an ill-fated cat [12]. However, the study persisted, and eventually, the sub-field of of quantum information was born out of the desire to utilize the strange behaviour. Early implementations of quantum systems relied on the use of nuclear magnetic resonance (NMR) as it was an established field where we could easily exert control over nuclei [13]. As the field expanded, the search for the optimal qubit expanded. Researchers began to examine superconducting circuits [14], trapped ions [15], and photons as options for perfect qubits. This thesis will examine why photons could be the ideal qubit and some nuances of implementing a photonic quantum computer.

1.1 Quantum Information

The field of quantum information uses quantum mechanics to study how information can be transmitted, transformed and analyzed. In this thesis, we will examine the smallest unit of quantum information, the qubit. Just as classical computers use a single unit of

information, known as a bit, to perform computation, quantum computers use a qubit as their smallest unit of information. We can use these qubits to solve a different class of problems than was accessible before; some notable examples include breaking RSA [16] and securely creating crypographic keys [17]. Like a classical bit, a qubit is a two-state system that can be used to describe a 0 or a 1, which in quantum computing are represented by the orthogonal eigenvectors, $|0\rangle$ and $|1\rangle$.

$$|0\rangle = \begin{bmatrix} 1 \\ 0 \end{bmatrix} \qquad |1\rangle = \begin{bmatrix} 0 \\ 1 \end{bmatrix} \tag{1.1}$$

Like a classical bit, when one of these states is measured, they will always yield the same output: $|0\rangle$ will output 0 and $|1\rangle$ will output 1. Unlike classical bits, qubits can exist in a superposition. A superposition is a linear combination of the two basis states written as $|\psi\rangle = \alpha\,|0\rangle + \beta\,|1\rangle$. A qubit will exist in this state until measured, at which point the output will be either 0 or 1 with a probability of $|\alpha|^2$ or $|\beta|^2$, respectively. For example, the state described in Equation 1.2 will have a 64% chance of giving a 0 result and a 36% chance of measuring as a 1.

$$|\psi_0\rangle = 0.8\,|0\rangle + 0.6\,|1\rangle \tag{1.2}$$

Since every measurement can only produce one result all states have to be normalized so $|\alpha|^2+|\beta|^2 = 1$. Once the measurement has taken place, the wave function collapses, and the qubit becomes the state that we measured, with trace of the superposition state remaining. This means we have no way of obtaining any other information on a superposition state once it has been measured. If we have multiple identical versions of the state, we can estimate what the state might have been by measuring all of them. For example, if we measure Equation 1.2 once and get a 1, that only tells us that $\beta \neq 0$. However, measuring ten versions of the same state and getting three 1s and seven 0s, tells us that the state could be $|\psi_1\rangle = \sqrt{0.7}\,|0\rangle + \sqrt{0.3}\,|1\rangle$ which is close to the actual state. The more measurements we take the more accurate our estimate of the state will be.

Single qubits can exist anywhere in a two-dimensional complex Hilbert space spanned by $|0\rangle$ and $|1\rangle$, meaning α and β can also be complex numbers. An $e^{i\theta}$ phase difference can exist between $|0\rangle$ and $|1\rangle$. This phase difference does not impact the measured result, as $|e^{i\theta}\alpha|^2 = |\alpha|^2$, but the phase difference can be utilized in quantum logic gates. The phases of qubits in a superposition can interfere, increasing the probability that the desired state is measured after a quantum operation is performed.

1.1.1 Entanglement

We have examined the behaviour of single qubits, but quantum algorithms require multiple qubits to interact. Multi-qubit states can exist as linear combinations of states; an example is shown in Equation 1.3.

$$|\Psi_0\rangle = 0.8\,|01\rangle + 0.6\,|11\rangle = (0.8\,|0\rangle + 0.6\,|1\rangle) \otimes |1\rangle \tag{1.3}$$

We can observe from this example two of the four possible basis states of a two-qubit system, $|01\rangle$ and $|11\rangle$. The other two basis states are $|00\rangle$ and $|10\rangle$. These four vectors span the four-dimensional complex Hilbert space that can represent all two-qubit states. The state in Equation 1.3 represents a separable state where one qubit is in the state described by Equation 1.2 and the other is in the basis state $|1\rangle$. A separable state is any state where the state of each qubit can be described individually or by $|\Psi\rangle = |\psi_0\rangle \otimes |\psi_1\rangle$ where $\otimes$ is the tensor product. Within the Hilbert space, there is also a set of states that cannot be written as the tensor product of two qubits. These states are called entangled because we cannot describe one qubit without considering the other. An example of an entangled state is Equation 1.4.

$$|\phi^+\rangle = \frac{1}{\sqrt{2}}\left(|00\rangle + |11\rangle\right) \tag{1.4}$$

Equation 1.4 is one of the maximally entangled states called the Bell states. The other three are described by Equations 1.5, 1.6, and 1.7.

$$|\phi^-\rangle = \frac{1}{\sqrt{2}}\left(|00\rangle - |11\rangle\right) \tag{1.5}$$

$$|\psi^+\rangle = \frac{1}{\sqrt{2}}\left(|01\rangle + |10\rangle\right) \tag{1.6}$$

$$|\psi^-\rangle = \frac{1}{\sqrt{2}}\left(|01\rangle - |10\rangle\right) \tag{1.7}$$

These states are considered maximally entangled because they are the most different from the four basis states. Bell states are important for implementing superdense coding [18], quantum key distribution [17], and quantum teleportation [19]. This maximally entangled quality makes them very important for quantum computing for a number of

interesting results that come from measuring entangled states. If we take an entangled state and physically separate the two photons by a great distance. We can measure one and instantly gain information on what the other qubit is, allowing perfectly correlated information to be transferred over large distances in a way that classical computing cannot replicate. For example, if we give Alice and Bob each a qubit from the entangled state $|\psi^+\rangle$ when Alice measures her qubit as a 0, Bob can only get a 1 when he measures, and both parties know what the other person measured without any other information. In the same situation with the separable state $|\Phi\rangle = \frac{1}{\sqrt{2}}(|11\rangle + |10\rangle)$, if Alice measures a 1, Bob still has an equal chance of measuring a 1 or a 0, giving Alice no information. Another important aspect of the Bell states is that the probability of measuring either state is equal meaning we have access to a source of true randomness that cannot be easily replicated.

Both the separable and entangled states we have examined so far are what can be described as pure states, meaning they can be described using a single state. However, there are also mixed states, which describe the probabilities of a qubit being in one of a set of initial states. An example is shown in Equation 1.8.

$$|\Psi_1\rangle = \begin{cases} |00\rangle \, \mathrm{P} = 0.5 \\ |11\rangle \, \mathrm{P} = 0.5 \end{cases} \tag{1.8}$$

While this state may look the same as the Bell state $|\phi^+\rangle$, it is not actually entangled. We do need a way to describe both of these states mathematically that can represent the difference between them. For this, we use an $n \times n$ density matrix to represent both pure and mixed states of any number of qubits. A density matrix is defined as:

$$\rho = \sum_{m}^{i=1} \mathrm{P}_i \, |\phi_i\rangle \, \langle\phi_i| \tag{1.9}$$

where m is the number of initial states, in the case of a pure state $m = 1$, using this process, we can calculate the density matrix of both $|\phi^+\rangle$ (Equation 1.10) and Equation 1.8 (Equation 1.11) to determine that they are different.

$$\rho_{\phi^+} = \frac{1}{2} \begin{bmatrix} 1 & 0 & 0 & 1 \\ 0 & 0 & 0 & 0 \\ 0 & 0 & 0 & 0 \\ 1 & 0 & 0 & 1 \end{bmatrix} \tag{1.10}$$

$$\rho_{\Psi_1} = \frac{1}{2}\begin{bmatrix} 1 & 0 & 0 & 0 \\ 0 & 0 & 0 & 0 \\ 0 & 0 & 0 & 0 \\ 0 & 0 & 0 & 1 \end{bmatrix} \tag{1.11}$$

The two states differ in their anti-diagonal elements, which can not be determined when measuring only in the $|0\rangle$ and $|1\rangle$ basis. However, we can reconstruct the complete density matrix using quantum state tomography.

1.1.2 Measuring Entanglement

Having established why entanglement is so important, we need a way to measure it. For a two-qubit system, entanglement is measured using the entanglement of formation (EF) [20]. For a pure state $|\Psi\rangle$, this is defined as:

$$EF = -Tr[\rho_\Psi \log(\rho_\Psi)]. \tag{1.12}$$

EF will be a value between 1 and 0, with 0 being a completely separable state and 1 being a maximally entangled state. EF can be written in terms of the concurrence, where concurrence is defined by:

$$C(\Psi_A) = |\langle\Psi|\tilde{\Psi}\rangle|. \tag{1.13}$$

where $|\tilde{\Psi}\rangle$ is a spin flip transformation to a pure state, defined as $\sigma_y|\Psi^*\rangle$ [20]. This changes the EF equation to:

$$E(C) = h\left(\frac{1+\sqrt{1-C^2}}{2}\right), \tag{1.14}$$

$$h(x) = -x\log_2(x) - (1-x)\log_2(1-x). \tag{1.15}$$

$E(C)$ monotonically increases from 0 to 1 as C increases from 0 to 1. This correlation means we can use concurrence as its own measure of entanglement. The definition of concurrence given by Equation 1.13 only covers pure states. The concurrence of a mixed state is given by:

$$C(\rho_A) = \max\{0, \lambda_1 - \lambda_2 - \lambda_3 - \lambda_4\}, \tag{1.16}$$

where λ_i are the eigenvalues of the Hermitian matrix $\sqrt{\sqrt{\rho}\tilde{\rho}\sqrt{\rho}}$. $\tilde{\rho}$ is the spin flip transformation to a mixed state, given by $(\sigma_y \otimes \sigma_y)\rho^*(\sigma_y \otimes \sigma_y)$ [20]. Since calculating the concurrence of a state is significantly easier to calculate than the EF, it is commonly used as the measure of entanglement. Frequently, we do not just want any state with a high concurrence and instead want one to be in a specific maximally entangled state. To determine this, we can examine a state's fidelity to a reference maximally entangled state. Fidelity is given by:

$$F(\rho) = Tr[\rho\rho_0], \tag{1.17}$$

where ρ_0 is the density of the maximally entangled state. The fidelity of a state ρ with a concurrence $C(\rho)$ has a fidelity bounded by [21]:

$$\max\left(\frac{1+C}{4}, C\right) \leq F \leq \frac{1+C}{2}, \tag{1.18}$$

meaning that the fidelity of a two-qubit state will be between 0.25 and 1 and always be greater than or equal to the concurrence.

1.2 Photons as Qubits

This thesis aims to show how photons can be used as qubits, meaning we must examine how they can act as information carriers. Photons are used to transmit classical information through the phase or amplitude of the light, they can be transmitted quickly over long distances with minimal loss using fibre-optic cables or used to process information on silicon chips efficiently. There are several degrees of freedom which we can exploit to encode quantum information, including the spatial mode, frequency, time, and polarization of a photon. In this thesis, we will examine the polarization degree of freedom.

1.2.1 Polarization

Polarization describes the orientation of the electric field of a single photon. There are six base polarizations a photon can exist in that are defined by their relation to the laboratory

frame. If the electric field is oscillating along the x-direction of the laboratory frame, the photon is considered to be in the $|H\rangle$ polarization; if it is oscillating along the y-direction, it is in the $|V\rangle$ polarization. These states are orthogonal and are usually defined as our basis states, $|0\rangle$ and $|1\rangle$ respectively.

$$|H\rangle = |0\rangle = \begin{bmatrix} 1 \\ 0 \end{bmatrix} \qquad |V\rangle = |1\rangle = \begin{bmatrix} 0 \\ 1 \end{bmatrix} \tag{1.19}$$

If we could look at these polarizations from the z-axis, the electric field would appear to be oscillating in a line along the axis, which is why we call these linear polarizations.

We know that qubits need to be able to exist in a superposition between $|0\rangle$ and $|1\rangle$. A superposition where α and β are equal in magnitude and phase can be described by the diagonal polarization, $|D\rangle$, where the electric field oscillates in a line $+45°$ between the x and y axes. Similarly, the anti-diagonal polarization where the electric field oscillates -45° between the x and y axes, $|A\rangle$, describes a superposition with α and β in equal phase but opposite magnitude. These polarizations are also considered linear polarizations.

$$|D\rangle = \frac{1}{\sqrt{2}}\left(|0\rangle + |1\rangle\right) = \frac{1}{\sqrt{2}}\begin{bmatrix} 1 \\ 1 \end{bmatrix} \qquad |A\rangle = \frac{1}{\sqrt{2}}\left(|0\rangle - |1\rangle\right) = \frac{1}{\sqrt{2}}\begin{bmatrix} 1 \\ -1 \end{bmatrix} \tag{1.20}$$

The final two polarizations are in the circular basis, meaning instead of the electric field oscillating in a line, they oscillate in a circle. When the electric field is rotating counter-clockwise (CCW), the photon is right circularly polarized (RCP), $|R\rangle$, and the clockwise (CW) rotation is left circularly polarized (LCP), $|L\rangle$. These states represent equal and opposite α and β with a 90° phase difference.

$$|R\rangle = \frac{1}{\sqrt{2}}\left(|0\rangle - i\,|1\rangle\right) = \frac{1}{\sqrt{2}}\begin{bmatrix} 1 \\ -i \end{bmatrix} \qquad |L\rangle = \frac{1}{\sqrt{2}}\left(|0\rangle + i\,|1\rangle\right) = \frac{1}{\sqrt{2}}\begin{bmatrix} 1 \\ i \end{bmatrix} \tag{1.21}$$

Together, these three sets of orthogonal bases: $|H\rangle\,/\,|V\rangle$, $|D\rangle\,/\,|A\rangle$, and $|R\rangle\,/\,|L\rangle$ span the polarization space and can be used to describe a photon in any polarization. We can also observe that the polarization of any photon can be visualized using a polarization ellipse which can be described by two parameters (Figure 1.1): the orientation angle, ψ, which indicates the angle the major axis of the ellipse is from the x-axis, and the ellipticity angle, χ, which is the angle between the major and minor axis of the ellipse. These parameters

are defined in Equation 1.22, using the probability amplitudes of a state $\alpha |H\rangle + \beta |V\rangle$ and the phase difference between them, $\delta = \theta_\alpha - \theta_\beta$

$$\tan(2\psi) = \frac{2|\alpha||\beta|}{\alpha^2 - \beta^2}\cos(\delta) \qquad \tan(2\chi) = \frac{2|\alpha||\beta|}{\alpha^2 + \beta^2}\sin(\delta) \tag{1.22}$$

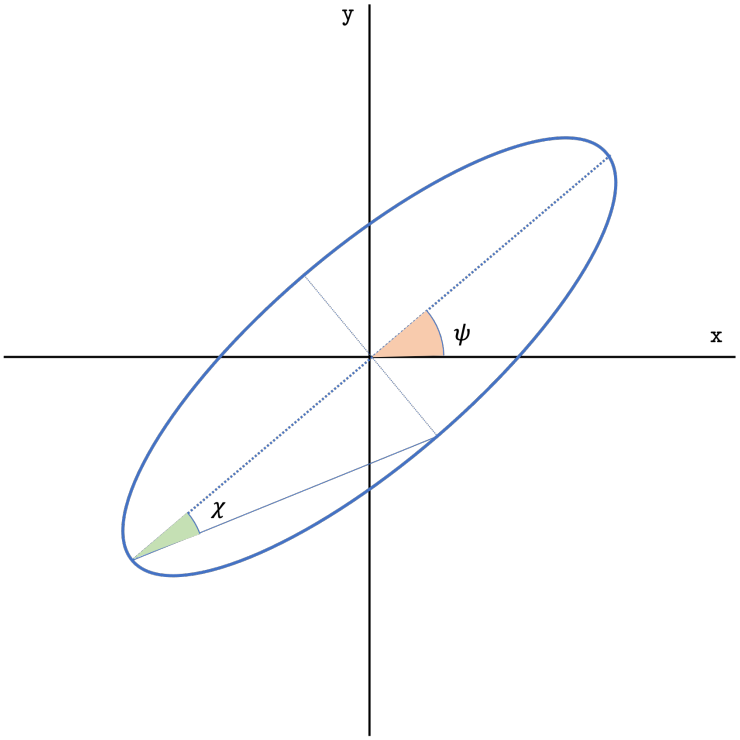

Figure 1.1: Polarization ellipse of a photon with the ellipticity (χ) and orientation (ψ) angle labelled.

Having established how we define the states of the photons, we must also examine how to measure them to determine their state.

1.2.2 Measurements

We have previously discussed how a single measurement of a single qubit gives us limited information, and we need repeated measurements to reconstruct the state of the qubit. Since we are working with photons where the polarization defines the state, we require

a method for reliably measuring the photon's polarization. There are two primary kinds of single-photon detectors, single-photon avalanche diodes and superconducting nanowire single-photon detectors, both of which are only capable of telling us that a photon was detected but not what polarization it had. To overcome this, we can use a polarization filter before the detector, which will only allow photons of a particular polarization, say $|H\rangle$, to travel to the detector and photons in the orthogonal polarization, $|V\rangle$, will be either absorbed or sent down a different optical path. This process gives us a projective measurement in $|H\rangle$.

A projective measurement occurs when the original qubit is projected onto the measured state. The observables of every qubit can be described by a set of eigenvectors and their corresponding eigenvalues, which are the measurement outcomes and must be real numbers. Once a specific eigenvalue has been measured, the state collapses into the corresponding eigenvector, hence the term projective.

$$|\Psi_1\rangle = 0.8\,|H\rangle + 0.6\,|V\rangle \tag{1.23}$$

A projective measurement is mathematically represented by the projection operator $P(\Psi) = |\Psi\rangle\langle\Psi|$. For example, if we take Equation 1.2, which has been converted to terms of polarization in Equation 1.23 and take the projective measurement in state $|H\rangle$, we get:

$$\begin{aligned} P(H) &= \langle\Psi|\,|H\rangle\langle H|\,|\Psi\rangle = (0.8\,\langle H| + 0.6\,\langle V|)\,|H\rangle\langle H|\,(0.8\,|H\rangle + 0.6\,|V\rangle) = 0.8^2 \\ &= 0.64. \end{aligned} \tag{1.24}$$

This measurement tells us that, as expected, 64% of the photons will be detected, and 36% of the photons will be discarded. We are not limited to only measuring $|H\rangle$ and $|V\rangle$. Instead we can perform measurements in any of the six bases, which gives us more information on the states. For example measuring Equation 1.23 in $|D\rangle$ we get $P(D) = 0.98$ and in $|R\rangle$ we get $P(R) = 0.5$. This ability to measure in other states allows us to determine the phase difference in state that would be invisible only using the $|H\rangle$ / $|V\rangle$ eigenstates. For example, by only measuring the linear states we would not be able to tell the difference between Equation 1.23 and the state $0.8\,|H\rangle + i0.6\,|V\rangle$ however using the $|R\rangle$ basis the projective measurements are $P(R) = 0.5$ and $P(R) = 0.02$ respectively. This measurement process allows us to reconstruct fully the state of a photon, which will be used in Section 4.1 of this thesis.

Examining the polarization bases shows us how photons can be in a state of superposition and other single-qubit states, but it does not examine entanglement or multi-qubit

states. Entanglement can be created using multiple methods, the easiest of which is an entangled photon source. We will examine the specifics of entangled photon sources in Chapter 2.

Chapter 2

Photon Sources

Photonics are a promising platform for quantum computing but to make the platform functional and scalable we need a source of entangled photons. The ideal photon source must address a list of qualities that would make it usable for quantum algorithms.

2.1 Ideal Photon Source

There are five primary qualities that a photon source must display to be considered ideal for quantum computing: bright, on-demand, high photon pair purity, highly entangled, and indistinguishable.

Bright

The brightness of a photon source is defined as the number of photon pairs released per second. There is no exact amount of photons per second defined to be ideal, but generally, the higher, the better. We will consider a lower limit of 10^7 photons per second as acceptable. We can see why brightness is considered so crucial by comparing it to the classical computing analogues of bits. The bitrate of a computer determines how much information or how many bits can be transferred in a given period. The more bits available, the more information can be transferred and the faster our computers can function. The same goes for qubits and quantum information.

Brightness is also crucial for combating loss within a system. Photons can be transferred through a system using various methods; fibre optic, free space, and crystal waveguides

are the most common. All of these methods have a specific loss per length or attenuation. Multi-mode fibre usually has 1.5 dB/km loss at 1300 nm [22], a silison nitride (SiN) crystal waveguide has around 0.8 dB/cm loss at a similar wavelength [23], and free space optics range widely depending on the conditions. Classical computers overcome loss by sending multiple copies of the information, so the information can be easily recovered if some gets lost. This method cannot be used with quantum qubits, as they are limited by the no-cloning theorem, meaning we cannot send multiple copies of the same qubit [24]. Quantum repeaters have been designed and developed [25], which, in theory, would allow information to travel over longer distances without being overcome by loss, but in all cases, the more photons that are initially available, the more information that can be transmitted.

It is important to note that brightness is affected by the amount of light output by the source and the amount that reaches the first collection lens after the source. If a source emits light at a wide range of angles, we can only use a portion of those photons, which reduces the brightness of the source. In the case of entangled photons, we also have to consider if the collection lens will always capture both photons.

On-Demand

An on-demand source is one where every trigger creates an event releasing a photon pair. On-demand photons are essential when we require two photons to interfere with each other, such as with entanglement swapping and when measuring the Hong-Ou-Mandel effect. For two photons to interfere with each other, they must be incident upon a beam-splitter simultaneously, meaning we have to be able to reliably predict when photons are released.

An ideal source will receive a triggering event, most commonly electrical signals or laser pulses, and will release the photon pair within a set period. Some sources are probabilistic, meaning only a certain percentage of trigger pulses release photons, which are released randomly. There are ways to overcome this randomness for single photons outlined in Section 2.2 but none for entangled pairs.

Photon-Pair Purity

For an ideal source, only one pair of photons is released when a triggering event occurs. This is known as photon-pair purity. If only one trigger is applied, only one photon pair will be emitted; however, spontaneous sources emit photons based on a Poissonian distribution, and sources based on electron recombination can be re-excited, emitting multiple pairs. This poses a problem when working with entangled pairs as one detector might measure

a photon from one pair, and the other measures a photon from the other pair, leading to decreased measured entanglement.

Photon purity is measured using the Hanbury-Brown-Twiss effect to find the second-order auto-correlation, or $g^{(2)}(\tau)$. This measures the probability of detecting a photon at time τ after detecting the first photon at time t and is described by Equation 2.1.

$$g^{(2)}(\tau) = \frac{\langle n(t)n(t+\tau)\rangle}{\langle n(t)\rangle^2} \tag{2.1}$$

Single-photon purity is measured when $\tau = 0$, which is the probability of two photons being detected simultaneously. An ideal single-photon source will have a $g^{(2)}(0) = 0$. For an entangled photon source, we can measure the pair purity by spatially separating the halves of the pairs and measuring the $g^{(2)}$ of each half. A low $g^{(2)}$ indicates a high photon pair purity.

$$g^{(2)}(0) = \frac{\langle n^2\rangle - \langle n\rangle}{\langle n\rangle^2} \tag{2.2}$$

Entangled

The photon pairs released by an ideal entangled photon source should be, to nobody's surprise, perfectly entangled. As mentioned in Section 1.1.2, entanglement is measured using concurrence, with maximum entanglement giving a concurrence of 1. Many factors affect the concurrence of the source. As stated previously, low photon-pair purity decreases measured entanglement. Background light and detector dark counts can also affect the concurrence by preventing the measurement of both halves of an entangled pair. A source's fidelity to one of the Bell states is also sometimes considered to be a factor in entanglement. As discussed previously, a Bell state is considered the ideal entangled state and therefore is frequently a requirement for many quantum algorithms [17, 18].

Indistinguishable

Finally, a source should produce indistinguishable photons, meaning each photon pair released should be identical in all meaningful characteristics (for example, frequency or polarization). Indistinguishability can be measured using the Hong-Ou-Mandel effect and two-photon interference, which relies on the principle that two identical photons incident on

a beam splitter will interfere and always exit out of the same port of the beam splitter. In contrast, distinguishable photons have a 50% chance of exiting the same port. Two-photon interference is required to implement quantum repeaters and other quantum systems.

2.2 State of the Art Sources

The most widely used and commercially developed photon sources are spontaneous parametric down conversion (SPDC) sources. These sources use a non-linear crystal and a pump laser to produce entangled photon pairs. The pump laser emits high-energy photons, which have the possibility of splitting into two lower-energy photons. The theory behind SPDC sources is outside the scope of this thesis, but we can examine how they do or do not fulfill the requirements outlined in the previous section.

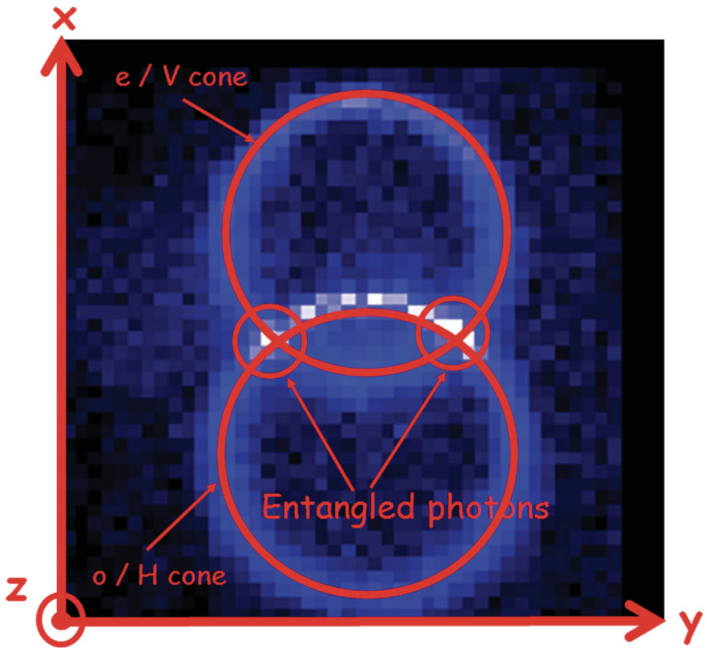

Figure 2.1: Graph representing two emission cones of a SPDC source [1]. The intersection between these two cones represent areas where photons are polarization entangled.

SPDC sources excel in two of the five requirements: indistinguishablity and entanglement. Due to the conservation of momentum, the photons are emitted at an angle, creating

two emission cones, each with a known energy and each cone having an opposite polarization. All the photons emitted within a cone will be indistinguishable from each other [1]. Areas where cones intersect produce highly entangled photons with unity concurrence as shown in Figure 2.1.

SPDC sources do have their downsides, namely being a spontaneous source. This means they do not fulfill the requirement of being on-demand. We can combat this when we only want to use single photons, as we can use one of the photon pairs as a heralding event to alert us to the presence of a single photon. However, this solution does not address the problem when using entangled photon pairs. SPDC sources also tend to have low brightness. For example, a commercial SPDC source (SPDC810) from Thorlabs has a pair emission rate of >450 kHz [26], which is functional but lower than what we consider ideal. Attempting to improve the brightness by increasing the power of the pump laser leads to a reduction in the photon-pair purity as SPDC sources emit pairs according to a Poissonian distribution [1].

While SPDC sources are the current state-of-the-art source for single and entangled photons, we can see that there is still significant room for improvement within the field.

2.3 Quantum Dots

A potential contender for the ideal source of single and entangled photons is the quantum dot (QD). Also known as artificial atoms, QDs are an area of three-dimensional confinement with discrete energy levels. They are created from regions of material with a lower bandgap than the surrounding material. Most commonly, QDs are made of either indium arsnide phosphide surrounded by indium phosphide or indium gallium arsnide surrounded by gallium arsnide. Research into QDs began in the early 1980s and has seen many improvements since then, including control of the dots' position, size, and shape [27, 28]. Before discussing how QDs fulfill the requirements of being an ideal photon source, we must understand how they produce photons.

2.3.1 Confinement

As mentioned, QDs are a region of three-dimensional energy confinement. This means the region can carry electrons in the conduction band and electron holes in the valance band at distinct energy levels. This band structure is where the analogy to atoms comes from, as these discrete bands can be considered similar to the electron orbitals around

an atom. Given enough energy, electrons can be excited out of the ground state, where electrons and electron holes are combined, to an excited state where the electron resides in the conduction band, and an electron hole is in the valance band. At some point, the electron-hole pair will recombine radiatively, releasing a photon at a known. We are only interested in using the lowest energy transition, analogous to the s-shell of an atom. This level is non-degenerate except for spin degeneracy, so it can only contain two electrons and two holes. This is beneficial as the only decay available will be radiative recombination instead of relaxing to a lower energy level. The shape of the dot controls the energy levels of a QD, so we need to choose one where only one energy level is available.

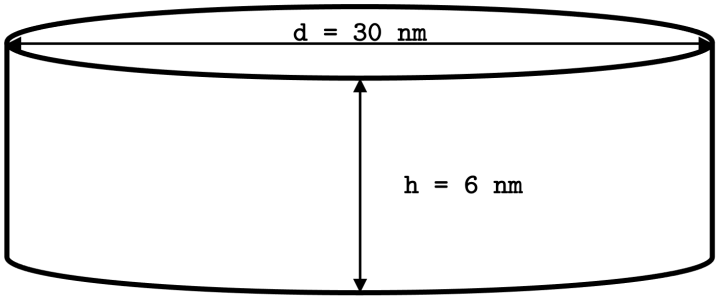

Figure 2.2: Simple representation of a puck-shaped QD. The dots we use are approximately 6 nm in height and 30 nm in diameter.

The confining potential for this shape is primarily along the z direction, which forms a one-dimensional square well with the degree of confinement controlled by the height. The QDs discussed in this thesis are 6 nm in height, ensuring that only one excited state is in the z-direction. There is also weaker confinement in the radial direction, which allows for the presence of sublevels. The potential energy in this direction is modelled by a simple two-dimensional harmonic oscillator, $V(r) = \frac{1}{2}m^*\omega^2 r^2$, where m^* is the effective mass of the electron or electron-hole. These combine to form allowable energy states described by Equation 2.3, where $n = 0, 1, 2, ...$ is the radial quantum number, $l = 0, \pm 1, \pm 2$ is the orbital quantum number, and $\hbar\omega$ is the quantized energy of the electron or hole.

$$E_{n,l} = (2n + |l| + 1)\hbar\omega \tag{2.3}$$

For this thesis, we are only concerned with the lowest energy level, which can be marked as $E_{0,0}$, but it is important to know that sub-levels are present within QDs and must be accounted for when exciting the dot.

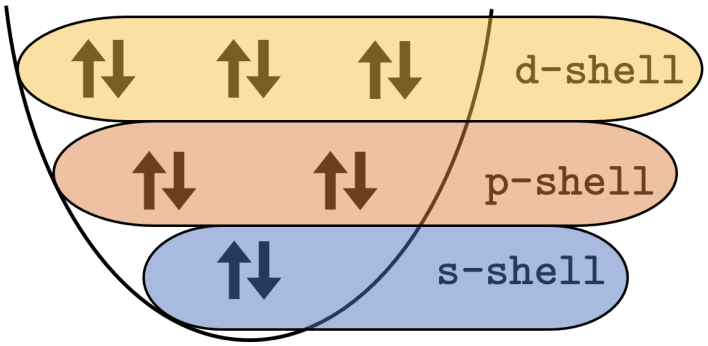

Figure 2.3: Simple energy level structure of the conduction band of a QD. The QDs we use are height-limited, so only the s-shell is available. The valance band would be an inverted version of this structure.

2.3.2 Photon Generation

As alluded to in the previous section, electrons in the quantum dot can be excited to the lowest excited state. Then, they will radiatively recombine with the hole in the valance band and release a photon of a distinct energy. This recombination is the process through which QDs are a source of on-demand photons. Most commonly, electrons are excited using a laser pulse, but work is being done to investigate electronically driving electron excitation [29].

During radiative recombination, angular momentum must be conserved. Photons have two possible spin-angular momentum (SAM) values, +1 and -1 in units of $\hbar$; these correspond to LCP and RCP photons, respectively. Only recombinations where the total angular moment is equivalent to $\pm$ 1 are allowed. The total angular moment of a charge carrier (electron or an electron-hole) is found in Equation 2.4 where L_s is the operator for orbital angular momentum of the shell, L_b is the operator for the intrinsic angular moment of the band, and S is the operator for the SAM of the charge carrier.

$$\boldsymbol{J = L_s + L_b + S} \tag{2.4}$$

These operators have eigenvalues j, l_b, l_s, and s. At the lowest excited state, $l_s = 0$ for both electrons and holes. However, l_b is 0 for electrons as they occupy the bottom of the conduction band, which is s-like, whereas holes occupy the top of the valence band, which is p-like with an angular momentum of 1. Both electrons and holes have a SAM of $\frac{1}{2}$. This means that electrons have $j = \{\frac{1}{2}\}$ and holes $j = \{\frac{1}{2}, \frac{3}{2}\}$. We also must consider

the angular momentum on the z-axis, which will fall between $-j$ and j inclusive. This means electrons can have a $j_z = \{-\frac{1}{2}, \frac{1}{2}\}$ and holes a $\{-\frac{3}{2}, -\frac{1}{2}, \frac{1}{2}, \frac{3}{2}\}$. Figure 2.4 displays the energy band structure.

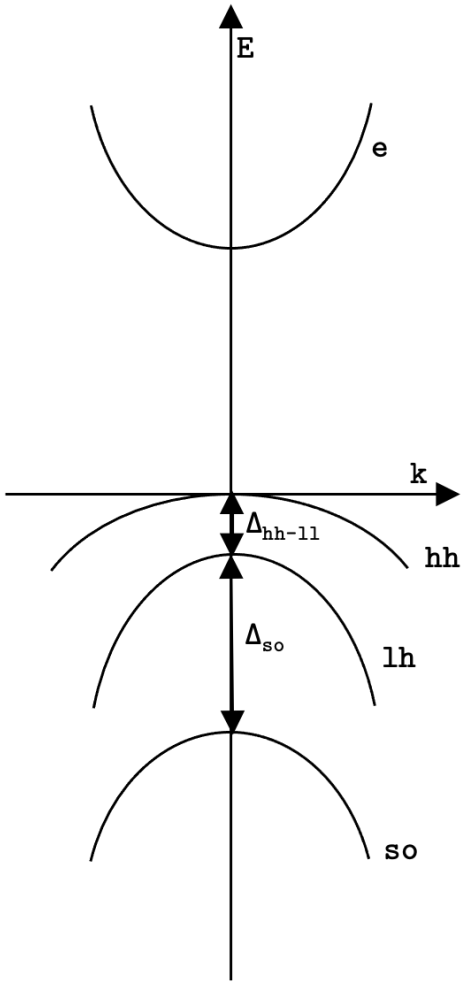

Figure 2.4: Band structure of a QD conduction and valance bands. The curve labelled e represents the electrons with $j = \frac{1}{2}$. There are three curves in the valance band; the lowest, labelled *so*, is the spin-orbit split-off with $j = \frac{1}{2}$. The light hole curve with $j = \frac{3}{2}$ and $j_z = \pm\frac{1}{2}$ is labelled lh and the heavy hole curve with $j = \frac{3}{2}$ and $j_z = \pm\frac{3}{2}$ is labelled hh. There is a difference in energy between these two layers labelled Δ_{hh-ll} the curves also "bend" at different rates due to the spin-orbit coupling, Δ_{so}.

The holes exist in three distinct energy states, the first being those with $j = \frac{1}{2}$ which is a spin-orbit split-off band, the middle layer with $j = \frac{3}{2}$ and $j_z = \pm\frac{1}{2}$ which is the light hole layer, finally the layer with the lowest energy excited state is the heavy hole layer with $j = \frac{3}{2}$ and $j_z = \pm\frac{3}{2}$. Optical transitions for the lowest energy level only occur between electrons and heavy holes so that we can disregard the other hole layers, and moving forward, heavy holes will be referred to as holes.

Remembering that recombination preserves angular momentum and the SAM of photons is either -1 or 1, we can see that a recombination event emitting a photon must have a $\Delta j_z = \pm 1$. This occurs when either $j_{z,e} = \frac{1}{2}$ and $j_{z,h} = -\frac{3}{2}$ or $j_{z,e} = -\frac{1}{2}$ and $j_{z,h} = \frac{3}{2}$.

An excited QD features two electrons in the conduction band and two holes in the valance band. Both of these will recombine but not at the same time. The first will recombine into either a photon with a SAM of either -1 or 1 and is labelled the biexciton (XX); the second has to emit a photon with an opposite SAM as the first and is known as the exciton (X). Remembering that a SAM of 1 corresponds to a LCP photon and -1 is a RCP photon, the exciton and biexciton will always have opposite polarizations.

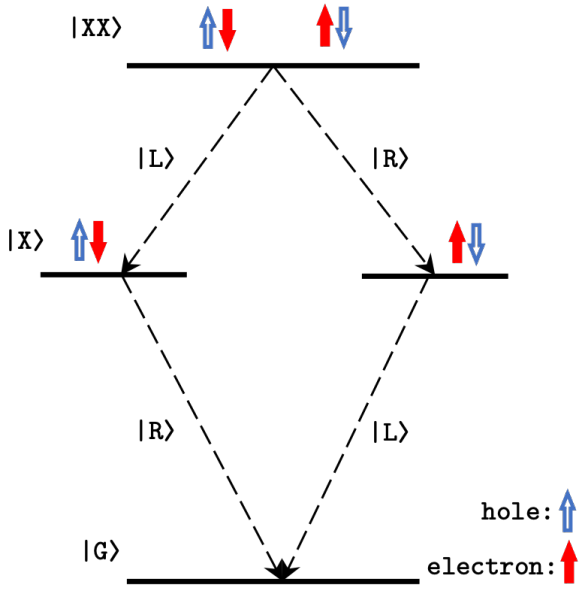

Figure 2.5: The XX-X cascade, Electron-hole pairs recombine to produce either an LCP or RCP biexciton, then an exciton is released in the opposite polarization as the biexciton when the remaining pair recombines.

There are two possible recombination pathways, also known as the biexciton-exciton

cascade (XX-X cascade): either the biexciton is LCP, and the exciton is RCP, or the biexciton is RCP, and the exciton is LCP. Since we cannot know which pathway took place until measuring the polarization of the photons, there is a superposition created upon recombination. This leads to a polarization-entangled state expressed as the maximally entangled state Equation 2.5.

$$|\Psi\rangle = \frac{1}{\sqrt{2}}[|RL\rangle + |LR\rangle] \tag{2.5}$$

2.3.3 Fine-Structure Splitting

Equation 2.5 represents the entangled state emitted from an ideal quantum dot. In reality, asymmetries in the shape, strain, and crystal makeup of the dot can affect the confining potential of the dot. This asymmetry shifts the energy of each photon by an amount $\pm\delta$. This difference is known as fine-structure splitting (FSS) and affects the emitted entangled state of the dot. Due to phase accumulation between the two pathways, the emitted state depends on the time (τ) between the recombination of the biexciton and the exciton.

$$|\Psi(\tau)\rangle = \frac{1}{\sqrt{2}}\left[|HH\rangle + e^{-i\frac{\delta\tau}{\hbar}c}\,|VV\rangle\right] \tag{2.6}$$

With symmetry broken, the eigenstates of the dot switch from the circular to the linear basis, but expanding the state according to the circular basis, we get Equation 2.7.

$$|\Psi(\tau)\rangle = \frac{1}{\sqrt{2}}\left[(|RL\rangle + |LR\rangle)\cos\left(\frac{\delta\tau}{2\hbar}\right) - i\,(|RR\rangle + |LL\rangle)\sin\left(\frac{\delta\tau}{2\hbar}\right)\right] \tag{2.7}$$

We can see from this expression that after the biexciton is emitted, the remaining electron precesses as though it was in a magnetic field, sometimes emitting the exciton in the same circular basis as the biexciton.

In the case of a QD with an FSS larger than the linewidth of a photon, ≈ 1 μeV, a detector with high energy resolution can resolve the difference between the two pathways, removing the superposition entirely. The state emitted by a QD with an FSS < 1 μeV is still an entangled state as detectors cannot resolve the difference between the pathways and the state will theoretically measure a concurrence of 1. However, the time dependence of the state makes using the entangled photons challenging. If we require photons in a specific entangled state, as quantum repeaters do, we would need to time gate the emitted

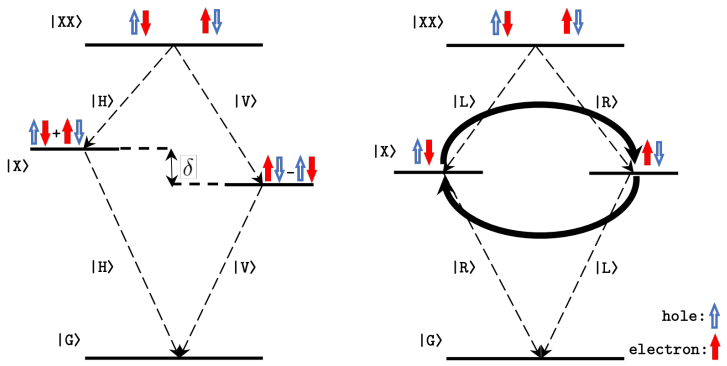

Figure 2.6: XX-X cascade in the presence of a FSS, δ. With the system's symmetry broken, the eigenstates switch to the linear basis with an energy difference between the intermediate states. When the state is examined in a circular basis, the electron remaining after the biexciton is released precesses as though in a magnetic field.

photons to select for ones with a desirable state. This would significantly reduce counts and the on-demand nature of QDs.

2.3.4 Quantum Dots as Ideal Photon Sources

Now that we understand what quantum dots are and how they work, we can look at how they fulfill our requirements for an ideal photon source. We have already gone through how QDs are on-demand as a single laser pulse will excite the electrons, and shortly after, the biexciton and exciton will be released. We also know that because we can select QDs that only allow for one energy level, meaning only one pair of electrons can be excited at a time, and only one pair of photons will be released. This leads to high photon-pair purity, and the separation in wavelength between the biexciton and exciton allows QDs also to have high single-photon purity [2, 30]. Subsequent emitted photons have a high degree of indistinguishability [31]. However, the QD's sensitivity to minute changes in shape and size leads to poor indistinguishability between dots. This has been addressed mainly through improvements in manufacturing at developments that allow the QD's energy levels to be tuned [32, 33].

One of the most significant improvements that QDs have over SPDC sources is the source's brightness. While SPDC sources always have to compromise brightness for photon purity, QDs are only limited by the recombination rate of the electrons and the collection efficiency of the first objective lens. The former is not a significant limitation, but the

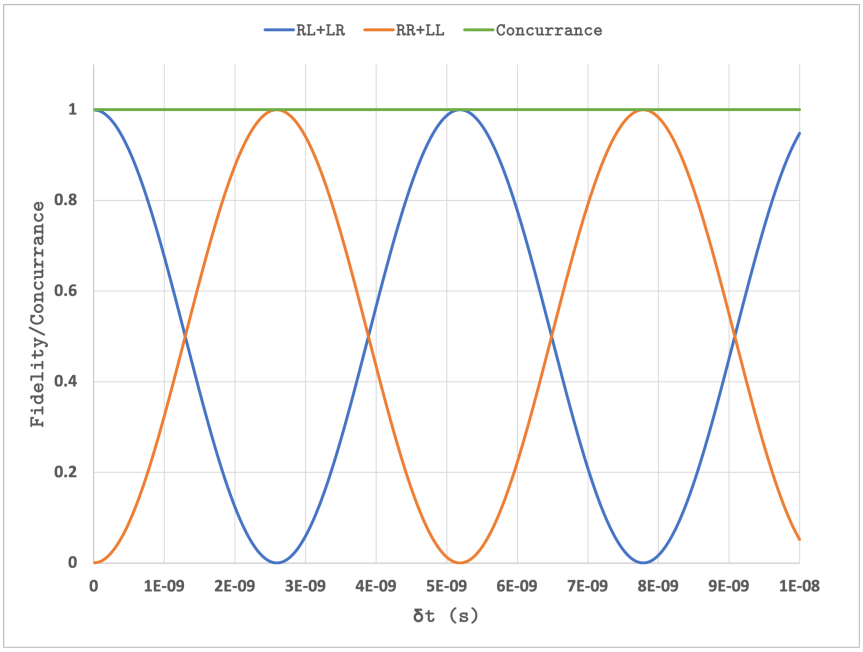

Figure 2.7: Simulation of the concurrence of the entangled state and the fidelity to the two Bell states oscillating as a function of δt assuming a 5 μeV FSS.

latter poses a problem. QDs do not emit photons in a single direction, which prevents even the largest of objective lenses from having a high collection efficiency. To combat this, various nanostructures have been developed to direct the emission of a QD in predictable directions. Structures such as bulls-eye cavities and nanopillars use a cavity, which uses a Purcell enhancement to increase spontaneous emission into the cavity mode [34, 35]. Other groups, including our lab, use nanowires made of high-refractive index materials, leading to strong confinement to a fundamental guided mode [2, 36]. A typical nanowire is shown in Figure 2.8. There are unique benefits to each type of nanostructure, but other than their effectiveness in improving the brightness of dots, the specifics are out of the scope of this work.

The high degree of entanglement of the source is also a benefit of QDs, but as discussed, FSS affects the fidelity to an ideal Bell state and makes QDs less suitable for many procedures such as quantum teleportation or quantum key distribution [17, 18]. Several methods have been developed to address the FSS, including using thermal annealing [37], magnetic fields [38], electric fields [33, 39], or strain tuning [32, 40]. These methods all

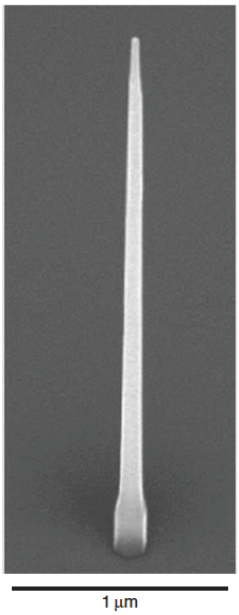

Figure 2.8: Scanning electron microscope of a tapered nanowire waveguide with a QD embedded 200 nm from the base of the wire [2].

require processing each and every dot used in a project directly either by fabricating gates close to the dot, applying stress to the material the dot is contained in, or applying heat to the dot. Due to this requirement, implementing these methods on a QD in a nanostructure is a challenge due to strain relaxation across the nanostructure. Some have proposed using electric fields around a nanowire [41], and another group used strain across the base of a nanowire [42]. Due to the importance of nanostructures in improving the brightness of QDs, a method of removing fine-structure splitting that can be used in conjunction with every type of nanostructure is vital. One such method is described in Chapters 3 and 4.

Chapter 3

Fine-Structure Splitting Eraser

There have been many methods developed to remove the FSS of quantum dots. These include using electric [33], magnetic [32], and strain fields [38] and thermal annealing [37]. These methods have managed to effectively remove the FSS of QDs greater than 20 μeV [32]. However, these methods all involve complicated fabrication techniques that must be performed on each quantum dot that will be used in an experiment, making scaling complicated. They also cannot easily be used with nanostructures, which, as discussed in Section 2.3.4, are important for increasing the collection efficiency of quantum dots because of strain relaxation [42]. Our project addresses these concerns using a novel all-optical method of removing fine-structure splitting.

3.1 All-Optical Approach

The all-optical method developed by Fognini et al. uses unitary optical components to remove the FSS without photon loss or filtering required by other schemes [3]. This approach relies on the use of quarter wave plates (QWPs) and fast-rotating half-wave plates (HWPs) to convert the state first to the circular basis as described by Equation 3.1 and finally to a time-independent Bell state (Equation 3.2).

$$|\Phi(t)\rangle = \frac{1}{\sqrt{2}}\left[|LR\rangle + e^{-i\frac{\delta}{\hbar}c}\,|RL\rangle\right] \tag{3.1}$$

$$|\chi\rangle = \frac{1}{\sqrt{2}}\left[|RL\rangle + |LR\rangle\right] \tag{3.2}$$

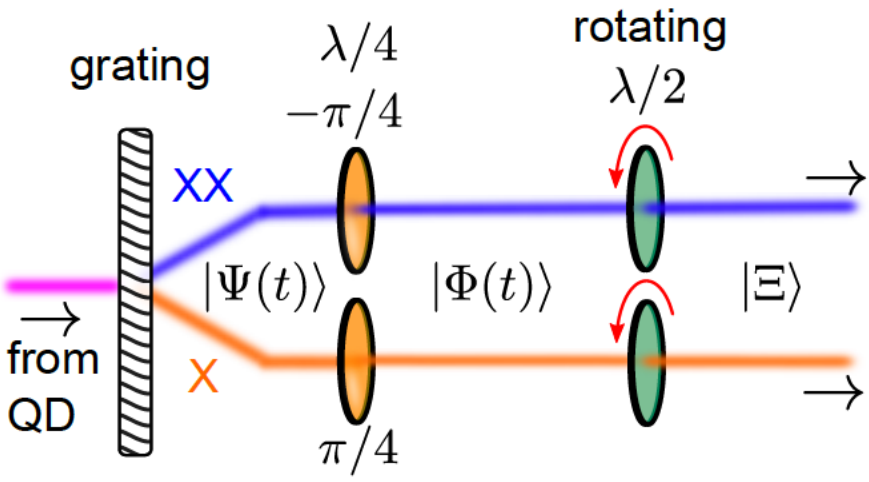

Figure 3.1: Diagram of proposed optical set-up for FSS eraser. First, the biexciton and exciton are split into two pathways using a transmission grating. The biexcitons are sent through a QWP set at a $-45°$ angle while the excitons travel through a QWP set at a $45°$ angle. Both beams then travel through HWPs rotating CW. [3]

3.1.1 Fast-Rotating Half Wave Plate

Rotating half-wave plates spinning with an angular frequency ω can be described by the Operator 3.3. This equation and the following process for defining the CW rotating HWP come from the textbook by Chuang [43].

$$\Lambda_{1/2}(\omega) = \sum_k a^\dagger_{k+\frac{2\omega}{c},L} a_{k,R} + a^\dagger_{k-\frac{2\omega}{c},R} a_{k,L} \tag{3.3}$$

Here c is the speed of light, and $a_{k,\lambda}$, $a^\dagger_{k,\lambda}$ are the annihilation and creation operators of photons with wavevector length k and polarization $\lambda \in \{R, L\}$ To see how this removes the FSS, I expressed the state Equation 2.6 using creation and annihilation operators.

$$\Psi = \frac{1}{\sqrt{2}} \left[a^\dagger_{z,k_{XX}+\frac{\delta}{2\hbar c},H} a^\dagger_{z-\tau c,k_X-\frac{\delta}{2\hbar c},H} + a^\dagger_{z,k_{XX}-\frac{\delta}{2\hbar c},V} a^\dagger_{z-\tau c,k_X+\frac{\delta}{2\hbar c},V} \right] \tag{3.4}$$

In Equation 2.6, z refers to the spatial position of the photon, and we can observe that the exciton is delayed by a factor τc. We also observe that the wavevector is affected by a

FSS equal to $\frac{\delta}{2\hbar c}$. To apply the scheme described by Fognini et al., we also need the effect of the QWP on linearly polarized light described by creation and annihilation operators:

$$\Lambda_{1/4}\left(-\frac{\pi}{4}\right) = a^\dagger_{k_i,R}a_{k_i,V} + a^\dagger_{k_i,L}a_{k_i,H} \tag{3.5}$$

$$\Lambda_{1/4}\left(\frac{\pi}{4}\right) = a^\dagger_{k_i,L}a_{k_i,V} + a^\dagger_{k_i,R}a_{k_i,H} \tag{3.6}$$

By spatially separating the exciton and biexciton using a transmission grating, We can use these two QWP to convert Equation 2.6 to the RCP/LCP basis:

$$\begin{aligned}\Phi &= \left(\Lambda_{1/4}\left(-\frac{\pi}{4}\right)\otimes\Lambda_{1/4}\left(\frac{\pi}{4}\right)\right)\Psi \\ &= \frac{1}{\sqrt{2}}\left[a^\dagger_{z,k_{XX}+\frac{\delta}{2\hbar c},L}a^\dagger_{z-\tau c,k_X-\frac{\delta}{2\hbar c},R} + a^\dagger_{z,k_{XX}-\frac{\delta}{2\hbar c},R}a^\dagger_{z-\tau c,k_X+\frac{\delta}{2\hbar c},L}\right]\end{aligned} \tag{3.7}$$

The light is required to be in the circular polarization basis for the interaction with the HWP to produce the desired results. The reason for this will be discussed further in Section 3.2.

$$\begin{aligned}\Xi(\omega) &= \left(\Lambda_{1/2,XX}(\omega)\otimes\Lambda_{1/2,X}(\omega)\right)\Phi \\ &= \frac{1}{\sqrt{2}}\left[a^\dagger_{z,k_{XX}+\frac{\delta}{2\hbar c}-\frac{2\omega}{c},R}a^\dagger_{z-\tau c,k_X-\frac{\delta}{2\hbar c}+\frac{2\omega}{c},L} + a^\dagger_{z,k_{XX}-\frac{\delta}{2\hbar c}+\frac{2\omega}{c},L}a^\dagger_{z-\tau c,k_X+\frac{\delta}{2\hbar c}-\frac{2\omega}{c},R}\right] \\ &= \frac{1}{\sqrt{2}}\Big[a^\dagger_{z,k_{XX},R}e^{i\left(z\left(\frac{\delta}{2\hbar c}-\frac{2\omega}{c}\right)\right)}a^\dagger_{z,k_X,L}e^{i\left(-z\left(\frac{\delta}{2\hbar c}-\frac{2\omega}{c}\right)-\tau ck_X+\tau c\left(\frac{\delta}{2\hbar c}-\frac{2\omega}{c}\right)\right)} \\ &+ a^\dagger_{z,k_{XX},L}e^{i\left(-z\left(\frac{\delta}{2\hbar c}-\frac{2\omega}{c}\right)\right)}a^\dagger_{z,k_X,R}e^{i\left(z\left(\frac{\delta}{2\hbar c}-\frac{2\omega}{c}\right)+\tau ck_X-\tau c\left(\frac{\delta}{2\hbar c}-\frac{2\omega}{c}\right)\right)}\Big] \\ &= \frac{1}{\sqrt{2}}\left[a^\dagger_{z,k_{XX},R}a^\dagger_{z,k_X,L}e^{i\tau c\left(\frac{\delta}{2\hbar c}-\frac{2\omega}{c}\right)} + a^\dagger_{z,k_{XX},L}a^\dagger_{z,k_X,R}e^{-i\tau c\left(\frac{\delta}{2\hbar c}-\frac{2\omega}{c}\right)}\right]\end{aligned} \tag{3.8}$$

From Equation 3.8, we can see that the FSS can be removed by using a $\omega = \frac{\delta}{4\hbar}$.

$$\begin{aligned}\Xi\left(\frac{\delta}{4\hbar}\right) &= \frac{1}{\sqrt{2}}\left[a^\dagger_{z,k_{XX},R}a^\dagger_{z,k_X,L}e^{i\tau c\left(\frac{\delta}{2\hbar c}-\frac{2\delta}{4\hbar c}\right)} + a^\dagger_{z,k_{XX},L}a^\dagger_{z,k_X,R}e^{-i\tau c\left(\frac{\delta}{2\hbar c}-\frac{2\delta}{4\hbar c}\right)}\right] \\ \chi &= \frac{1}{\sqrt{2}}\left[a^\dagger_{z,k_{XX},R}a^\dagger_{z,k_X,L} + a^\dagger_{z,k_{XX},L}a^\dagger_{z,k_X,R}\right]\end{aligned} \tag{3.9}$$

Reverting to ket notation, the state becomes the time-independent Bell state $|\Xi\rangle = \frac{1}{\sqrt{2}}[|RL\rangle + |LR\rangle]$. This state can be measured accurately even using detectors with a large timing jitter.

Most QDs can be fabricated with FSS < 10 μeV [2], which translates to an $\omega > 600$ MHz, which is a significantly higher frequency than can be achieved using a physical HWP. An electro-optic modulators can be used to emulate a fast rotating HWP to overcome this obstacle.

3.2 Electro-Optic Modulation

The optical properties of a material can be controlled using an electric field of a lower frequency than the frequency of light travelling through the material. This is known as the electro-optic effect. This effect is utilized in electro-optic modulators (EOMs) to change properties such as the phase, frequency, amplitude or polarization of a beam of light. We will examine how EOMs affect the frequency of single photons by controlling the material's index of refraction.

3.2.1 Birefringence

Certain materials have an optical property known as birefringence. Birefringence is when a material's index of refraction is dependent on the polarization and propagation direction of the incident light. This property is used to create both HWPs and QWPs. The effects of a birefringent material are typically described by an index ellipsoid, which is derived from the permittivity (Equation 3.10) matrix where the coordinate system has been chosen such that the matrix is diagonalized.

$$\overline{\overline{\varepsilon}} = \begin{bmatrix} \varepsilon_x & 0 & 0 \\ 0 & \varepsilon_y & 0 \\ 0 & 0 & \varepsilon_z \end{bmatrix} = \varepsilon_0 \begin{bmatrix} n_x^2 & 0 & 0 \\ 0 & n_y^2 & 0 \\ 0 & 0 & n_z^2 \end{bmatrix} \tag{3.10}$$

The permittivity of a material (relative permittivity) describes the degree to which a material polarizes when subjected to an electric field compared to the effect the same electric field would have on a vacuum (ε_0). Permittivity is related to the index of refraction of a material according to $n_i = \sqrt{\frac{\epsilon_i \mu_i}{\epsilon_0 \mu_0}} = \sqrt{\frac{\epsilon_i}{\epsilon_0}}$ when the permeability of the material is

equivalent to that of a vacuum ($\mu_i = \mu_0$). However, to describe the index ellipse, we need the inverse of the permittivity matrix, the impermeability matrix (Equation 3.11).

$$\overline{\overline{K}} = \varepsilon^{-1} = \frac{1}{\varepsilon_0} \begin{bmatrix} \frac{1}{n_x^2} & 0 & 0 \\ 0 & \frac{1}{n_y^2} & 0 \\ 0 & 0 & \frac{1}{n_z^2} \end{bmatrix} \tag{3.11}$$

The index ellipse is described by Equation 3.12, where K_{ij} are elements of $\overline{\overline{K}}$ and c_i is the ith element of the tuple (x, y, z).

$$\varepsilon_0 \sum_{i,j=1}^{3} K_{ij} c_i c_j = \frac{x^2}{n_x^2} + \frac{y^2}{n_y^2} + \frac{z^2}{n_z^2} = 1 \tag{3.12}$$

In a uniaxial medium, where two of the axes have equivalent permittivity values and the third, the optical axis, has a different permittivity, Equation 3.12 becomes Equation 3.13

$$\frac{x^2}{n_o^2} + \frac{y^2}{n_o^2} + \frac{z^2}{n_e^2} = 1 \tag{3.13}$$

Here, the subscript o refers to the ordinary wave solution, and e is the extraordinary wave. Ordinary waves occur when the electric field of the wave is entirely perpendicular to the optical axis, and extraordinary waves are when the electric field runs parallel to the optical axis.

The Pockels Effect

Up to this point, we have been examining the index ellipse of a material when no electric field is present. Friedrich Pockels defined the linear relationship between an applied electric field and the resulting change in the impermeability in 1894. The Pockels effect states that when an electric field is applied to an electro-optic material the impermeability matrix changes to $\overline{\overline{K}} = \overline{\overline{K}}_0 + \Delta\overline{\overline{K}}$, where $\overline{\overline{K}}_0$ is the impermeability defined in Equation 3.11 when no electric field is present and $\Delta\overline{\overline{K}}$ is the change induced by an applied electric field $\boldsymbol{F} = (F_1, F_2, F_3) = (F_x, F_y, F_z)$ according to Equation 3.14.

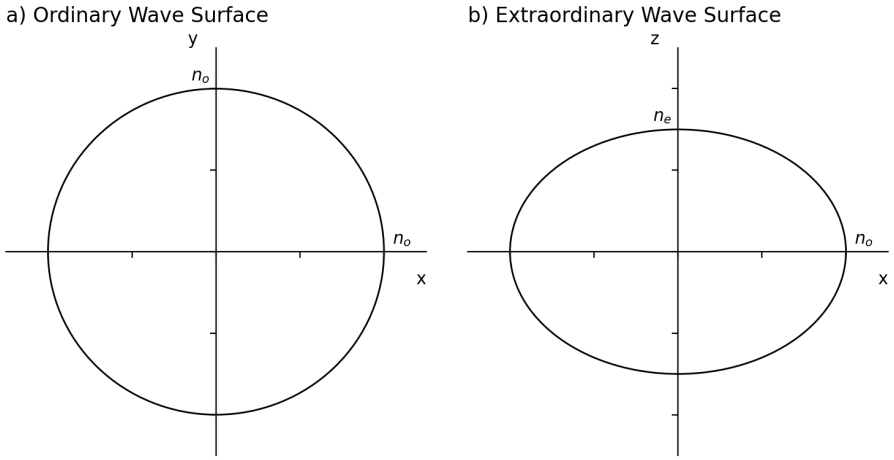

Figure 3.2: Diagram of wave surface of a) an ordinary wave and b) an extraordinary wave.

$j\backslash i$	1	2	3
1	1	6	5
2	6	2	4
3	5	4	3

Table 3.1: Matrix correspondence converting ij to l indices.

$$\varepsilon_0 \Delta K_{ij} = \sum_{k=1}^{3} K_{ijk} F_k \tag{3.14}$$

r_{ijk} are the Pockels coefficients, and due to symmetry within the crystal, the indices ij can be replaced with an index between 1 and 6 according to Table 3.1.

This reduces the set of $r_{ijk} = r_{Ik}$ to a 6×3 matrix, and Equation 3.14 can be expanded to Equation 3.15.

$$\varepsilon_0 \begin{bmatrix} \Delta K_1 \\ \Delta K_2 \\ \Delta K_3 \\ \Delta K_4 \\ \Delta K_5 \\ \Delta K_6 \end{bmatrix} = \begin{bmatrix} r_{11} & r_{12} & r_{13} \\ r_{21} & r_{22} & r_{23} \\ r_{31} & r_{32} & r_{33} \\ r_{41} & r_{42} & r_{43} \\ r_{51} & r_{52} & r_{53} \\ r_{61} & r_{62} & r_{63} \end{bmatrix} \begin{bmatrix} F_1 \\ F_2 \\ F_3 \end{bmatrix} \tag{3.15}$$

In order to reduce this set of coefficients to something more manageable, we have to examine the material that will be used.

Lithium Niobate

Lithium niobate ($LiNbO_3$) is a manufactured, naturally birefringent material discovered to be ferroelectric in 1949 and studied extensively for countless acoustic and optical uses [44]. At 633 nm, the index of refraction of $LiNbO_3$ is 2.297 along the ordinary axes and 2.208 along the extraordinary axis [43].

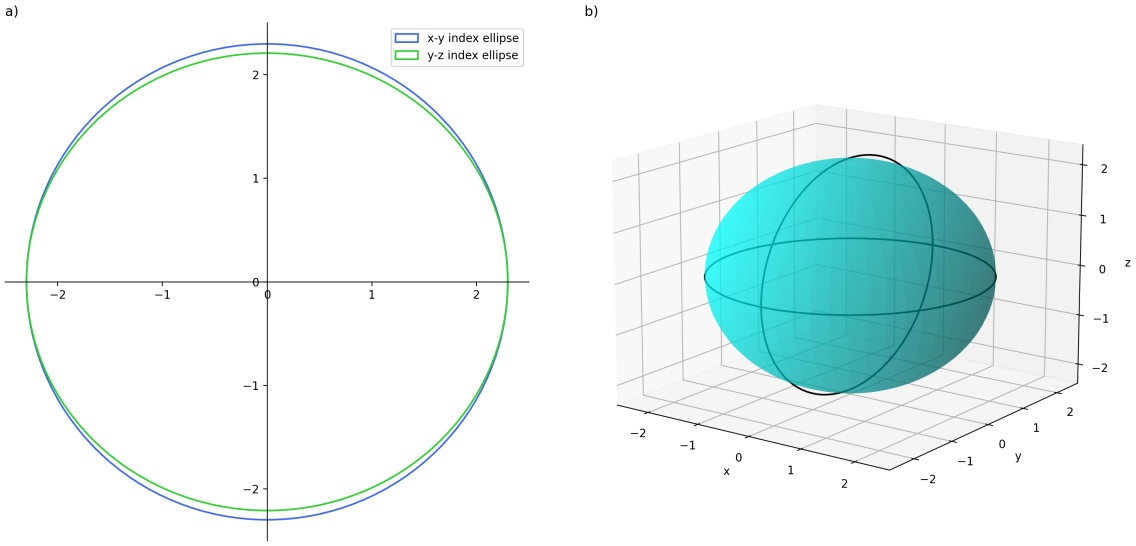

Figure 3.3: a) Index ellipses of $LiNbO_3$ in the x-y and y-z planes. b) Full index ellipsoid of $LiNbO_3$ with index ellipses of a non-birefringent material drawn on the cross-sections. Notice the gap along the y-z cross-section.

As $LiNbO_3$ has 3m point group symmetry within its crystal structure, we can determine that most Pockels coefficients become 0 while others are equivalent. Namely $r_{13} = r_{23}$, $r_{22} = -r_{12} = -r_{61}$ and $r_{42} = r_{51}$. This means only four coefficients are required to describe the electro-optic effect in $LiNbO_3$.

$$r_{Ik} = \begin{bmatrix} 0 & -r_{22} & r_{13} \\ 0 & r_{22} & r_{13} \\ 0 & 0 & r_{33} \\ 0 & r_{42} & 0 \\ r_{42} & 0 & 0 \\ -r_{22} & 0 & 0 \end{bmatrix} \tag{3.16}$$

For $LiNbO_3$ at 633 nm these values have been determined to be $r_{13} = 8.6 \times 10^{-12}\text{mV}^{-1}$, $r_{22} = 3.4 \times 10^{-12}\text{mV}^{-1}$, $r_{33} = 30.8 \times 10^{-12}\text{mV}^{-1}$, and $r_{42} = 28 \times 10^{-12}\text{mV}^{-1}$[44]. Using this result to determine $\overline{\overline{K}}$, we can determine the equation relating the electric field to the change in the index ellipsoid by completing Equation 3.12.

$$\overline{\overline{K}}_0 + \Delta\overline{\overline{K}} = \frac{1}{\varepsilon_0}\begin{bmatrix} \frac{1}{n_o^2} & 0 & 0 \\ 0 & \frac{1}{n_o^2} & 0 \\ 0 & 0 & \frac{1}{n_e^2} \end{bmatrix} + \frac{1}{\varepsilon_0}\begin{bmatrix} 0 & -r_{22} & r_{13} \\ 0 & r_{22} & r_{13} \\ 0 & 0 & r_{33} \\ 0 & r_{42} & 0 \\ r_{42} & 0 & 0 \\ -r_{22} & 0 & 0 \end{bmatrix}\begin{bmatrix} F_x \\ F_y \\ F_z \end{bmatrix} \tag{3.17}$$

$$\begin{aligned} \varepsilon_0 \sum_{i,j=1}^{3} K_{ij} c_i c_j &= 1 \\ x^2\left(\frac{1}{n_o^2} - r_{22}F_y + r_{13}F_z\right) + y^2\left(\frac{1}{n_o^2} + r_{22}F_y + r_{13}F_z\right) + z^2\left(\frac{1}{n_e^2} + r_{33}F_z\right) & \\ + 2xy\left(-r_{22}F_x\right) + 2xz\left(r_{42}F_x\right) + 2yz\left(r_{42}F_y\right) &= 1 \end{aligned} \tag{3.18}$$

In most EOMs, one can only apply an electric field to two of the axes of $LiNbO_3$. Most commonly, the z axis is chosen for the light to propagate through, while the x and y axes can be controlled. This reduced our index ellipse calculations to Equation 3.19.

$$x^2\left(\frac{1}{n_o^2} - r_{22}F_y\right) + y^2\left(\frac{1}{n_o^2} + r_{22}F_y\right) - 2xyr_{22}F_x = 1 \tag{3.19}$$

3.2.2 Rotating Half-wave Plate

We now possess the requisite information to emulate a rotating half-wave plate using an EOM containing a $LiNbO_3$ crystal. To understand how we might do this, we can examine how the index ellipse changes when we apply an electric field in the x or y direction.

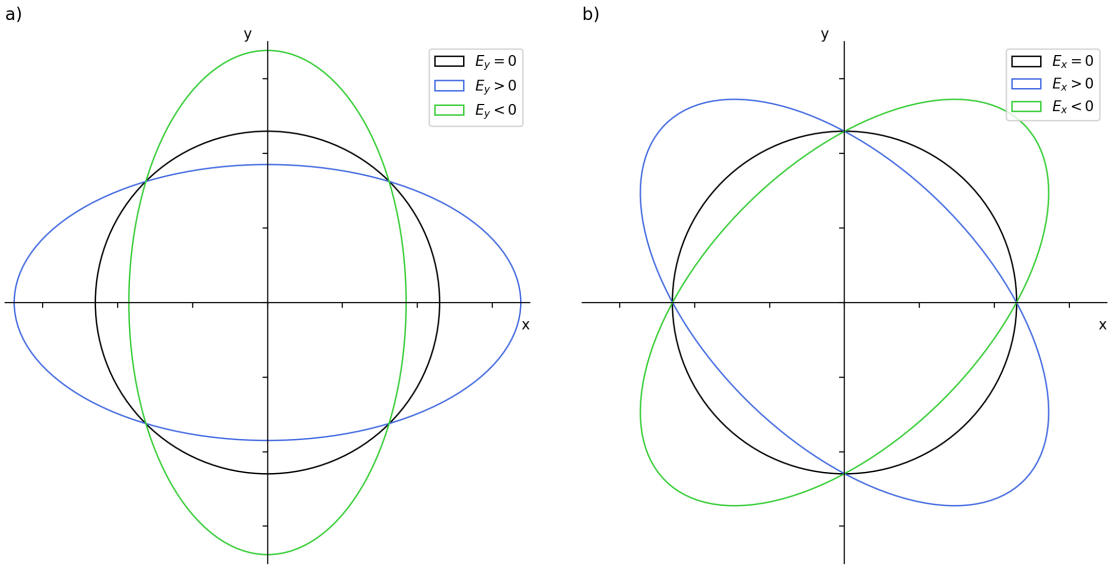

Figure 3.4: a) Diagram showing an index ellipse changing when an electric field is applied along the y-axis and b) diagram showing an index ellipse changing when an electric field is applied along the x-axis.

From Figure 3.4, we notice that when an electric field is applied only along the y-axis, the ellipse stretches and shrinks along the major axis according to Equation 3.20.

$$x^2\left(\frac{1}{n_o^2} - r_{22}F_y\right) + y^2\left(\frac{1}{n_o^2} + r_{22}F_y\right) = 1 \tag{3.20}$$

We can simplify this equation by redefining our indices of refraction along the x and y axis using Equations 3.21.

$$n_x = \frac{n_o}{\sqrt{1 - n_o^2 r_{22} E_y}} \qquad n_y = \frac{n_o}{\sqrt{1 + n_o^2 r_{22} E_y}} \tag{3.21}$$

This leaves our index ellipse varying according to Equation 3.22, which has the same form as when we examined birefringence without any applied electric field in Equation 3.12.

$$\frac{x^2}{n_x^2} + \frac{y^2}{n_y^2} = 1 \tag{3.22}$$

From Figure 3.4, we can also see that when an electric field is applied along the x direction, the major and minor axis of the ellipse no longer fall along the x and y axes, meaning that our equation for $\overline{\overline{\varepsilon}}$ (Equation 3.10) is no longer diagonalized. We chose a new set of axes that satisfies this requirement, reducing Equation 3.19 to Equation 3.24.

$$x = \frac{1}{\sqrt{2}}(x' - y') \qquad y = \frac{1}{\sqrt{2}}(x' + y') \tag{3.23}$$

$$x'^2\left(\frac{1}{n_o^2} - r_{22}F_x\right) + y'^2\left(\frac{1}{n_o^2} + r_{22}F_x\right) = 1 \tag{3.24}$$

This can be reduced similarly to Equation 3.22 using Equations 3.25.

$$n_{x'} = \frac{n_o}{\sqrt{1 - n_o^2 r_{22} E_x}} \qquad n_{y'} = \frac{n_o}{\sqrt{1 + n_o^2 r_{22} E_x}} \tag{3.25}$$

$$\frac{x'^2}{n_{x'}^2} + \frac{y'^2}{n_{y'}^2} = 1 \tag{3.26}$$

We can see in Figure 3.5 that along our newly defined axes, the index ellipse compresses and grows depending on the applied electric field.

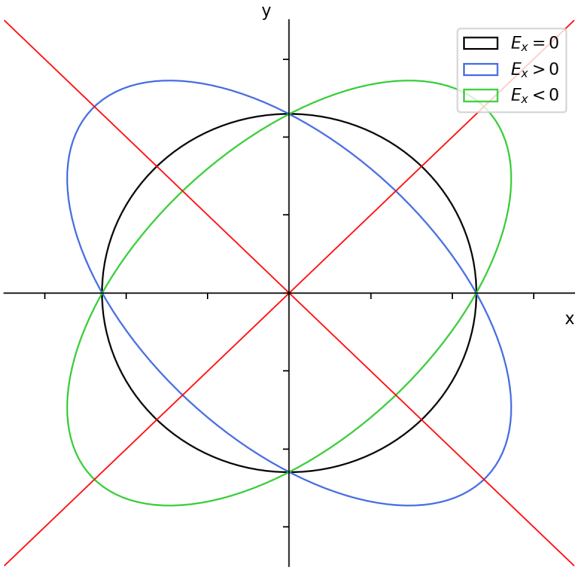

Figure 3.5: Diagram of an index ellipse varying under an electric field applied to the x-axis with new principle axes depicted in red.

Having examined the effects of electric fields in the x and y directions independently, we must examine what occurs when both are applied. We can see from Figure 3.6 that the major and minor axis of the ellipse continue to rotate depending on the amount of x or y electric field applied. We can choose a new principle axis that will account for this rotation using Equations 3.27.

$$x = x' \cos(\theta) - y' \sin(\theta) \qquad y = x' \sin(\theta) + y' \cos(\theta) \tag{3.27}$$

To examine this, we consider the case where a constant total electric field is applied to the system, but the proportion of x to y varies sinusoidally at a frequency ω (ie. $E_0^2 = E_x^2 + E_y^2$), this allows us to rewrite E_x and E_y in terms of E_0.

$$E_x = E_0 \sin(\omega t) \qquad E_y = E_0 \cos(\omega t) \tag{3.28}$$

Combining Equations 3.27 and 3.28 we can re-write the index ellipse.

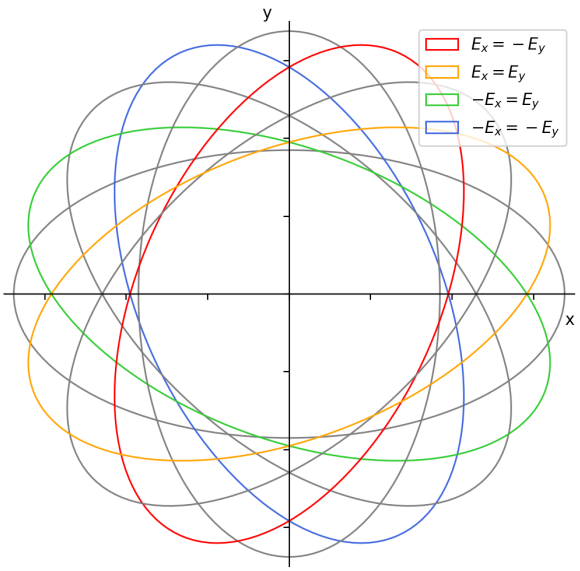

Figure 3.6: Diagram showing an index ellipse with the same height and width rotating through an angle of π. Ellipses shown in grey represent ellipses formed when the electric field is entirely along the x or y axis ($E_{tot} = E_x$ or E_y). Ellipses in colour are derived from instances when $E_{tot} = \sqrt{E_x^2 + E_y^2}$, so the total electric field is always constant.

$$x'^2\left(\frac{1}{n_o^2} - r_{22}E_0\cos(2\theta - \omega t)\right) + y'^2\left(\frac{1}{n_o^2} + r_{22}E_0\cos(2\theta - \omega t)\right) + 2x'y'r_{22}E_0\sin(2\theta - \omega t) = 1 \tag{3.29}$$

From this, we can see that the $x'y'$ term will be eliminated when $\theta = \frac{\omega t}{2}$ meaning that the principle axis rotates at half the frequency of the applied electric field and reducing our index ellipse in the rotating frame to be Equation 3.30.

$$x'^2\left(\frac{1}{n_o^2} - r_{22}E_0\right) + y'^2\left(\frac{1}{n_o^2} + r_{22}E_0\right) = 1 \tag{3.30}$$

We can isolate the indexes of refraction as we did previously to find $n_{x'}$ and $n_{y'}$.

$$n_{x'} = \frac{n_o}{\sqrt{1 - r_{22}E_0 n_o^2}} \approx n_o + \frac{1}{2} r_{22} E_0 n_o^3 \tag{3.31}$$

$$n_{y'} = \frac{n_o}{\sqrt{1 + r_{22}E_0 n_o^2}} \approx n_o - \frac{1}{2} r_{22} E_0 n_o^3 \tag{3.32}$$

The difference in the index of refraction between the fast and slow axis in this situation is $\Delta n = r_{22} E_0 n_o^3$ which we can use to determine what electric field will be required to emulate a half-wave plate or a π retardation along the slow axis compared to the fast axis ($\Gamma = \pi$).

$$\Gamma = \frac{2\pi l n}{\lambda} = \frac{2\pi l r_{22} E_0 n_o^3}{\lambda} \rightarrow E_0 = \frac{\lambda}{2 l r_{22} n_o^3} \tag{3.33}$$

Having determined the half-wave plate electric field, which can be achieved using a HWP voltage at some frequency $\frac{\omega}{2}$, we now have to determine how this rotation will achieve the results mentioned in Section 3.1

3.3 Frequency Shifting

We have now established that we intend to use a rotating HWP to remove the fine-structure splitting of a quantum dot and that we can emulate one using an EOM. However, we still need to address how a rotating HWP will remove the FSS. The process can be considered analogous to a Doppler shift that occurs when light reflects off a moving mirror. When a mirror moves towards a light source, any reflected light will have a higher frequency than it did at emission, and if the mirror moves away from the light source, the light will have a lower frequency upon reflection. This is an example of the conservation of momentum. In the case of a rotating HWP, we have to examine the angular moment of the system. Circularly polarized photons have SAM related to their polarization's handedness (or direction). Rotating waveplates have angular momentum vectors in the $+z$ or $-z$ direction, depending on their direction of rotation. If the SAM of the photon is in the same direction as the momentum vector of the waveplate, the photons will increase in frequency, and if they are in opposite directions, the photons will decrease in frequency.

The frequency conversion can be conveyed mathematically using Jones calculus. A circularly polarized photon will have an electric field vector relating to the direction of polarization and the angular frequency of the photon, ω_0.

$$\text{Right Polarized: } \begin{bmatrix} E_x \\ E_y \\ E_z \end{bmatrix} = \begin{bmatrix} E\cos(\omega_0 t) \\ E\sin(\omega_0 t) \\ 0 \end{bmatrix} \tag{3.34}$$

$$\text{Left Polarized: } \begin{bmatrix} E_x \\ E_y \\ E_z \end{bmatrix} = \begin{bmatrix} E\sin(\omega_0 t) \\ E\cos(\omega_0 t) \\ 0 \end{bmatrix} \tag{3.35}$$

As there is no electric field in the z direction, and we do not intend to add one, we can ignore this portion of the matrix in upcoming calculations. We know from Section 3.2.2 that our EOM has a rotating reference frame described by Equation 3.27, which we must apply to our photons. We will move forward only by examining the right polarized case for simplicity.

$$\begin{bmatrix} E_{x'} \\ E_{y'} \end{bmatrix}_{in} = \begin{bmatrix} \cos(\theta) & \sin(\theta) \\ -\sin(\theta) & \cos(\theta) \end{bmatrix} \begin{bmatrix} E\cos(\omega_0 t) \\ E\sin(\omega_0 t) \end{bmatrix} = \begin{bmatrix} E\cos(\omega_0 t - \theta) \\ E\sin(\omega_0 t - \theta) \end{bmatrix} \tag{3.36}$$

We also know that the $E_{x'}$ component will be retarded by an amount Γ compared to the $E_{y'}$ as we travel through the EOM. We divide this amount in two as the change occurs equal but opposite along the fast and slow axes.

$$\begin{bmatrix} E_{x'} \\ E_{y'} \end{bmatrix}_{out} = \begin{bmatrix} \cos\left(\frac{\Gamma}{2}\right) & \sin\left(\frac{\Gamma}{2}\right) \\ \sin\left(\frac{\Gamma}{2}\right) & -\cos\left(\frac{\Gamma}{2}\right) \end{bmatrix} \begin{bmatrix} E\cos(\omega_0 t - \theta) \\ E\sin(\omega_0 t - \theta) \end{bmatrix} = \begin{bmatrix} E\cos\left(\omega_0 t - \theta - \frac{\Gamma}{2}\right) \\ -E\sin\left(\omega_0 t - \theta - \frac{\Gamma}{2}\right) \end{bmatrix} \tag{3.37}$$

After the photon has passed through the EOM, we can rotate back to the laboratory frame.

$$\begin{aligned} \begin{bmatrix} E_{x'} \\ E_{y'} \end{bmatrix}_{out} &= \begin{bmatrix} \cos(\theta) & -\sin(\theta) \\ \sin(\theta) & \cos(\theta) \end{bmatrix} \begin{bmatrix} E\cos\left(\omega_0 t - \theta - \frac{\Gamma}{2}\right) \\ -E\sin\left(\omega_0 t - \theta - \frac{\Gamma}{2}\right) \end{bmatrix} = \begin{bmatrix} E\cos\left(\omega_0 t - 2\theta - \frac{\Gamma}{2}\right) \\ -E\sin\left(\omega_0 t - 2\theta - \frac{\Gamma}{2}\right) \end{bmatrix} \\ &= \begin{bmatrix} E\cos\left(\omega_0 t - 2\theta\right)\cos\left(\frac{\Gamma}{2}\right) + E\sin\left(\omega_0 t - 2\theta\right)\sin\left(\frac{\Gamma}{2}\right) \\ -E\sin\left(\omega_0 t - 2\theta\right)\cos\left(\frac{\Gamma}{2}\right) + E\cos\left(\omega_0 t - 2\theta\right)\sin\left(\frac{\Gamma}{2}\right) \end{bmatrix} \end{aligned} \tag{3.38}$$

Remembering from Section 3.1.1 that for our set-up, we are using a $\Gamma = \pi$ and a $\theta = \frac{\omega t}{2}$ we find that a fast rotating HWP spinning in the positive direction on a RCP photon will be down-converted and switched the have LCP output.

$$\begin{bmatrix} E\cos(\omega_0 t-\omega t)\cos\left(\frac{\pi}{2}\right)+E\sin(\omega_0 t-\omega t)\sin\left(\frac{\pi}{2}\right) \\ -E\sin(\omega_0 t-\omega t)\cos\left(\frac{\pi}{2}\right)+E\cos(\omega_0 t-\omega t)\sin\left(\frac{\pi}{2}\right) \end{bmatrix} = \begin{bmatrix} E\sin(\omega_0 t-\omega t) \\ E\cos(\omega_0 t-\omega t) \end{bmatrix} \tag{3.39}$$

This calculation can be simplified by combining the three operators that describe a rotating HWP into one unitary operator, Equation 3.40.

$$\begin{aligned} \frac{\lambda}{2}(\theta,\pi) &= \begin{bmatrix} \cos(\theta) & -\sin(\theta) \\ \sin(\theta) & \cos(\theta) \end{bmatrix} \begin{bmatrix} \cos\left(\frac{\pi}{2}\right) & \sin\left(\frac{\pi}{2}\right) \\ \sin\left(\frac{\pi}{2}\right) & -\cos\left(\frac{\pi}{2}\right) \end{bmatrix} \begin{bmatrix} \cos(\theta) & \sin(\theta) \\ -\sin(\theta) & \cos(\theta) \end{bmatrix} \\ &= \begin{bmatrix} -\sin(2\theta) & \cos(2\theta) \\ \cos(2\theta) & \sin(2\theta) \end{bmatrix} \end{aligned} \tag{3.40}$$

This process can be easily repeated to see what would occur if the waveplate was rotating in the other direction or if a LCP photon was input. The results are summarized in Table 3.2

Input Polarization	**θ Direction**	**Output Frequency**	**Output Polarization**
R	CCW	$\omega_0-\omega$	L
R	CW	$\omega_0+\omega$	L
L	CCW	$\omega_0+\omega$	R
L	CW	$\omega_0-\omega$	R

Table 3.2: Effects of a HWP rotating at a frequency ω on circularly polarized light

As a photon undergoes a change frequency, it also experiences a change in energy. Energy within a system must be conserved so we can surmise that rotating HWP analogue will increase or decrease in opposition to the photon. If we were using a physically rotating HWP the change in energy would appear as a change in rotation speed however when using an EOM the change will be in the electrical signal across the device. In the cases where the FSS is small enough that it cannot be resolved by a detector the change in energy would also not be able to be detected. As we cannot determine if a photon was up or down-converted in frequency, entanglement is preserved.

Chapter 4

Frequency Shifting

The theory outlined in Chapter 3 has been tested in parts for decades. Campbell and Steier outlined the effects of a $LiNbO_3$ crystal driven by both optimal and sub-optimal electrical signals on a laser beam in 1971. At the time, a frequency shift of 110 MHz required 194 Volts [45]. Since then, the design of EOMs has improved significantly so frequency shifting can be achieved using more manageable voltages. EOMs used to feature a large ($\approx 1 \times 1 \times 20$ mm) crystal with electrical traces being placed along all four sides of the crystal to allow electrical fields to propagate along the x and y-axis of the crystal. Modern EOMs feature a very small doped waveguide in the center of a larger $LiNbO_3$ waveguide, which allows the majority of the light to be concentrated in a much smaller area, and the electrical traces can be placed very close to the waveguide. This narrow separation between the waveguide and the electrodes significantly reduces the power requirements of these devices.

This work is an extension of research previously completed by Simon Daley [46], Michael Kobierski [47], and Turner Garrow [4]. Daley and Kobierski were able to show frequency shifting of laser light by 350 MHz with an efficiency of 93% [46]. However, these results could not be explained using the theory. Garrow, using another version of the EOMs, attempted to predict what factors would drive the EOM optimally and was able to up- and down-convert a 852 nm laser by 200 MHz with an efficiency of 80% [4]. However, frequency shifts of higher frequencies could not be achieved with the EOMs available because of low efficiency and concerns of overheating. This thesis aims to examine a range of EOMs to determine if we can reliably obtain high-efficiency shifting with any EOM.

4.0.1 EOMs

All of the EOMs examined in this thesis were custom-manufactured by SRICO. In all cases, we used an x-cut, z-propagating $LiNbO_3$ crystal with a zinc oxide (ZnO) diffused waveguide along one of the surfaces. This area forms a low-loss waveguide with low polarization selectivity. A layer of silicon dioxide (SiO_2) is deposited along the surface to passivate it, and three gold traces are deposited to run parallel to the waveguide. One trace is placed directly on top of the waveguide, which acts as a common ground for the device; the other two are laid equidistant from the waveguide and are used to apply voltages. Three different generations of EOMs were tested and used. The oldest generation, referred to as V1, are 4.5 cm long and have 10 μm thick gold traces. The second generation (V2) are 3 cm long and have 1 μm thick gold traces. The newest devices are again 4.5 cm long with 10 μm thick gold traces. Apart from the length and thickness of the gold traces, the cross-section of the devices are similar and both are shown in Figure 4.1.

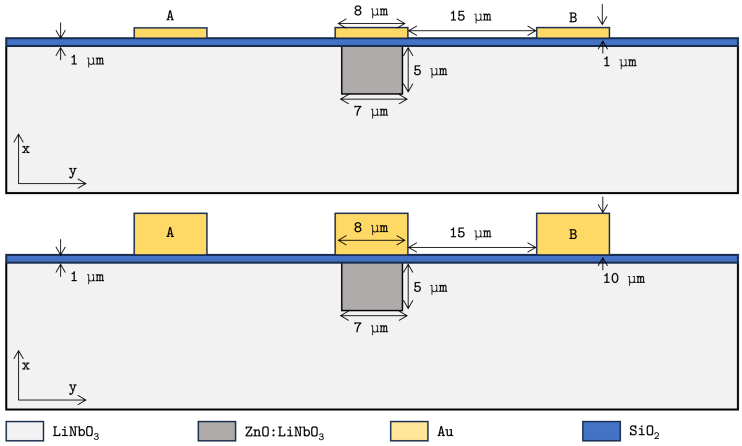

Figure 4.1: Cross-sectional diagrams of the EOMs with both the V2 EOMs with 1 μm thick gold traces (top), and the V1 and V3 devices with 10 μm gold traces (bottom).

In order to determine how best to drive these devices, a series of characterizations must be completed.

4.1 Device Characterization

There are four main components to the drive signal that must be determined for each device that I intend to use: frequency, voltage, phase, and DC bias.

4.1.1 Frequency

The first and simplest variable of the drive signal that has to be addressed is the frequency to operate the EOM at and, therefore, what frequency the photons will be shifted. As discussed in Chapter 3, the FSS can be removed by a frequency shift of $\frac{\delta}{2\hbar}$. So, determining the amount of FSS of a quantum dot will allow us to determine the drive frequency of the EOM. The process for determining the amount of FSS of a QD is well-described elsewhere[4, 48]. A measurement of a set of quantum dots similar to the ones used in my experiment found that over 50% of quantum dots had an FSS lower than 2 μeV [2]. However, a typical nanowire QD will have a FSS ranging between 2 and 10 μeV This means our EOMs generally have to operate in a range below 250 MHz, but an ideal EOM should be able to handle quantum dots with FSS up to 10 μeV.

4.1.2 Phase

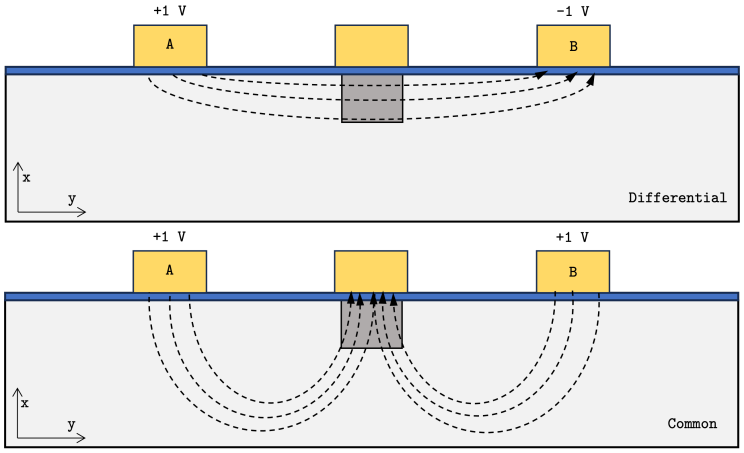

Figure 4.2: An EOM shown with both a differential (top) and a common (bottom) voltage applied to the traces. I observed that a differential voltage creates an electric field along the y-axis, and a common voltage creates a field along the x-axis.

As mentioned, the EOM has two traces that carry the signal along the length of the crystal. I needed to determine what the phase difference between these two traces must be to create a rotating wave plate. If the signals were perfectly in phase, the traces would always have a common voltage, and the electric field would be constantly aligned with the x-axis of the crystal. If the signals are perfectly out of phase (180°) the traces will always

have a differential voltage, meaning the electric field will be constantly aligned with the y-axis of the crystal. The effects of a common and a differential field are shown in Figure 4.2.

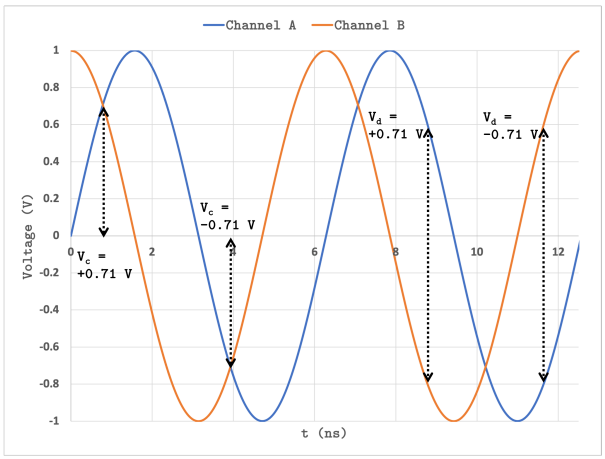

Figure 4.3: A drive signal for channels A and B with a 90° phase difference. The common and differential voltage at various points is marked. This shows that at this phase difference, the electric field rotates between the x and y direction.

In the ideal case, a 90° phase difference will allow the field to rotate by combining common and differential voltages, as shown in Figure 4.4. However, the 90° phase difference does not account for the asymmetry in field strength that might arise between the common and differential cases. To determine what asymmetry can be expected, a cross-section of the EOM was simulated using Quickfield Student. The dimensions were exactly as shown in Figure 4.1 apart from the gold traces being modelled as infinitely thin. Garrow found that by using the same voltage magnitude (±1 V), the common voltage yielded a field of E_x = 34.9 kV/m, and the differential voltage yielded E_y = 18.7 kV/m, meaning the common voltage is 1.87 times larger than the differential voltage. To compensate for this, we have to choose a phase that ensures E_y to be 1.87 times larger than E_x [4]. This requirement is satisfied by a phase difference of 123.7° calculated from Equations 4.1 and 4.2, where the phase is the ratio of α/β. This value may change based on individual devices, but it does determine that a phase difference of 90° cannot be expected.

$$V_A = V_c - V_d = |E|\sqrt{\frac{1}{\alpha^2} + \frac{1}{\beta^2}} \cos\left(2\omega - \arctan\frac{\alpha}{\beta}\right) \tag{4.1}$$

$$V_B = V_c + V_d = |E|\sqrt{\frac{1}{\alpha^2} + \frac{1}{\beta^2}} \sin\left(2\omega + \arctan\frac{\alpha}{\beta}\right) \tag{4.2}$$

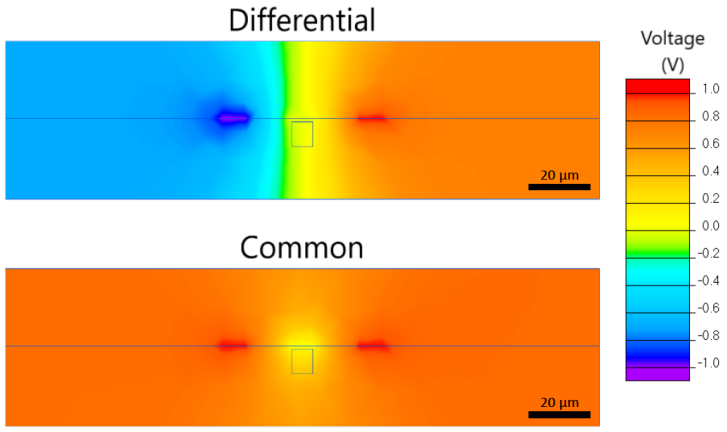

Figure 4.4: QuickField finite element method simulations of the EOMs when both a differential (top) and common (bottom) voltage of ±1 V is applied [4].

4.1.3 Voltage

Next, I must determine the voltage required to create the half-wave plate within the $LiNbO_3$ crystal. This can be determined mathematically or experimentally. Mathematically the HWP voltage of an EOM is related to several parameters of the crystal by the equation:

$$V_\pi = \frac{\lambda d}{2n_o^3 r_{22} L} \tag{4.3}$$

where λ is the wavelength of the photons to be shifted, d is the width of the waveguide in the direction of the electric field, and L is the length of the waveguide [45]. Using the parameters for the V3 EOM, I get a calculated voltage of 1.68 V. This equation assumes that the gold traces are placed directly next to the waveguide which is not true for our EOMs. It is also the case that the exact impedance of the traces is unknown and each of the ports on the EOM will reflect a certain amount of the signal. Both of these parameters will affect the necessary voltage and can be calculated, however, since they will change for each port on each device, it is easier to experimentally find the voltage required to create the HWP effect in an individual EOM.

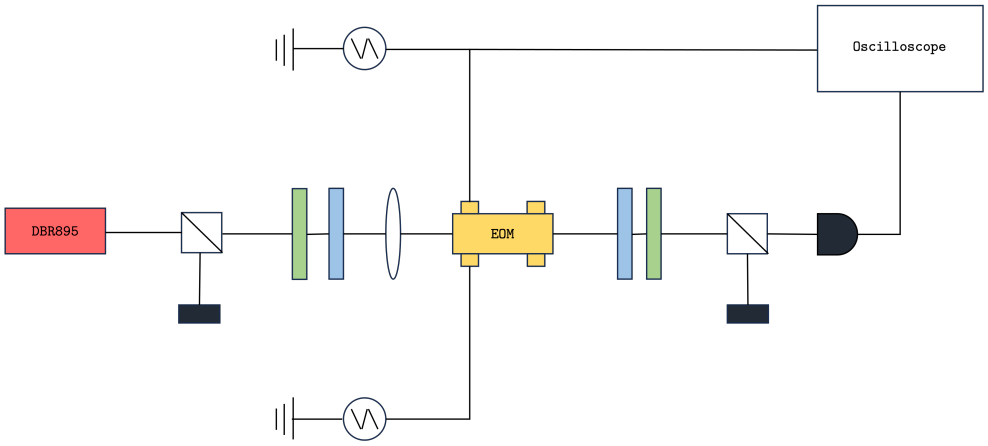

Figure 4.5: DC testing setup for the EOMs. In this setup, two voltage sources apply a slow-oscillating triangular wave to the traces of the EOM.

Experimentally, the HWP voltage can be measured using a simplified tomography setup shown in Figure 4.5. I used a ThorLabs DBR895PN diode laser, as the unique properties of a single-photon source are not required, and the higher counts from a laser makes this experiment faster and easier. I chose a laser with a wavelength similar to the wavelength that our QDs emit at (895 nm) because the frequency shifting process is wavelength dependant, and this allows for an easier transition to using the QDs. The laser light is sent through a polarizing beamsplitter (PBS), which is set only to allow horizontally polarized light to pass through. A HWP and QWP are then used to control what polarization of light is sent into the EOM. For a complete tomography experiment, I would need to examine all possible polarizations $\{H, V, A, D, R, L\}$. For my purposes, I only need to examine three input polarizations $\{H, D, R\}$ to perform a simplified tomography experiment. The polarized light is sent through an Olympus LMPLN5XIR objective lens and into the EOM in question. Two Stanford Research Systems DS345 synthesized function generators drive the EOM by providing a slow (10 Hz) oscillating triangle wave to each trace. By ensuring that these signals are 180 degrees out of phase from each other, a differential signal can be provided to the EOM. As mentioned in 4.1.2, a differential signal will create a voltage across a singular axis in the crystal. After the EOM, the light is sent through another HWP and QWP. These waveplates, in conjunction with another PBS, allow me to choose which polarization was measured.

Using the counts measured by a Tektronix DPO 4104 Digital Phosphor oscilloscope for each polarization, I can reconstruct how the polarization ellipse of the crystal changes as the voltage changes. This is done first by finding the Stokes parameters:

$$S_0 = \frac{H+V}{T} \qquad S_1 = \frac{H-V}{T} \qquad S_2 = \frac{A-D}{T} \qquad S_3 = \frac{R-L}{T}, \tag{4.4}$$

where T is the total number of counts and $\{H, V, A, D, R, L\}$ represents the counts of each corresponding polarization. The Stokes parameters are related to ψ and χ by:

$$\psi = \frac{1}{2}\tan^{-1}\left(\frac{S_2}{S_1}\right) \qquad \chi = \frac{1}{2}\sin^{-1}\left(\frac{S_3}{S_0}\right) \tag{4.5}$$

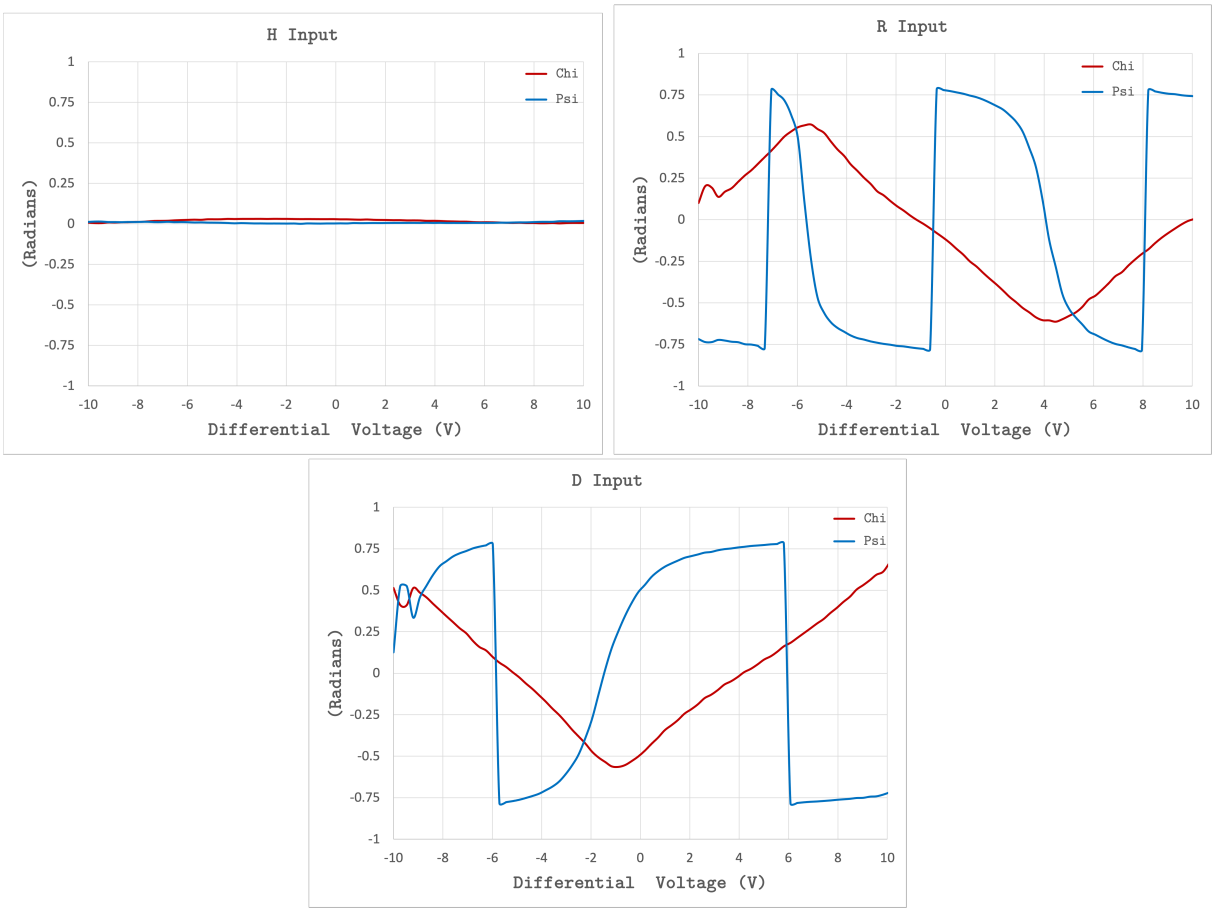

Figure 4.6: Results showing how an applied voltage on a V3 EOM affects the polarization ellipse of a photon. The ellipticity (χ) and orientation (ψ) angle of the output light are shown for three input polarizations. The EOM appears to act as a HWP at around ± 9 V.

The results from one of the V3 devices are shown in Figure 4.6. From these results, I can determine a few things. First, by examining the H input, I observe that the polarization does not significantly change as the voltage increases; this indicates that the fast and slow axis of the induced half-wave plate is well aligned with the laboratory frame. From the RCP input and D input, I observe that the EOM does have some built-in birefringence, as at 0 volts, the output polarization does not match the input polarization. This birefringence will be addressed in 4.1.4. Finally, the HWP voltage can be determined by examining the D and R input graphs and observing the voltage at which the polarization is precisely the opposite of what it was at 0 volts. This occurs around ±9 V. Garrow completed this procedure for one of the V2 EOMs (Figure 4.7) and found that the device achieved an HWP voltage at approximately ±7 V and had minimal built-in birefringence [4].

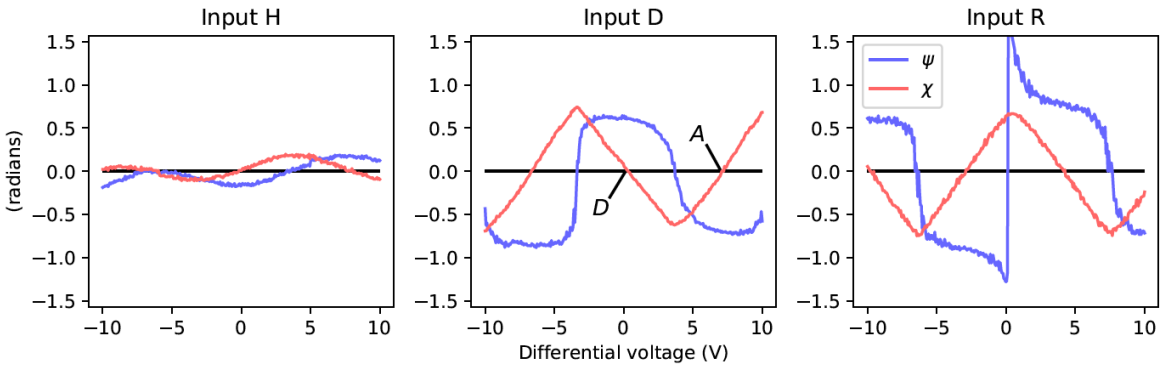

Figure 4.7: Results showing how a V2 EOM changes the polarization ellipse of a photon when a differential voltage is applied [4].The EOM appears to act as a HWP at around ±7 V.

There is some noise present in these graphs that arrives from the low sample rate of the oscilloscope (50 KS/s). The sample rate was doubled for all results shown after this point. Since both results were taken using a differential voltage, the peak-to-peak voltage (V_{pp}) to create the HWP effect in the EOMs must be calculated. For the V3 EOMs, the voltage required to create a differential voltage of 9 V assuming a phase difference of 123° is 10.2 V or a $V_{pp} = 20.2$ V and for a V2 EOM, a voltage of 7.93 V or a $V_{pp} = 15.86$ V is required, calculated from Equations 4.1 and 4.2.

4.1.4 DC Bias

As mentioned in Section 4.1.3, these EOMs show some amount of built-in birefringence. This birefringence can be addressed using a direct current (DC) bias applied to the trace. Determining this value for each EOM was relatively simple and could be done using the setup described in Figure 4.9. Using the QWP to send RCP light into the EOM and not applying any alternating current (AC) signal to the EOM, I used the QWP and PBS after the EOM to measure LCP. With no birefringence, there should be no LCP light measured. This was not the case with the majority of the devices tested. Using a BK Precision 1761 DC triple output power supply, which has two tunable voltage sources which can individually bias the two traces, I swept the voltages across each trace. The correct DC bias is determined when minimal LCP light is measured. Finding the DC bias was done before each data set was taken with an EOM because the DC bias fluctuates. Through observation, it appears that the bias shifts until the EOM had been running for a while at which point it stabilizes. This could be due to charge accumulation within the EOM. $LiNbO_3$ is a dielectric material, meaning it can be polarized by an external electric field. As the material is polarized, it produces its own internal electric field that opposes the DC bias. Dielectrics are also sensitive to temperature and humidity, which can explain why the necessary DC bias changes depending on the day [49].

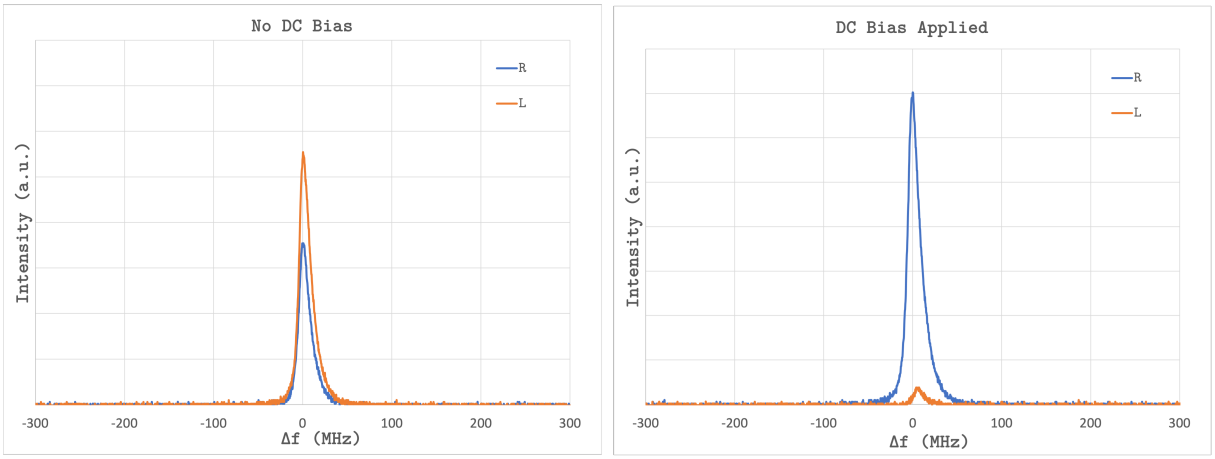

Figure 4.8: Intensity of light measured as RCP or LCP after travelling through an EOM with no AC signal both before a DC bias was applied (left) and after (right).

4.2 Laser Shifting

4.2.1 Experimental Setup

To test the devices, I used a ThorLabs DBR895PN laser, which emits light at a very narrow linewidth (1 MHz), allowing the frequency shifts to be observed. The setup is described in Figure 4.9 and features a PBS and QWP before the EOM, which allows me to control if I am sending in RCP or LCP photons. An Olympus LMPLN5XIR objective lens focuses the light onto the waveguide of the EOM. After the EOM, I can either direct the light into a Thorlabs DCC1545M-GL CMOS camera so I can measure and control the coupling into the $LiNbO_3$ waveguide, or to another QWP and PBS to allow for measurements of either RCP or LCP light. I then use a Thorlabs SA200-8B scanning Fabry-Perot cavity with a free spectral range of 1.5GHz and a resolution of 7.5MHz to measure shifts in frequency accurately. The Fabry-Perot cavity is connected to a piezo-electric transducer, which allows the cavity to change length when a voltage is applied. The cavity length determines what wavelength is transmitted to the photodiode detector. The photodiode and the voltage source send the signal to a Tektronix DPO 4104 Digital Phosphor Oscilloscope, where the correlation between voltage applied and transmitted wavelength can be used to determine the shifts in frequency.

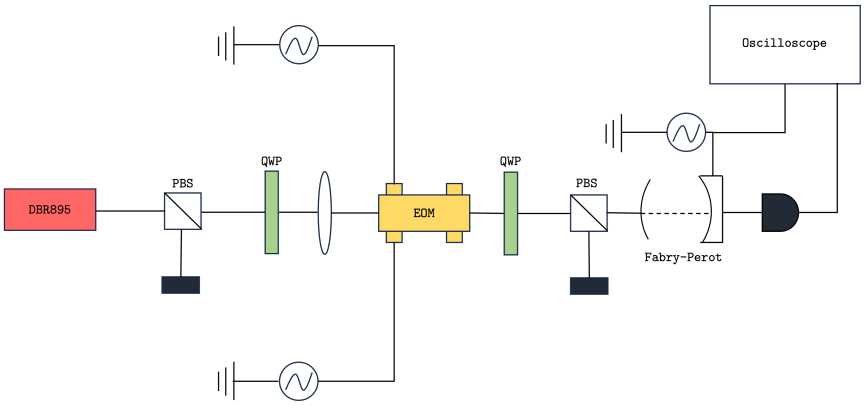

Figure 4.9: AC experimental setup for the EOMs. Here, an RF signal from the amplifiers and a DC bias are applied to each trace of the EOM. Before detection, photons are sent through a scanning Fabry-Perot cavity, which allows me to resolve small frequency shifts. The cavity is controlled by a slow oscillating triangle wave.

For the EOM to function as a rotating HWP, it also requires several electronic components. A pair of sinusoidal signals come from TI DAC38RF82, a dual channel digital to

analog converter (DAC) capable of generating RF signals up to gigahertz frequencies. I can control the frequency, phase and amplitude of the signal using custom-built Python code [50]. The DAC is only capable of producing a maximum power of 1.6 ± 0.1 dBm at 200 MHz, which is significantly lower than the power required to drive the EOMs. Therefore, each output of the DAC is sent through a Mini-Circuits ZHL-50W-52-S+ amplifier, which has a gain of 52 dB and a maximum output power of 47.5 dBm. To avoid damaging the amplifiers or the EOMs, a Pasternack PE8726 lowpass filter cuts off any signal over 400 MHz, and a set of Mini-Circuit attenuators lowers the maximum possible power output. The amount of attenuation depended on the version of EOM I was using. The EOMs with the thicker gold traces (V1 and V3) are more resilient against over-heating so an attenuation of 5 dB was used, whereas with the V2 devices an attenuation of 11 dB was implemented in an effort to protect the thinner gold traces.

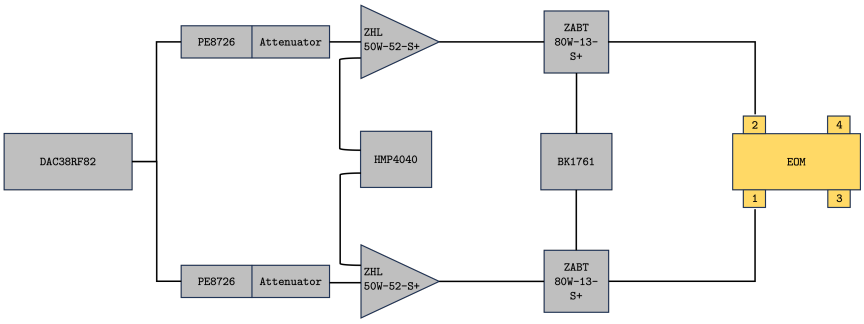

Figure 4.10: Electronic setup required to drive the EOM.

Both amplifiers are powered using a Rohde & Schwarz HMP programmable power supply with four output channels. A DC bias is added into the signals using a BK Precision 1761 DC power supply with two output ports capable of supplying ± 35 V. These signals are connected to the signals from the amplifiers using two ZABT-80W-13-S bias tees. Each signal is applied to one port of either trace. Then, I can choose between using a standing of a travelling wave mode by either leaving the other port of the trace open or terminating it with a 50 Ω terminator.

There are specific reason for using the standing wave mode or a travelling wave mode. The standing wave mode has both an amplitude anti-node (the point in a wave where the oscillation has the highest amplitude) and a current node (where the wave has no amplitude) at the open port. Operating at an amplitude anti-node allows the EOM to operate at a lower power as the photons interact with the part of the wave with the maximum power differential, and the current anti-node means the minimal current is travelling through the traces. A flow in current can cause Joule heating, which has caused the gold traces on

the EOMs to melt in the past [47]. A travelling wave mode does allow for a current flow and can cause Joule heating, which is the primary drawback of this setup. The benefit of a travelling wave mode as compared to the standing wave mode is that the photons and the signal travel together at approximately the same rate over the length of the EOM. In contrast, the standing wave mode, the photons are travelling, but the signal is not, meaning the photons could interact with the signal at various amplitudes over the length of the EOM. To observe if this could be a problem, it needs to determine if the transit time of the photon is significantly smaller than the oscillation period of the signal. The transit time is found using $t_t = \frac{n_o l}{c}$, where l is the length of the waveguide and c is the speed of light, and the oscillation period is found using $T = \frac{2\pi}{\omega}$, where ω is the frequency of the drive signal. Since, the transit time needs to be significantly shorter than the oscillation period, the equation $1 \ll \frac{2\pi}{\omega t_t} = \frac{2\pi c}{\omega n_o l}$ needs to be true. The worst-case scenario for our EOMs operating in the standing wave mode would be a frequency of 400 MHz (the highest frequency our electronics are rated for) with our longest EOMs which are 4.5 cm long.

$$\begin{aligned} 1 \ll & \frac{2\pi c}{\omega n_o l} \\ 1 \ll & \frac{2\pi(3 \times 10^8 \text{ m/s})}{400 \text{ MHz} \times 2.3 \times 4.5 \text{ cm}} \\ 1 \ll & 45.5 \end{aligned} \tag{4.6}$$

This inequality holds for the worst combination of factors, so the effects of the standing wave should not be a concern for my experiment. In an effort to avoid Joule heating, I will be primarily using the standing wave mode for my experiments.

4.2.2 Devices

The experimental setup for the FSS eraser requires two EOMs capable of high-efficiency frequency shifting, so I need to identify which of our EOMs would be able to meet this requirement. For each EOM available, I used the CMOS camera to make sure light could be sufficiently coupled to the waveguide, all traces were working correctly, and I analyzed the best frequency shifting that could be achieved.

Waveguide Coupling

Each device was imaged using a CMOS camera so I could observe the quality of coupling into the waveguide, the results are shown in Figure 4.11. While imaging the coupling, I

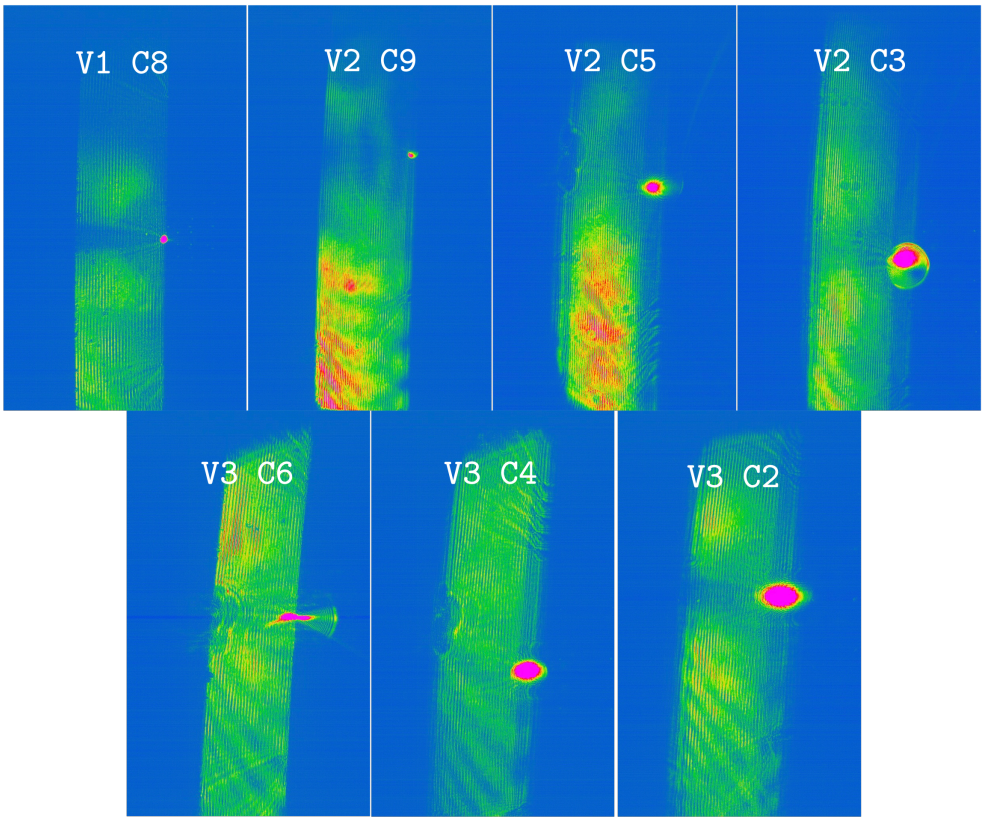

Figure 4.11: False colour images of the waveguide and $LiNbO_3$ chip taken by a Thorlabs DCC1545M-GL CMOS camera. In all the images, the bright pink spot represents the laser light travelling through the zinc-doped waveguide, and the green rectangular region is the bulk waveguide.

determined that some of our devices, namely V1 C8, V2 C9 and V3 C6, have very poor waveguide coupling. In the case of C8 and C9, this is most likely because of the ZnO dissipating due to the device overheating during previous tests [46]. Since C6 was not used before these tests, I know that cannot be the case and the waveguide must be broken or toherwise affected. During these preliminary tests, I also discovered that one of the traces in V2 C5 is broken, making it unusable. Again, this might have occurred during previous testing. This left me with three EOMs that could display high-efficiency shifting. To compare the EOMs, I examined the highest efficiency frequency shifting each EOM could achieve.

Frequency Shifting

To test the efficiency of frequency shifting of each device, I chose to use a constant frequency shift of 200 MHz. Each device was tested using incident RCP photons, and for completeness, each set of ports was tested. Since the EOMs are four-port devices with two ports being connected to a trace, I can either send the electrical signal in through ports 1 and 2 or ports 3 and 4. The location of the ports is shown in Figure 4.12.

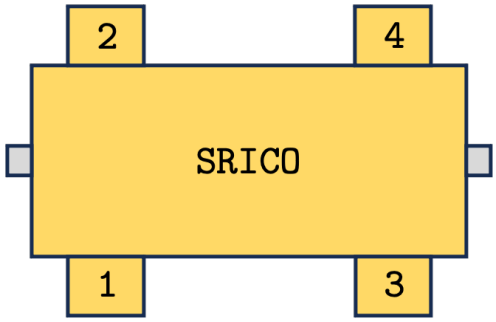

Figure 4.12: Diagram of the EOM with the location of the ports labelled. The waveguide is also shown in grey.

The EOMs are mounted in a fixed orientation, with the V2 devices having ports 1 and 2 at the front of the device or the entrance of the waveguide. The V3 devices were reversed with ports 3 and 4 at the front. For simplicity, moving forward, I will refer to the ports as the front or rear ports and the traces as the top or bottom trace. The top trace ran between ports 2 and 4 for the V3 EOMs and ports 1 and 3 for the V2 EOMs. I always tested using the same phase range for both the front and rear ports of each device, meaning that the same electrical signal will causing either an up or down conversion depending on which set of ports it is connected. In my tests, I examined up-conversion when using the front ports and down-conversion while using the rear ones.

Before each test, the DC bias required to remove the birefringence was found using the method outlined in Section 4.1.4. Once the bias has been found, I can optimize the phase and amplitude. Imbalances in the amplitude, phase and bias of the signal will cause multiple peaks to appear. EOMs are capable of shifting photons at integer multiples of the drive frequency. These are known as sidebands and can occur at $\{..., -2\omega, -\omega, 0, \omega, 2\omega, ...\}$. Optimization was performed using the custom-built Python script for the DAC. The frequency was set to 200 MHz, and initially, the phase between the traces was set to the predicted 123°. The amplitude was then slowly raised until the peak amount of shifting

was observed. Using that amplitude, the phase was then swept between 0 and 180° to optimize the shifting further. This process was repeated until the maximum efficiency was observed. The DAC reports the amplitude as a percentage of the maximum amplitude it is capable of producing, this information combined with the amplification and attenuation of the various electrical components between the DAC and the EOM allows me to calculate V_{pp} (Equation 4.7). These calculations were made assuming an impedance (Z) of 50 Ω. As mentioned in Section 4.1.3, the impedance of each device might not be exactly 50 Ω, however, I chose to make this assumption for simplicity. The efficiency of the frequency shifting was found by calculating the area under the peak of light shifted to the correct polarization and compared to the peak when the EOM is not driven.

$$V_{pp} = \sqrt{8 \times Z \times 10^{P_{\mathrm{dBm}}/10}} \tag{4.7}$$

The results from the V2 C3 EOM are shown in Figure 4.13. Using the front ports produced a maximum of 29.4% frequency up-shift using an amplitude of $V_{pp} = 35.1 \pm 0.4$ V, a phase of $\phi_{t\to b} = 113°$ and a DC bias of 6.05 V along the top trace (V_t). When using the rear ports, 88.4% of the photons were down converted using $V_{pp,t} = 31.0 \pm 0.4$ V, $V_{pp,b} = 37.1 \pm 0.4$ V, $\phi_{t\to b} = 113°$, $V_t = 1.47$ V and $V_b = -3.17$ V. The V3 C2 EOM displayed very poor frequency shifting, as shown in Figure 4.14. The front ports displayed 16.6% up-conversion using $V_{pp} = 53.7 \pm 0.6$ V, $\phi_{t\to b} = 118°$, and $V_t = 9.3$ V. Using the rear ports I saw 14.1 % of light down-converted using the same amplitude and phase but a DC bias of $V_t = 10.2$ V. The final EOM to be tested was the V3 C4 device. The results, shown in Figure 4.15, using the front ports are similar with a frequency up-conversion of 42.8% using $V_{pp} = 53.7 \pm 0.6$ V, $\phi_{t\to b} = 113°$, and $V_t = 17.29$ V. When using the rear ports, I observe a frequency down-conversion of 46.8% using the same amplitude and phase as the previous test.

The most efficient device was V2 C3, so I will use this device for the majority of the experiments. It is also worth noting that this device was the only one where the port I was using made a significant impact on the performance of the device. It is possible that there was some damage to one of the ports, creating this imbalance.

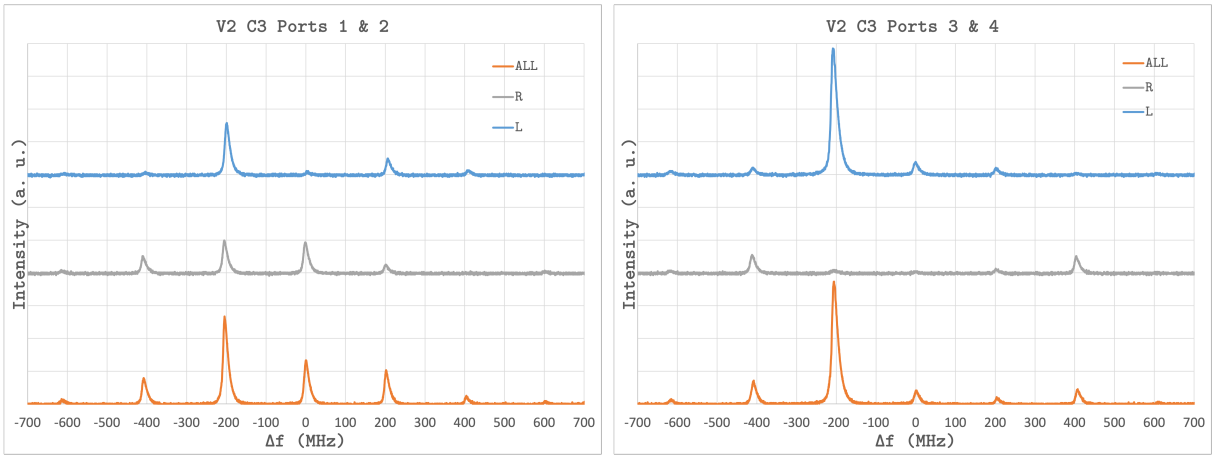

Figure 4.13: Frequency shifting results when using the V2 C3 EOM. The front ports (left) were driven using $V_{pp} = 35.1 \pm 0.4$ V, $\phi_{t\to b} = 113°$, and $V_t = 6.05$ V to achieve a up-conversion efficiency of 29.4%. The rear ports (right) achieved a frequency down-conversion of 88.4% using a signal of $V_{pp,t} = 31.0 \pm 0.4$ V, $V_{pp,b} = 37.1 \pm 0.4$ V, $\phi_{t\to b} = 113°$, $V_t = 1.47$ V, and $V_b = -3.17$ V.

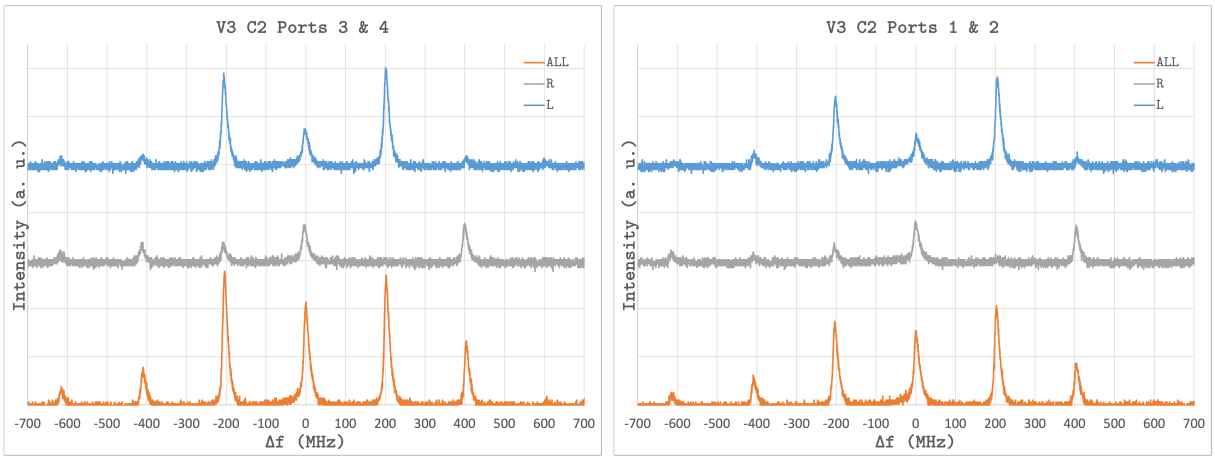

Figure 4.14: Frequency shifting results for the V3 C2 EOM. The front ports (left) achieved a 16.6% up-conversion using a signal of $V_{pp} = 53.7 \pm 0.6$ V, $\phi_{t\to t} = 118°$,and $V_t = 9.3$ V. The rear ports (right) had an efficiency of 14.1% down-conversion using a signal of $V_{pp} = 53.7 \pm 0.6$ V, $\phi_{t\to b} = 118°$,and $V_t = 10.2$ V.

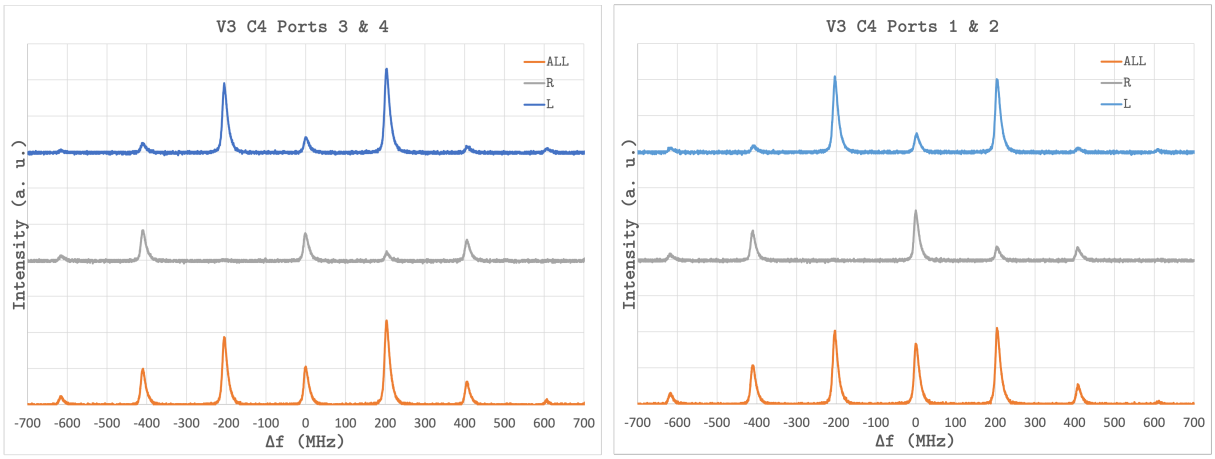

Figure 4.15: Frequency shifting results for the V3 C4 EOM. Using the front ports I saw a frequency up-conversion of 42.8% using a single of $V_{pp} = 53.7 \pm 0.6$ V, $\phi_{t\to b} = 113°$, and $V_t = 17.29$ V. With the rear ports 46.8% of the light was down-converted using a signal of $V_{pp} = 53.7 \pm 0.6$ V, $\phi_{t\to b} = 113°$,and $V_t = 17.17$ V.

Frequency Dependence

Since the EOM should be able to remove the FSS from a wide range of quantum dots, we need them to operate at a range of frequencies at similar efficiency. From the previous experiments, I know that at 200 MHz, the V2 C3 EOM can down-convert 88.4% of light. I used the same ports for each experiment and the same process to find the optimal shifting. I discovered that as the frequency increased, a lower amplitude was required to reach peak shifting. However, the efficiency also decreased significantly. The results from these tests are shown in Figure 4.16. At 250 MHz, the efficiency is reduced to 80.8% and 77.7% at 300 MHz. At these frequencies, the EOM could still be useful, but at 350 MHz, the efficiency reduces to 43.9%, making this FSS removal method no longer functional. As stated in Section 4.1.1, approximately half of our QDs only require a frequency shift of < 250 MHz, so this EOM could be used.

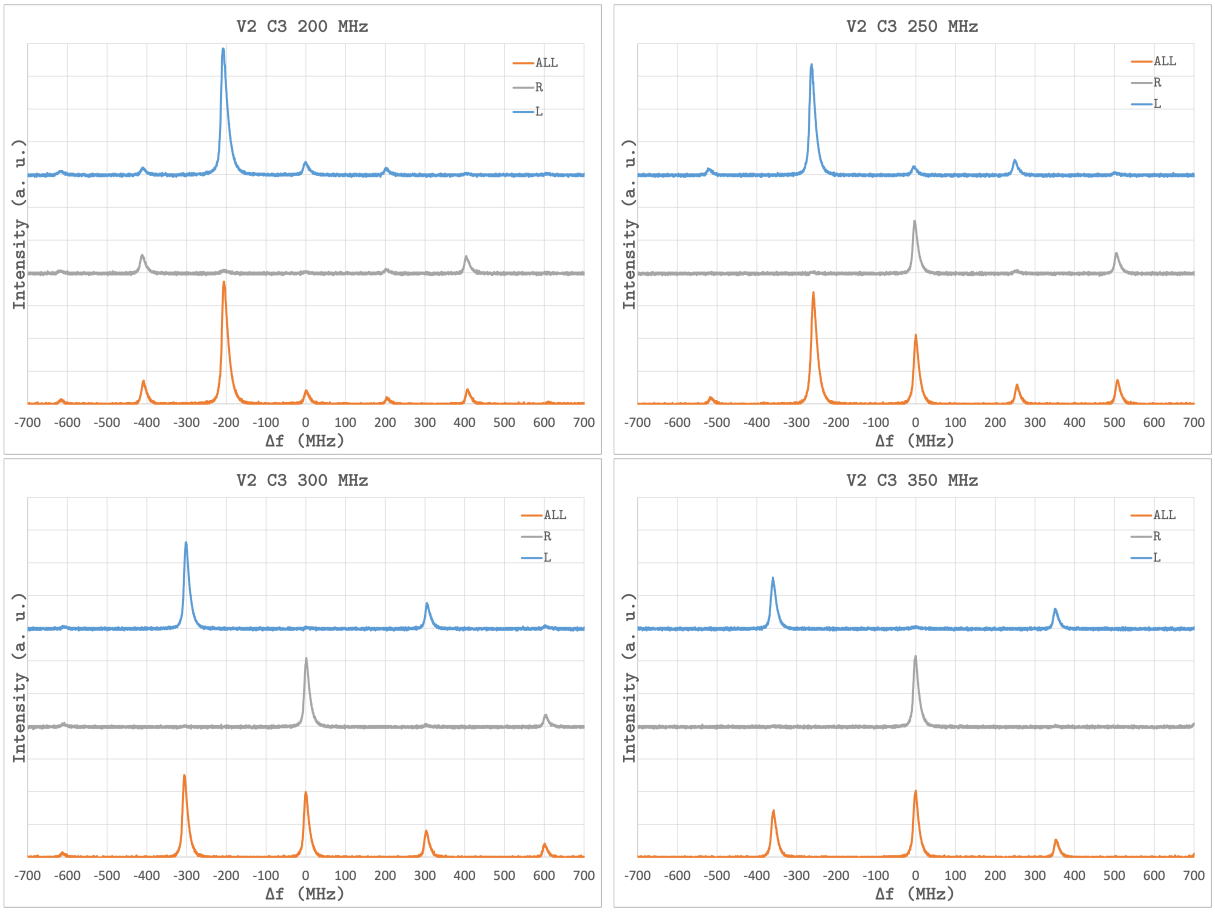

Figure 4.16: Results for frequency down-conversion over a range of frequencies for the V2 C3 EOM. At 200 MHz (top-left), 88.4% of photons were shifted using a signal of $V_{pp,t} = 31.0 \pm 0.4$ V, $V_{pp,b} = 37.1 \pm 0.4$ V, $\phi_{t\to b} = 113°$, $V_t = 1.47$ V, and $V_b = -3.17$ V. At 250 MHz (top-right), 80.8% of photons were shifted using a signal of $V_{pp,t} = 34.0 \pm 0.4$ V, $V_{pp,b} = 31.5 \pm 0.4$ V, $\phi_{t\to b} = 96°$, and $V_b = -12.65$ V. At 300 MHz (bottom-left), 77.7% of photons were shifted using a signal of $V_{pp,t} = 23.4 \pm 0.3$ V, $V_{pp,b} = 24.9 \pm 0.3$ V, $\phi_{t\to b} = 109°$, $V_t = 1.47$ V, and $V_b = -7.12$ V. Lastly at 350 MHz (bottom-right), 43.9% of light was shifted using a signal of $V_{pp,t} = 18.8 \pm 0.2$ V, $V_{pp,b} = 18.3 \pm 0.2$ V, $\phi_{t\to b} = 109°$, and $V_b = -9.22$ V.

After observing how much the frequency affected the efficiency of the V2 C3 EOM, I decided to test if this was true for the V3 devices and if there was a different optimal frequency for these newer devices. As shown in Figure 4.17, the shifting efficiency decreased

as the frequency increased, from 46.8% at 200 MHz to 20.7% at 350 MHz. This confirmed that 200 MHz was the optimal frequency shift for both V2 and V3 devices.

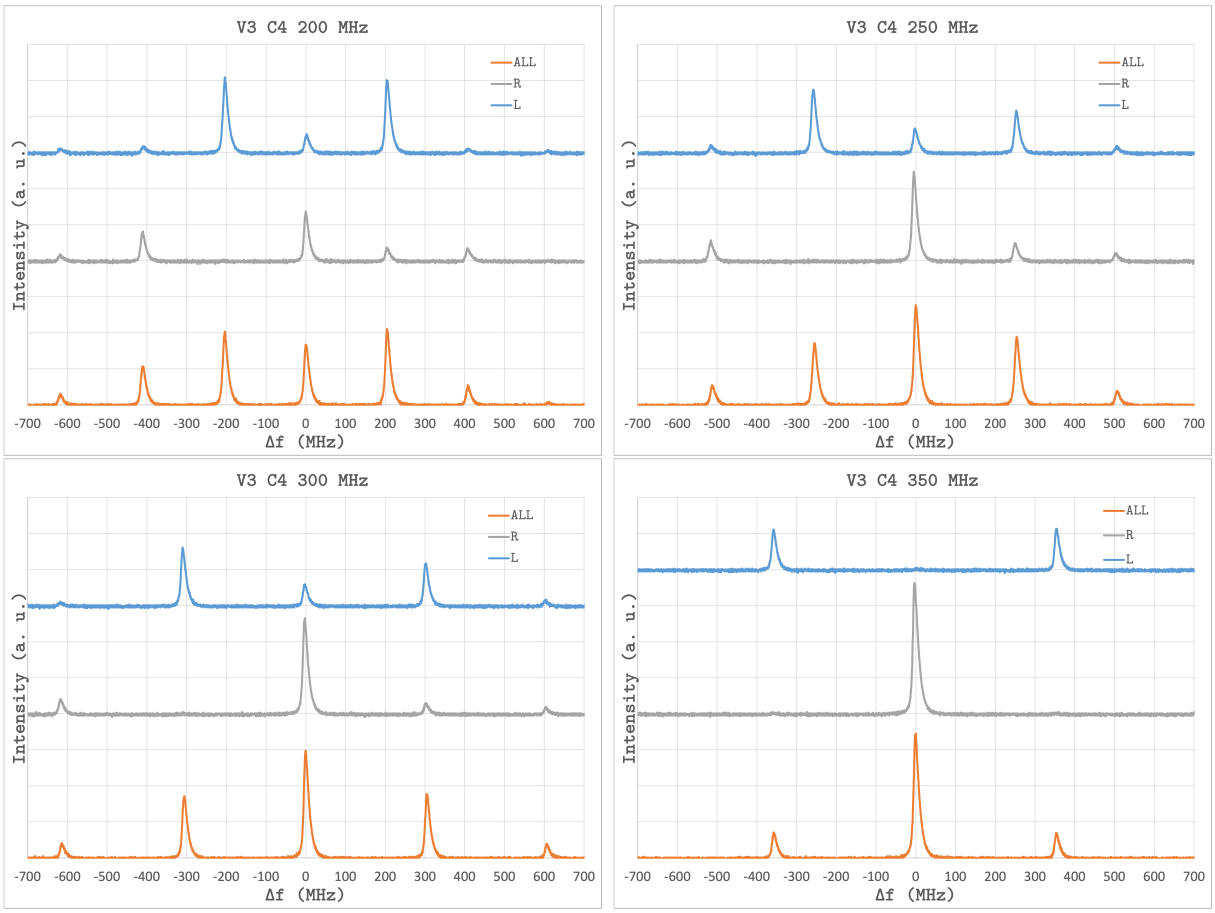

Figure 4.17: Results for frequency down-conversion over a range of frequencies for the V3 C4 EOM. At 200 MHz (top-left), 46.8% of photons were shifted using a signal of $V_{pp} = 53.7 \pm 0.6$ V, $\phi_{t\to b} = 113°$, and $V_t = 17.17$ V. At 250 MHz (top-right), 38.5% of photons were shifted using a signal of $V_{pp} = 47.7 \pm 0.6$ V, $\phi_{t\to b} = 96°$, and $V_b = -12.65$ V. At 300 MHz (bottom-left), 33.3% of photons were shifted using a signal of $V_{pp} = 37.5 \pm 0.4$ V, $\phi_{t\to b} = 75°$, and $V_t = 17.17$ V. Lastly at 350 MHz (bottom-right), 20.7% of light was shifted using a signal of $V_{pp} = 28.4 \pm 0.3$ V, $\phi_{t\to b} = 113°$, and $V_t = 20.27$ V.

I can observe from these tests that the amplitude required to reach peak efficiency changes according to the frequency. As we know from Equation 4.3, the V_π of the EOM is not frequency dependant so I do not expect to observe a decrease in the required amplitude.

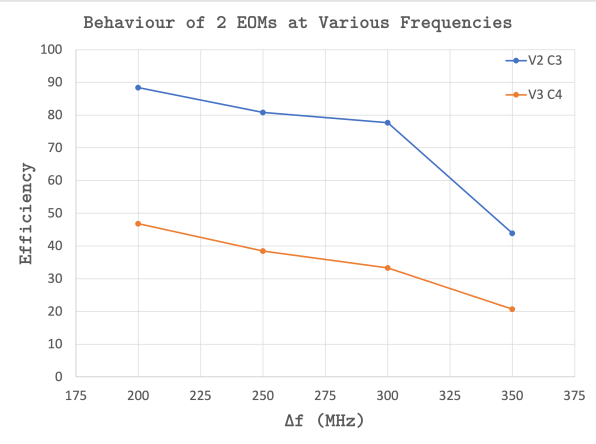

Figure 4.18: Efficiency frequency shifting of both V2 C3 and V3 C4 at frequencies between 200 and 350 MHz.

However, this frequency dependence might be explained by the scattering parameters or s-parameters of the ports on the device. Whenever a signal in incident on a port some of the signal will be reflected and some will be transmitted. The amount of signal that is reflected is dependant on the frequency of the signal. I can conclude from my observations that at higher frequencies the amount of reflected signal decreases so less power is required to reach the HWP voltage. This dependence is not accounted for in the characterization test I performed in Section 4.1.3. Luckily, doing a complete sweep to find the optimal voltage is a quick process and could be completed easily without ever attempting the characterization. This however does not account for the reduction in efficiency. I found in Section 4.2.1, that even when using a standing wave setup these EOMs should be capable of shifting at higher frequencies. However, for completeness, I should examine a travelling wave setup to determine if this could be contributing to the reduction in efficiency.

Standing vs. Travelling Wave

As discussed in Section 4.2.1, using a travelling wave could increase the efficiency of frequency shifting at higher frequencies. As I was concerned with the possibility of Joule heating melting the thin gold traces on the V2 C3 device, I used the V3 C4 device and tested it with and without a terminator at both 200 and 300 MHz, results are shown in Figure 4.19. The terminator used was a Pasternack PE6232 50 W RF Terminator. For both frequencies, the efficiency decreased; at 200 MHz, it reduced to 27.8% from 46.8%, and at 300 MHz, the efficiency reduced from 33.3% to 12.4%. It is unclear where this

overall reduction in efficiency comes from. I can also observe that using either standing or travelling waves the efficiency decreased at the higher frequency. From this I can conclude that the results from the calculation in Equation 4.6, are accurate but I still don't know why the efficiency reduces at higher frequencies.

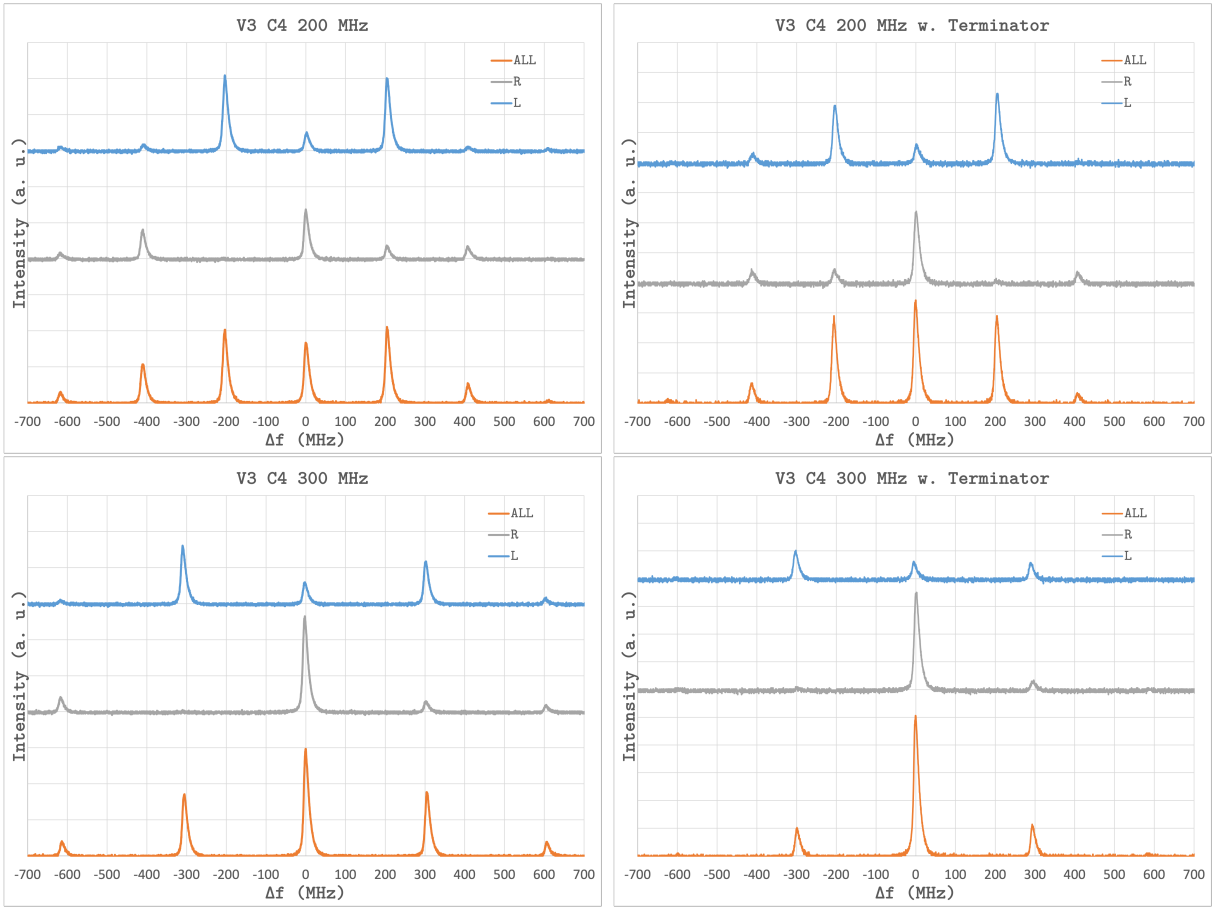

Figure 4.19: Results when using the V3 C4 EOM with and without a 50 W terminator. At 200 MHz with no terminator (top-left), 46.8% of light was down-converted using a signal of $V_{pp} = 53.7 \pm 0.6$ V, $\phi_{t\to b} = 113°$, and $V_t = 17.17$ V. With a terminator (top-right), 27.8% shifting was achieved using a signal of $V_{pp} = 47.7 \pm 0.6$ V, $\phi_{t\to b} = 113°$, and $V_t = 15.42$ V. At 300 MHz with no terminator (bottom-left), 33.3% of light was shifted using a signal of $V_{pp} = 37.5 \pm 0.4$ V, $\phi_{t\to b} = 75°$, and $V_t = 17.17$ V. Finally at 300 MHz with a terminator (bottom-right), 12.4% of light was down-converted using a signal of $V_{pp} = 37.5 \pm 0.4$ V, $\phi_{t\to b} = 104°$, and $V_t = 17.83$ V.

Stability

For the EOM to be a functional solution to removing the FSS, it has to be able to maintain high efficiency shifting for an extended period without losing efficiency or overheating. To test this, I set the EOM to the ideal parameters I had found previously, and the DC bias that was determined. Data was taken at the setup and an hour later. At t = 0 min, the shifting efficiency was found to be 83.9%, and at t = 60 min, the efficiency was reduced to 75%. The loss in efficiency is most likely related to charge accumulation within the crystal, causing the DC bias required to remove the birefringence to shift.

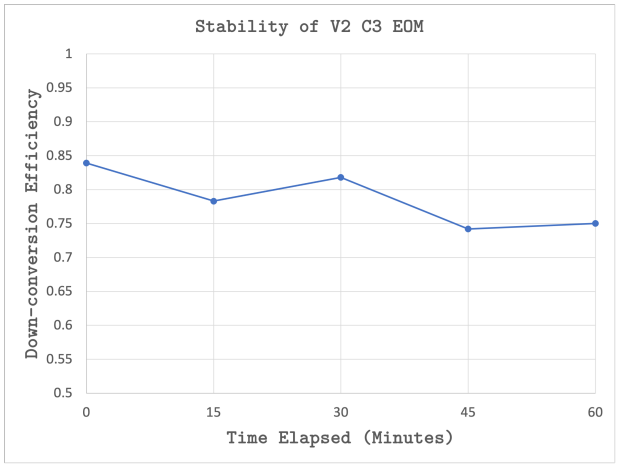

Figure 4.20: Frequency down-conversion using the V2 C3 EOM immediately after setup (left) and an hour later (right). The electrical signal was $V_{pp,t} = 31.0 \pm 0.4$ V, $V_{pp,b} = 37.1 \pm 0.4$ V, $\phi_{t\to b} = 113°$, and $V_b = -11.77$ V for both test. The efficiency at $t = 0$ min was 83.9%, and at $t = 60$ min, the efficiency was reduced to 75%.

Effects of an imperfect signal

I also tested how minor deviations from the optimal drive signal affected the efficiency in Figure 4.21. Using the V2 C3 EOM, the device displayed the highest efficiency shifting, I first used a phase 10° higher than the optimal 113°, and the efficiency was reduced to 61.8%. Next, the amplitude was increased by 3%. In this case, the efficiency only decreased slightly to 87.8%. Finally, the DC bias was removed, and again, I saw a significant reduction in efficiency to 66.8%. In all of these cases, the amount of light shifted to a higher-order sideband increased, as shown in Table 4.1. A paper written by Campbell and Steiner goes

into significantly more depth and mathematically examines the results of an imperfect drive signal [45].

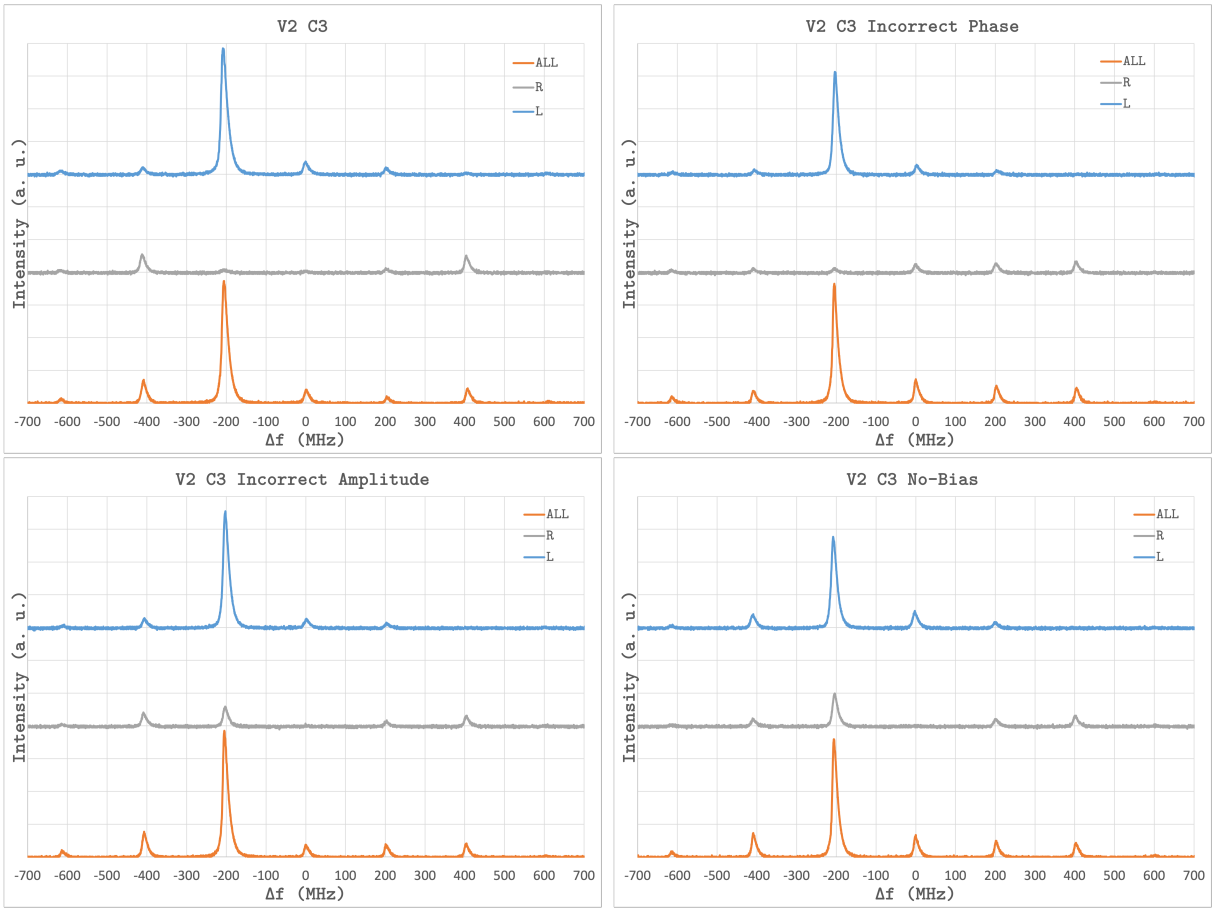

Figure 4.21: Effects of an imperfect drive signal. Shown are the results using the optimal drive signal (top-left), a higher phase (top-right), an increased amplitude (bottom-left), and an incorrect DC bias (bottom-right).

I did not observe what might be causing the persistent sidebands in the V3 EOMs. It is possible that a crystal cut slightly off-axis would cause sidebands as we would be unable to induce a consistent HWP throughout the length of the EOM leading to some photons to be shifted to a sideband other than the one the drive signal is optimized for and some photons to be entirely unaffected.

	-2ω	$-\omega$ (LCP)	$-\omega$ (RCP)	0	ω	2ω
Optimal	11.8%	88.4%	0.3%	6.4%	2.0%	6.6%
$\phi_{t\to b} + 10°$	5.3%	61.8%	1.0%	11.2%	8.1%	6.6%
$V_{pp} \times 1.3$	14.5%	87.8%	11.3%	6.2%	6.2%	6.6%
$V_{t,b} = 0$ V	13.0%	66.8%	20.7%	12.1%	8.1%	7.1%

Table 4.1: Results of frequency down-conversion using an imperfect signal on each of the five main sidebands.

Input polarization

Finally, I also examined the optical signal when I send in LCP photons; up until this point, I have only been examining RCP input photons. I expect most of the photons to be up-converted and RCP after the EOM. Using the same drive signal that was found to be optimal for RCP input photons, it was found that 70.7% of photons were up-converted. This indicates that the optimal drive signal for one input polarization might not be optimal for the other. I can also clearly observe that in both cases, the EOM is acting as a HWP, as the RCP input has a predominantly LCP output and vice versa.

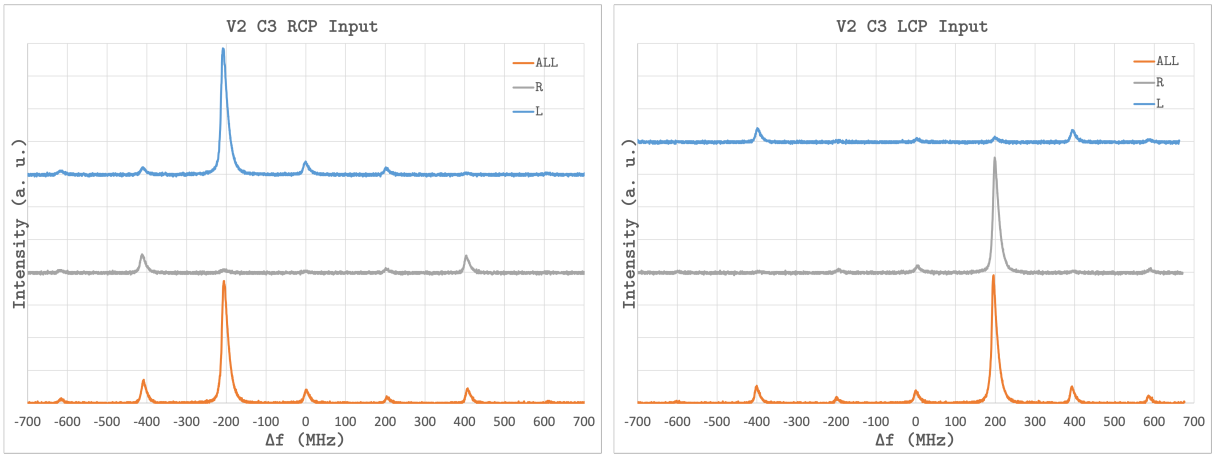

Figure 4.22: Results of the same drive signal when both RCP photons (left) and LCP photons (right) are used as input. RCP down-conversion had an 88.4% efficiency, and LCP up-conversion had an efficiency of 70.7%.

Through these experiments, I have shown that removing the FSS from a QD could be achieved, but more research into why some EOMs appear to work better than others needs to be completed.

Chapter 5

Integrated Optics

Alongside developing an ideal entangled photon source, we also need to examine ways to build quantum circuits. In the typical lab setting, this is done using bulk optics, where a simple algorithm can require dozens of components and take up a significant amount of space on an optics table. A solution can be found in the field of classical computing. The first patent for integrated computer chips was filed by J. S. Kilby in 1964, and they have become smaller and more compact as the technology around transistors has improved [51, 52]. In 2004, it was discovered how light could be harnessed in a chip in similar ways to electricity, and the field of integrated optics grew quickly [53]. Today, most data centres use integrated optics for fast and effective data transfer and processing. In 2008, Politi et al. put the first quantum circuit on an optical chip and proved that complicated bulk quantum circuits could be miniaturized onto a single chip [54].

Since the field of integrated optics is mature, many resources are already available for large and small-scale development of optical chips, including open-source libraries for optical components, tape-out and simulation software for designing chips, and pre-built rigs for testing chips. This well-developed infrastructure makes creating optical chips easy, however, we run into a significant issue: the majority of the infrastructure has been designed specifically for light at a telecom wavelength, most commonly 1550 nm, with 1350 nm as a common alternative. The quantum dots used in our lab primarily emit light in the near-infrared spectrum, 895 nm specifically. Unfortunately, this wavelength is outside the window of transparency of silicon [5]. To combat this, we can use an alternative material that foundries provide increasing support for silicon nitride (SiN). An added benefit to switching to SiN is the lower light loss of the material, which is beneficial as we switch to single photons for quantum applications.

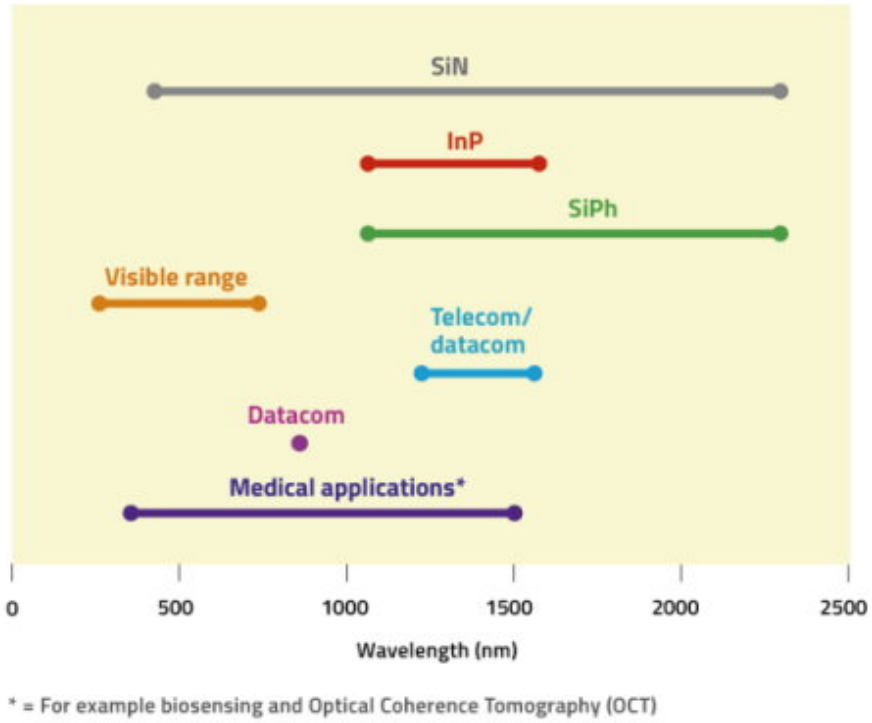

Figure 5.1: Transparency window of SiPh, SiN, and InP, as well as the common ranges for a variety of applications [5].

However, no open-source SiN libraries of pre-made and tested components are optimized for 895 nm. Our lab set out to develop a basic set of components to build circuits for our lab to test and use. We designed these components in collaboration with the silicon electronic-photonic integrated circuits (SiEPIC) program, a program developed to train researchers in creating integrated silicon photonic chips. We added the components to the SiEPIC EBeam library, an open-source personal development kit (PDK), where anyone can access and use the developed components.

5.1 Waveguide

The most basic of optical components is the waveguide. A waveguide acts as a pipeline between optical components and needs to transport light efficiently with low loss. There are three primary types of optical loss: sidewall scattering, radiation loss, and mode mismatch. Waveguides are designed to reduce these sources of loss as much as possible.

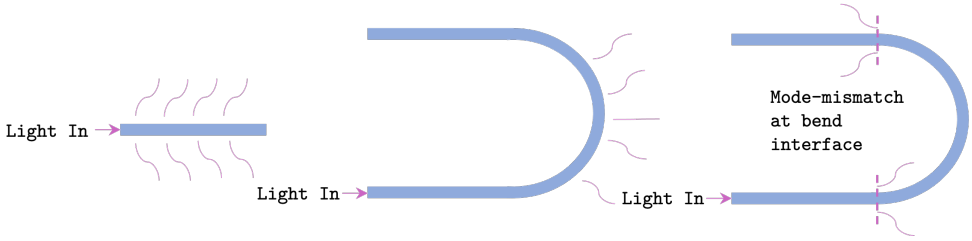

Figure 5.2: Sources of loss in an optical waveguide. Left) loss occurring through light scattering off the rough sidewall of a waveguide, known as sidewall scattering. Center) loss occurring through light travelling out the waveguide instead of following the bend of the waveguide; this is known as radiative loss. Right) loss occurring from the light not being centred in the waveguide after a bend; this is known as mode-mismatch loss.

Simulation

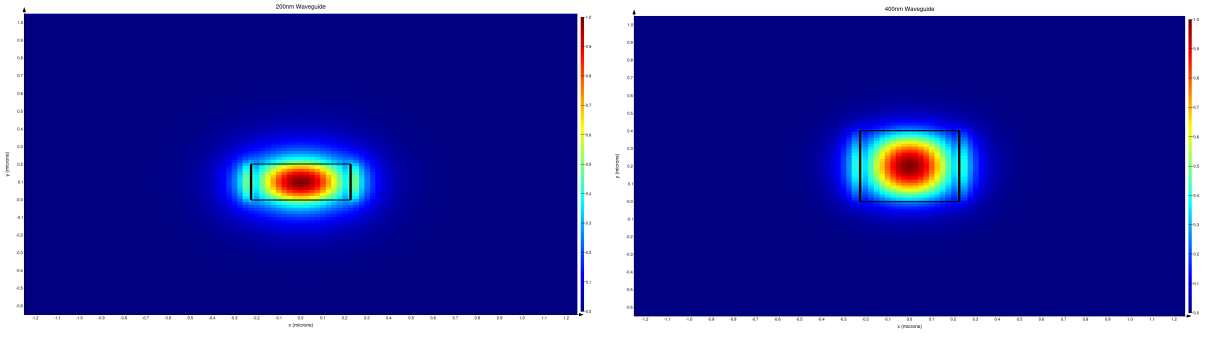

Figure 5.3: Mode profile of the first order TE mode in a 200 nm thick waveguide (left) and a 400 nm thick waveguide (right). Mode profiles were calculated using Lumerical MODE.

Four factors are required to fully define a strip waveguide: height, width, bend radius and Bezier parameters. The foundry usually only offers a single height, but we had a

choice between 200 and 400 nm. As we can observe in Figure 5.3, 400 nm proved to have significantly better mode confinement and appears to be a height offered by many foundries.

The waveguide width could be found by sweeping a range of widths and finding at which point the waveguide is optimized for transmitting the first-order transverse electric (TE) and transverse magnetic (TM) modes. To do this, I calculated both the effective and group indexes at each width using Lumerical MODE (Figure 5.4).

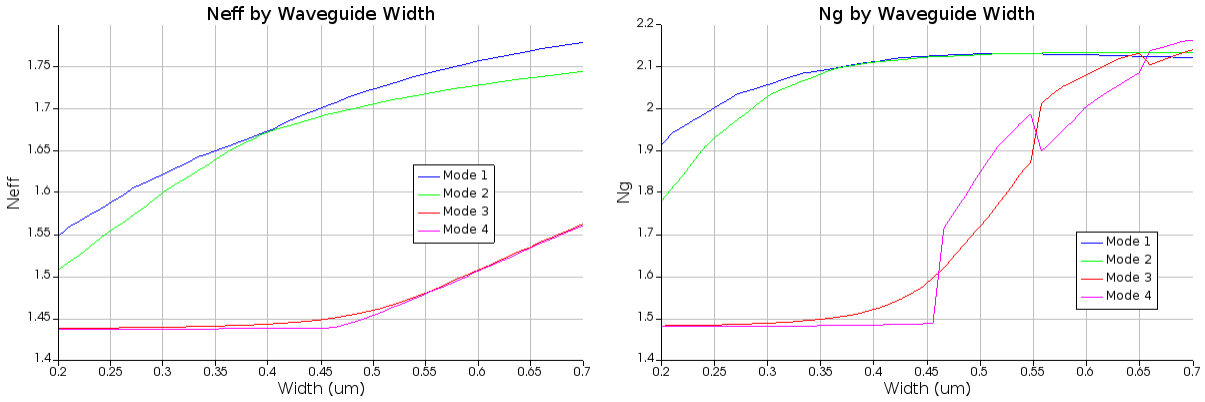

Figure 5.4: Effective (left) and group (right) index of a waveguide at widths between 200 nm and 700 nm for the first four modes. Modes 1 and 2 refer to the first-order TE and TM modes, and modes 3 and 4 are the second-order TE and TM modes. The ideal width is when the difference between the first and second-order modes is widest, in this case 450 nm. The n_{eff} and n_g of the modes was calculated using Lumerical MODE.

From this, it was determined that a width of 450 nm had the most significant difference between the first-order and second-order modes for both group index (n_g) and effective index (n_{eff}). As observed in Figure 5.5, loss for this width is also found to be minimal. It is important to remember that the actual loss per unit length will be significantly higher than the 0.018 dB/cm calculated. Applied nanotools (ANT) foundry in Edmonton, Canada, reports a 1.5 dB/cm for a 750 nm waveguide.

Once the thickness and width of a straight waveguide have been determined, I can move on to determining the bend radius of the waveguide. The total bend loss is calculated using the propagation loss over the bend and the mode-mismatch loss [55].

$$\text{Loss}_{total} = -2 \times 10 \log_{10} \left(\text{Loss}_{propagation}\right) + \left(r_{bend} \times \theta_{bend}\right) \text{Loss}_{mode-mismatch} \tag{5.1}$$

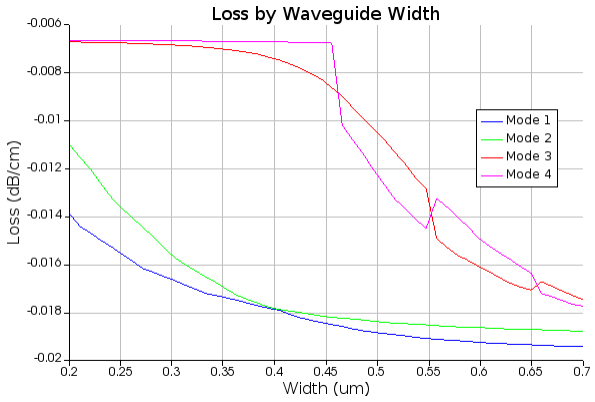

Figure 5.5: The loss of a waveguide at widths between 200 nm and 700 nm for the first four modes. Modes 1 and 2 refer to the first-order TE and TM modes, and modes 3 and 4 are the second-order TE and TM modes. The ideal width is when the difference between the first and second-order modes is widest, in this case 450 nm. The loss of each mode was calculated using Lumerical MODE.

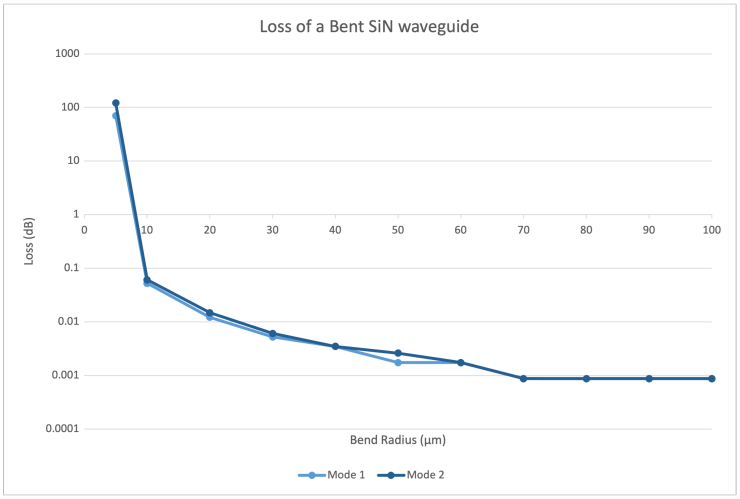

Figure 5.6: Loss of a waveguide over a 90° bend of radii between 5 μm and 100 μm. Values used to calculate loss were found using Lumerical MODE.

It was found that a bend radius of 25 μm had a loss less than 0.01 dB per 90° bend. Again, this is an underestimate, and the actual loss of a bent waveguide will probably be higher. ANT measures the loss of a bent SiN waveguide to be 5 dB/cm for a 750 nm

waveguide of unspecified radius. I can reduce the loss of a bent waveguide even more by introducing a Bezier bend.

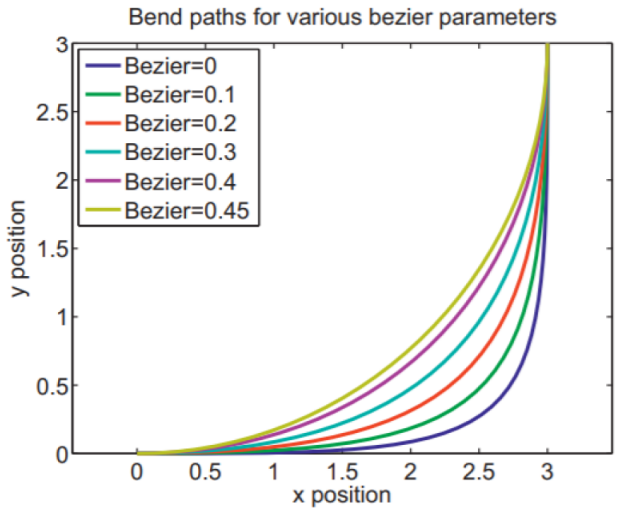

Figure 5.7: Path of the same curve with Bezier parameters between 0 and 0.45 applied to it [6].

A Bezier parameter indicates what path a curve will take. Instead of creating an exact quarter circle, the curve will be shallower, this is shown in Figure 5.7. This adiabatic bending can reduce mode mismatch loss over a curve. It was found that for a 25 μm radius, a Bezier parameter of 0.35 had the lowest loss.

Having found the parameters for a low-loss SiN waveguide, we can use them in our optical chip designs. First, the design needs to be imported into a mask layout software. We will be using Klayout, a free and simple layout software.

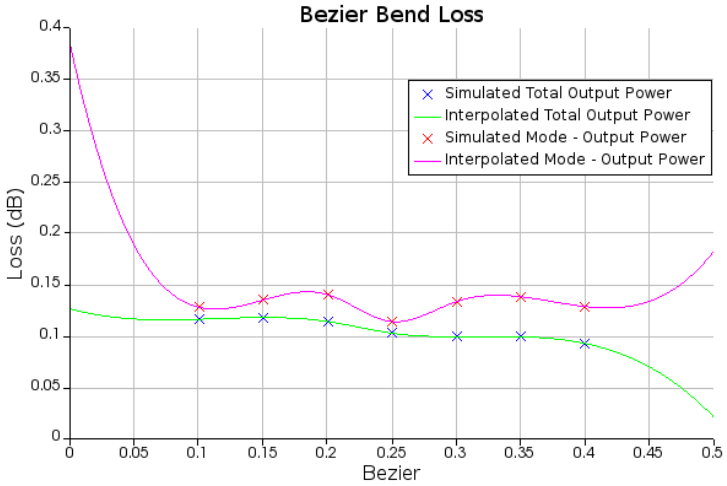

Figure 5.8: loss of a 25 μm curve with Bezier parameters between 0.1 and 0.4 applied to it. Loss simulated and calculated using Lumerical FDTD.

Klayout Integration

Klayout determines how to draw a waveguide using a simple XML lookup file:

```
<waveguides>
<waveguide>
<name>SiN Strip TE 895 nm, w=450nm</name>
<CML>EBeam</CML>
<model>ebeam_wg_integral_895</model>
<bezier>0.25</bezier>
<radius>25.0</radius>
<width>0.45</width>
<component>
<layer>SiN</layer>
<width>0.45</width>
<offset>0.0</offset>
</component>
<component>
<layer>Waveguide</layer>
<width>0.45</width>
<offset>0.0</offset>
```

```
</component>
<component>
<layer>DevRec</layer>
<width>1.45</width>
<offset>0.0</offset>
</component>
</waveguide>
</waveguides>
```

The lookup file contains the parameters found during simulation: “width”, “radius” and “bezier”. As discussed previously, the layer’s thickness is set by the foundry, so it is not explicitly included in the table. However, the layer the waveguide is drawn on is defined under the first component listing. There are two other layer components listed in the table. The “Waveguide” layer is a non-fabricated layer used by KLayout to perform convenient tasks like determining the length of a waveguide section, quickly resizing a waveguide section, and snapping other components to the end of the waveguide. The final layer, “DevRec” is another non-fabricated layer used to determine if the two components in close contact break any design rules the foundry sets. It creates a buffer around the waveguide and alerts the design checker if another component is too close to the waveguide.

Two further lines in the XML file require explanation. The first, “CML” refers to the compact model library within which a model of the waveguide, the name of the model listed under “model”, can be found. This model is used when performing simulations of circuits in a layout. KLayout allows for easy simulation of circuits using a Lumerical Interconnect integration.

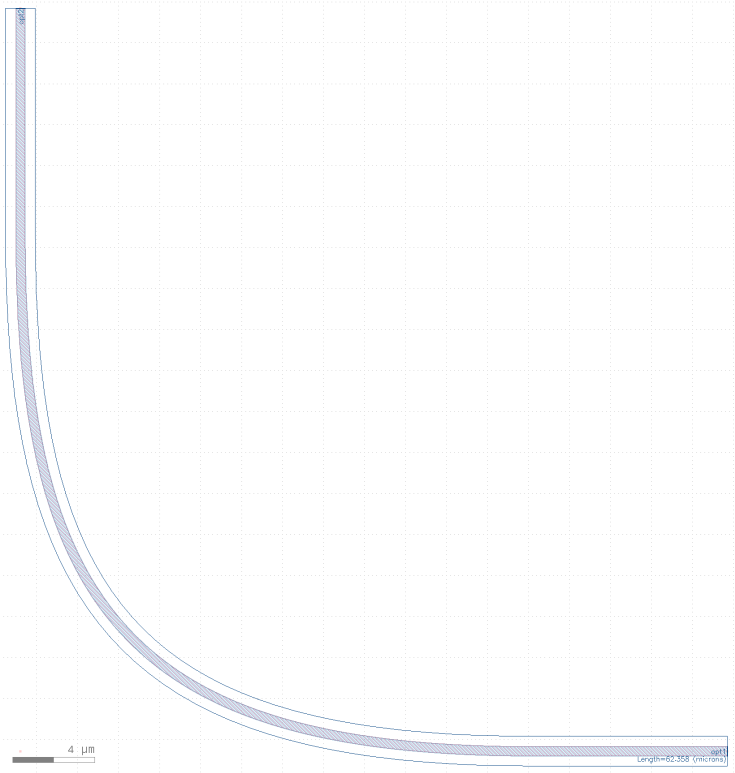

Figure 5.9: Example of a curved waveguide section modelled in KLayout. The length of the section is marked in the bottom right corner, and the ports are marked along the top left and bottom right corners.

Lumerical Integration

Interconnect and the recently available qInterconnect, use compact models to run simulations of collections of components. The compact model contains information on the effective and group index of the material as well as the loss per length.

The model also requires the positions of the ports of the component to be defined. Some components also require a script to calculate information. In the case of a waveguide, the script calculates the length of the waveguide segment and the total loss along that segment. This allows the behaviour of a circuit to be simulated.

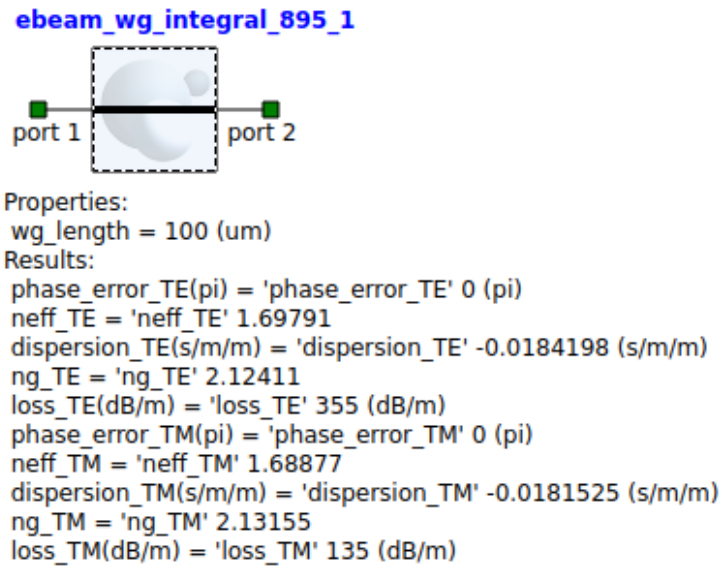

Figure 5.10: Lumerical interconnect icon describing a waveguide section 100 μm in length. The model lists factors like the n_{eff} and n_g of the waveguide for both the TE and TM modes, the loss per unit length, and dispersion. These factors were calculated using the results of Lumerical MODE and FDTD simulations.

5.2 Y-Branch

The second component built was a y-branch. A y-branch takes a single beam of light and evenly splits it into two; it is the integrated analogue of a 50:50 beamsplitter with only one input port.

Simulation

My simulations measure the s-parameters of the component, and I can test for the optimal transmission.

When I input light in port 1, I expect the light to entirely split between ports 2 and 3, leading each to have a transmission of 3 dB. We can observed that this was found in Figure 5.12.

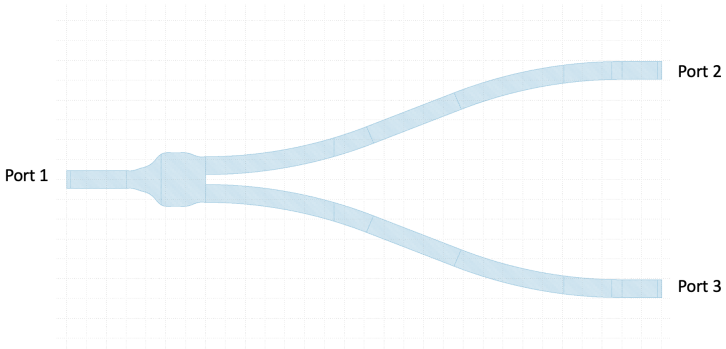

Figure 5.11: Diagram of a y-branch modelled in KLayout. The ports of the component have been marked.

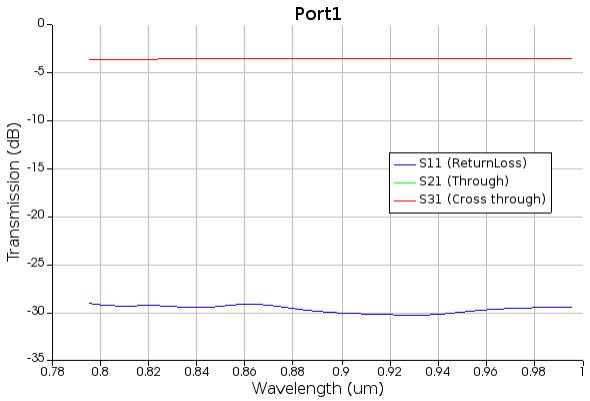

Figure 5.12: Transmission of light input into port 1. At 895 nm, S21 and S31 are approximately 3 dB or about half the input light. A minimal amount of light reflects through port 1. The simulations and calculations were performed in Lumerical FDTD.

Light input into ports 2 or 3 should be primarily exiting through port 1 and a small amount reflecting or crossing into ports 2 or 3 as shown in Figure 5.13.

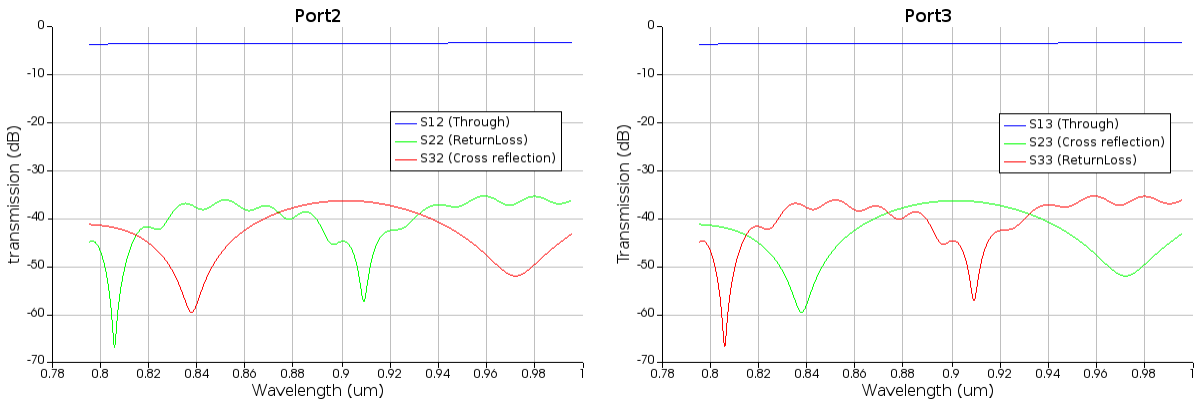

Figure 5.13: Transmission of light input into ports 2 (top) and 3 (bottom), we can observe that transmission through port 1 (S12 and S13) is approximatly 4 dB, and some light is reflected through the input port or to the opposite port. Simulations and calculations for these graphs were done in Lumerical FDTD.

Klayout Integration

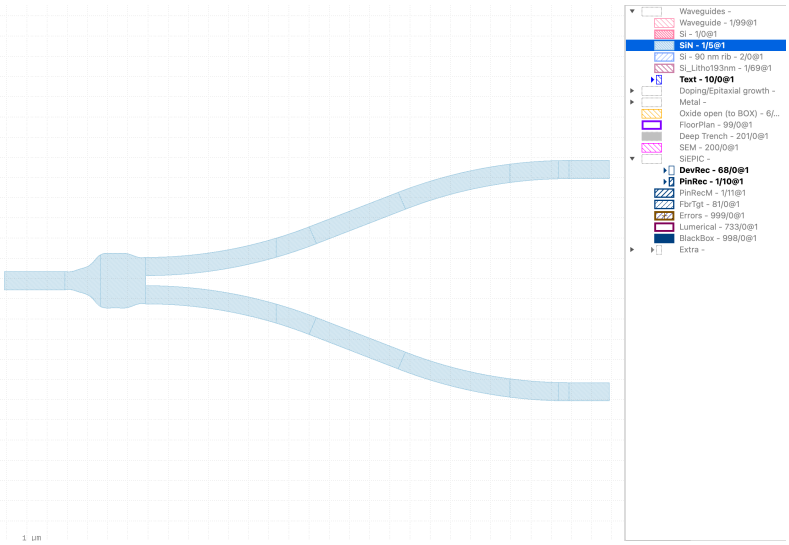

Figure 5.14: SiN layer of a y-branch laid out in KLayout.

Having found a design for a y-branch with optimal transmission values, I can integrate it into KLayout. Since this component is a constant size and shape, it is integrated as a

graphic data system (GDS) file. This file contains the shape of each layer in the component. The first layer is the SiN itself in the shape of the y-branch (Figure 5.14). Next, I defined the DevRec layer (Figure 5.15), which performs the same function discussed in Section 5.1 and creates a box around the waveguide.

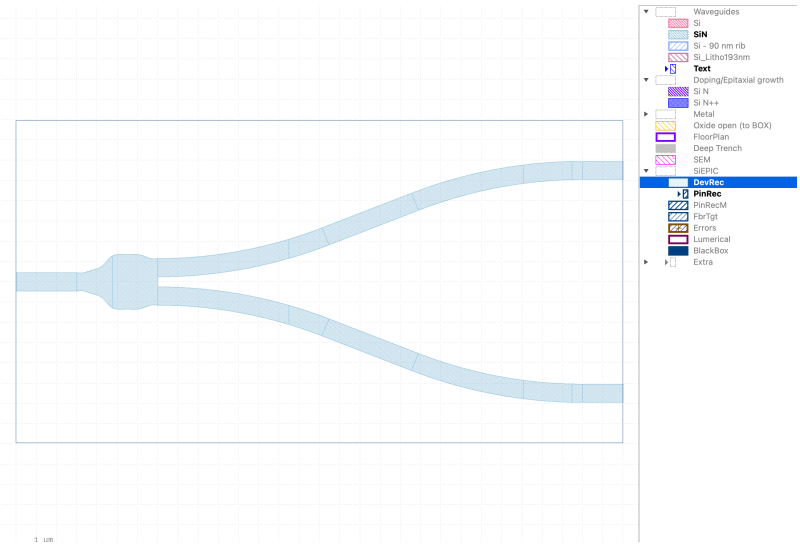

Figure 5.15: DevRec layer of a y-branch laid out in KLayout.

The PinRec layer (Figure 5.16), is a non-fabricated layer that tells KLayout where the ports of the component are and where and how to connect waveguides to the component. The layer must be defined from the inside of the component to the outside so that KLayout will attach the waveguide in the correct direction. Finally, a layer of non-fabricated text (Figure 5.17), is used to label the component to provide information to future users. These layers are saved to a GDS file, which will be called upon every time a user inputs a y-branch into a circuit.

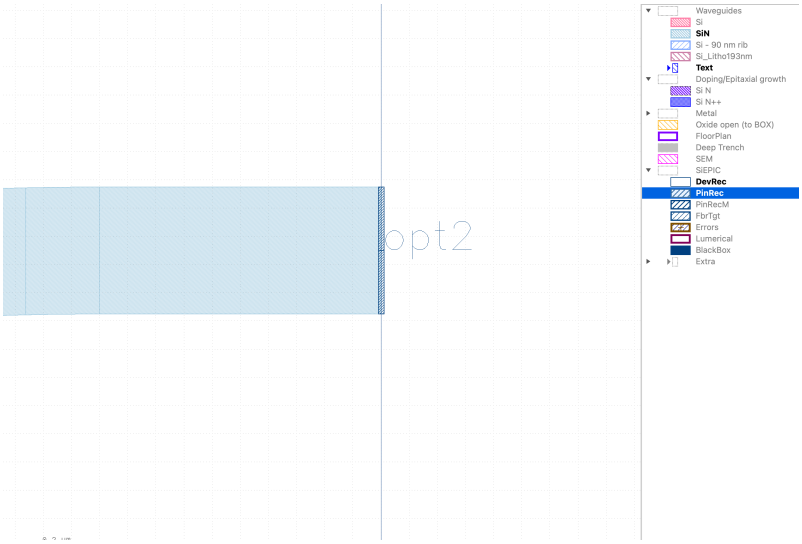

Figure 5.16: PinRec layer of a y-branch laid out in KLayout.

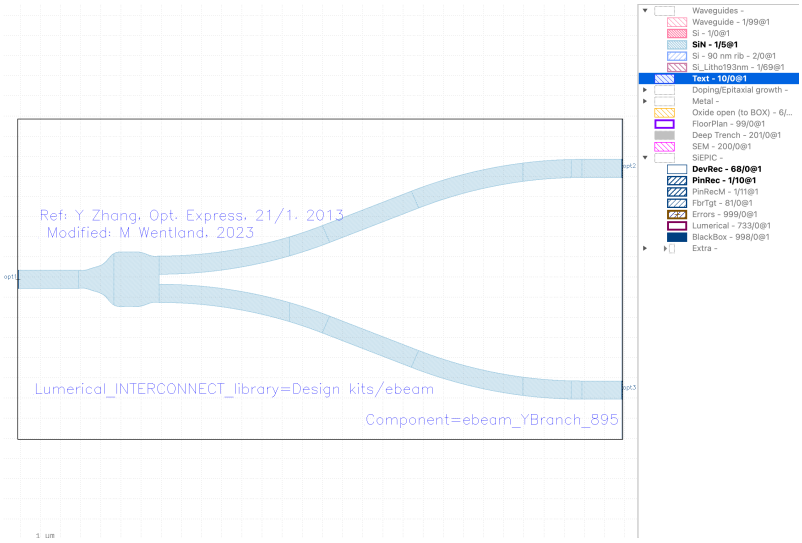

Figure 5.17: Text layer of a y-branch laid out in KLayout.

Lumerical Integration

An interconnect model for the y-branch was also developed and includes information on the s-parameters and ports of the component. This component also requires a simple

script that allows Interconnect to access the s-parameters of each port. This information necessary to determine the behaviour of the component in a circuit and to calculate the loss we can expect from this component.

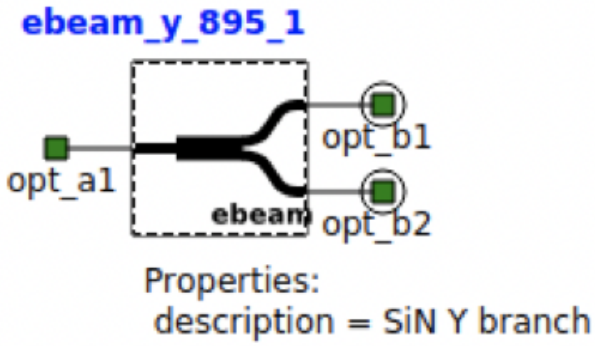

Figure 5.18: Lumerical interconnect icon describing a y-branch.

5.3 Chip Design

With these basic components developed, they need to be tested. I had the opportunity to design the chip in Figure 5.19 in collaboration with canadian microsystems (CMC). This chip was made at the advanced micro foundry (AMF) in Singapore, which had some restrictions that affected the design. Namely, they require all SiN components to be surrounded by a window 20 μm on either side of the component, necessitating a larger turn radius of 45 μm.

The chip was designed to act as a method of unit testing the components. The first set features different lengths of waveguides to determine the loss of a standard waveguide. These tests contain two bends of a standard radius. The next set tests different bend radii, keeping the length of the waveguide constant. Four circuits are dedicated to determining loss per bend, keeping the length of the waveguide the same as the number of turns increases from 2 to 10 turns. Three simple circuits were added to test the s-parameters of the y-branch by maintaining the length of the output waveguides. Finally, a long waveguide with many turns was added to determine if the waveguides would be functional over longer, more

complicated circuits. These chips have been fabricated and returned to our lab, however their behaviour has not yet been tested.

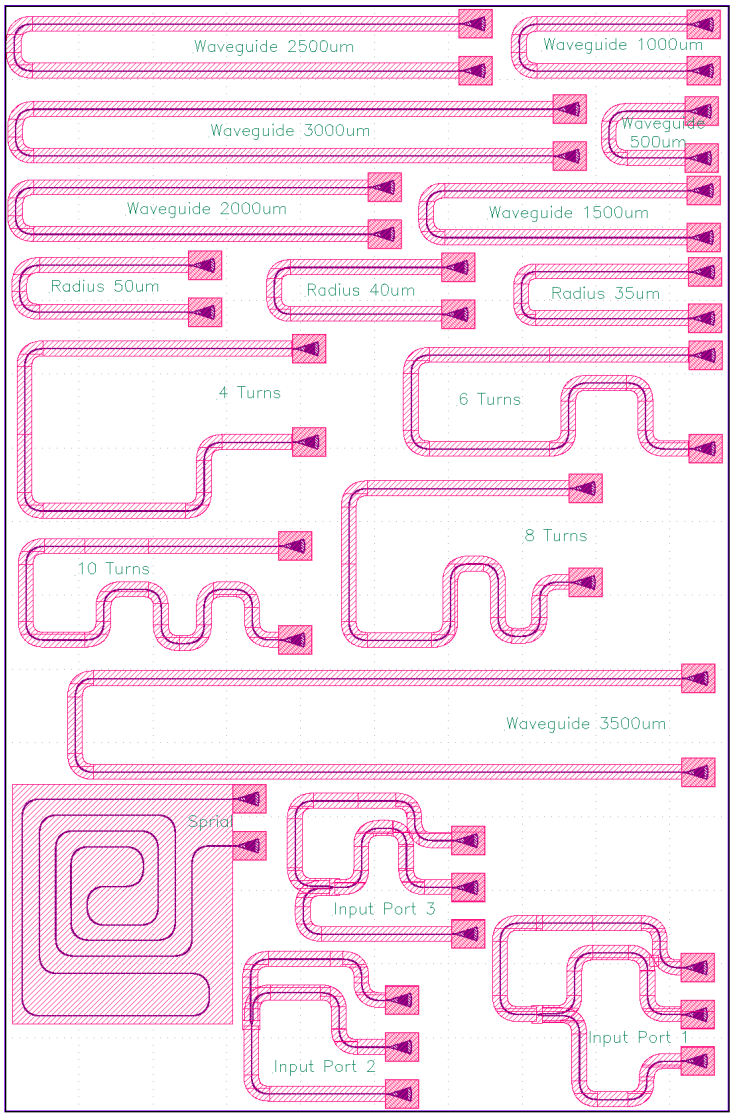

Figure 5.19: Chip design for the AMF foundry taped out in KLayout. There are seven tests of wavelengths between 500 and 3500 μm in length. Three tests of radii of 50 μm, 40 μm, and 35 μm are combined with a test of the same length with a 45 μm radius labelled"Waveguide 1000 um". Four tests are designated to determine loss per bend by increasing the number of bends from 4 to 10. There is also a test labelled "Waveguide 2000um", which is the same length as the turn tests but contains only two turns. Finally, the three tests labelled Input Port 1, 2, and 3 test the transmission of a y-branch by inputting light into one port and measuring the light output from the other two ports.

Chapter 6

Conclusion

Semiconductor quantum dots have the potential to compete with, or even surpass, the performance of SPDC sources as the ideal source of entangled photons. However, there are still issues that have to be overcome, namely the FSS that causes the photons to be released in a time-dependent entangled state. There have been multiple methods used to remove the FSS of quantum dots, but they typically involve further fabrication and cannot be used in conjunction with quantum dots in nanostructures.

In this thesis, I examined an all-optical approach agnostic to the form of the quantum dots. This approach uses the properties of a fast-rotating half-wave plate, which we emulate using an electro-optic modulator. I tested several EOMs to see if they could successfully be used in a FSS removal scheme. I found that not all EOMs perform identically, with our longer devices performing significantly worse (maximum 46.8% efficiency) than our shorter devices (maximum of 88.4% efficiency). We also found that these devices have an optimal frequency range (200-300MHz) in which they are most efficient and that constant adjustments to the DC bias are required to maintain efficiency over an extended operation period.

The differences in these devices are cause for further study to identify why increasing the length of the device might have impacted the performance or if something else might be the reason for the reduction in efficiency such as the cut of the crystal. Improving the stability of the devices is an essential next step; this could be addressed using a duty cycle or an active feedback system. Once a set of functional EOMs has been identified, they can be used in a tomography experiment to see if they can remove the FSS of a quantum dot. Future work could also examine ways to reduce the required voltage as the current design does require the use of high gain (52 dB) amplifier reducing the ease of implementation of

this method.

This thesis also examines a potential use for the entangled photons we create in the form of integrated photonic chips. A small library of silicon nitride components that can be used to build quantum circuits was simulated specifically for photons at the wavelength our quantum dots emit. The components were also integrated into the SiEPIC EBeam library so they can be easily added into a mask layout using the KLayout software. I also used the Lumerical integration to build compact models of my components so simulations of the circuits can be performed with no added effort to the user.

Samples of these components have been fabricated on chips, which can be used to test for both the efficacy and efficiency of the components. From there, the designs can be iterated and perfected until the components have the lowest loss possible. Further components can also be created and added to the library to allow a wide range of circuits to be built. This small library will allow us to build on-chip test structures like the Hong-Ou-Mandel interferometers or quantum teleportation circuits that would otherwise require significant optical table space.

Both of these experiments aim to improve the ease and efficiency of creating quantum circuits and potentially allowing quantum computers with many qubits to be a reality.

References

[1] C. Couteau, "Spontaneous parametric down-conversion," *Contemporary Physics*, vol. 59, no. 3, pp. 291–304, 2018.

[2] M. A. M. Versteegh, M. E. Reimer, K. D. Jöns, D. Dalacu, P. J. Poole, A. Gulinatti, A. Giudice, and V. Zwiller, "Observation of strongly entangled photon pairs from a nanowire quantum dot," *Nature Communications*, vol. 5, p. 5298, 2014.

[3] A. Fognini, A. Ahmadi, S. J. Daley, M. E. Reimer, and V. Zwiller, "Universal fine-structure eraser for quantum dots," *Optics Express*, vol. 26, no. 19, p. 24487, 2018.

[4] T. Garrow, "Resonant excitation of a nanowire quantum dot and optical frequency shifting via electro-optic modulation," Master's thesis, University of Waterloo, 2021.

[5] (2022, June) Why can silicon nitride be an ideal platform for photonic integrated circuits. PhotonDelta. [Online]. Available: https://www.photondelta.com/news/why-can-silicon-nitride-sin-be-ideal-platform-for-photonic-integrated-circuits/

[6] S. Lam, "Waveguide bezier bends," 2021.

[7] O. Darrigol, *A History of Optics*. Oxford University Press, 2012.

[8] H. Kubbinga, "Christiaan huygens and the foundations of optics," *Pure Applied Optics*, vol. 4, pp. 723–739, 1995.

[9] A. B. Arons and M. B. Peppard, "Einstein's proposal of the photon concept," *American Journal of Physics*, vol. 33, no. 5, pp. 367–374, 1965.

[10] A. Einstein, B. Podolsky, and N. Rosen, "Can quantum-mechanical deescriptio of physical reality be considered complete," *Physical Review*, vol. 47, pp. 777–780, 1935.

[11] A. Einstein, M. Born, and H. Born, *The Born-Einstein Letters*. Macmillan, 1971.

[12] E. Schrödinger, "Die gegenwärtige situation in der quantenmechanik," *Die Naturwissenschaften*, vol. 48, pp. 807–812, 1935.

[13] D. G. Cory, R. LaFlamme, E. Knill, L. Viola, T. F. Havel, N. Boulant, G. Boutis, E. Fortunato, S. Lloyd, R. Martinez, C. Negrevergne, M. Pravia, Y. Sharf, G. Teklemariam, Y. S. Weinstein, and W. H. Zurek, "Nmr based quantum information processing: Achievements and prospects," *Fortschritte der Physik*, vol. 48, no. 9-11, pp. 875–907, 2000.

[14] J. M. Gambetta, J. M. Chow, and M. Steffen, "Building logical qubits in a superconducting quantum computing system," *npj Quantum Information*, vol. 3, p. 2, 2017.

[15] C. D. Bruzewicz, J. Chiaverini, R. McConnell, and J. M. Sage, "Trapped-ion quantum computing: Progress and challenges," *Applied Physics Reviews*, vol. 6, p. 021314, 2019.

[16] P. Shor, "Polynomial-time algorithms for prime factorization and discrete logarithms on a quantum computer," *SIAM Journal on Computing*, vol. 26, no. 5, pp. 1484–1509, 1997.

[17] P. W. Shor and J. Preskill, "Simple proof of security of the bb84 quantum key distribution protocol," *Physical Review Letters*, vol. 85, no. 2, pp. 441–444, 2000.

[18] S. Pirandola, J. Eisert, C. Weedbrook, A. Furusawa, and S. L. Braunstein, "Advances in quantum teleportation," *Nature Photonics*, vol. 9, pp. 641–652, 2015.

[19] A. Harrow, P. Hayden, and D. Leung, "Superdense coding of quantum states," *Physical Review Letters*, vol. 92, no. 18, p. 187901, 2004.

[20] W. K. Wootters, "Entanglement of formation of an abritrary state of two qubits," *Physical Review Letters*, vol. 80, no. 10, pp. 2245–2248, 1998.

[21] F. Verstraete and H. Verschelde, "Fidelity of mixed states of two qubits," *Physical Review A*, vol. 66, p. 022307, 2002.

[22] (2021) Tia 568 standard for fiber optics. The Fiber Optic Association Inc. [Online]. Available: https://www.thefoa.org/tech/tia568b3.htm

[23] Process specifications. Applied Nanotools NanoSOI. [Online]. Available: https://www.appliednt.com/nanosoi/sys/resources/specs{_}nitride

[24] W. K. Wootters and W. H. Zurek, "A single quantum cannot be cloned," *Nature*, vol. 299, pp. 802–803, 1982.

[25] N. Sangoard, C. Simon, H. de Riedmatten, and N. Gisin, "Quantum repeaters based on atomic ensembles and linear optics," *Review of Modern Physics*, vol. 83, pp. 33–80, 2011.

[26] *SPDC810*, ThorLabs. [Online]. Available: https://www.thorlabs.com/drawings/67cc418950ad13ac-0EC881E0-D302-F634-CCC240B55E2ACCC4/SPDC810-Manual.pdf

[27] A. Hartmann, Y. Ducommun, K. Leifer, and E. Kapon, "Structure and optical properties of semiconductor quantum nanostructures self-formed in inverted tetrahedral pyramids," *Journal of Physics: Condensed Matter*, vol. 11, p. 5901, 1999.

[28] M. E. Reimer, G. Bulgarini, N. Akopian, M. Hocevar, M. B. Bavinck, M. A. Verheijen, E. P. A. M. Bakkers, L. P. Kouwenhoven, and V. Zwiller, "Bright single-photon sources in botttom-up tailored nanowires," *Nature Communications*, vol. 3, p. 737, 2012.

[29] S. Deshpande, J. Heo, A. Das, and P. Bhattacharya, "Electrically driven polarized single-photon emission from an ingan quantum dot in a gan nanowire," *Nature Communications*, vol. 4, p. 1675, 2013.

[30] P. Senellart, G. Solomon, and A. White, "High-performance semi-conductor quantum-dot single-photon sources," *Nature Nanotechnology*, vol. 12, pp. 1026–1039, 2017.

[31] M. Müller, S. Bounouar, K. D. Glässl, and P. Michler, "On-demand generaton of inditinguishable polarization entangled photon pairs," *Nature Photonics*, vol. 8, pp. 224–228, 2014.

[32] R. Trotta, J. Martín-Sánchez, J. S. Wildmann, G. Piredda, M. Reindl, C. Schimpf, E. Zallo, S. Stroj, J. Edlinger, and A. Rastelli, "Wavelength-tunable sources of eentangled photons interfaced with atomic vapours," *Nature Communications*, vol. 7, p. 10375, 2016.

[33] J. Zhang, E. Zallo, B. Höfer, Y. Chen, R. Keil, M. Zopf, S. Böttner, F. Ding, and O. G. Schmidt, "Electric-field-induced energy tuning of on-demand entangled photon emission from self-assembled quantum dots," *Nano Letters*, vol. 17, pp. 501–507, 2017.

[34] O. Gazzano, S. M. de Vasconcellos, C. Arnold, A. Nowak, E. Galopin, I. Sagnes, L. Lanco, A. Lemaître, and P. Senellart, "Bright solid-state sources of indistinguishable single photons," *Nature Communications*, vol. 4, p. 1425, 2013.

[35] H. Wang, H. Hu, T. H. Chung, J. Qin, X. Yang, J. P. Li, R. Z. Liu, H. S. Zhong, Y. M. He, X. Ding, Y. H. Deng, Q. Dai, Y. H. Huo, S. Höfling, C. Y. Lu, and J. W. Pan, "On-demand semiconductor source of entangled photons which simultaneously has high fidelity, efficiency and indistinguishability," *Physical Review Letters*, vol. 122, p. 113602, 2019.

[36] J. Claudon, J. Bleuse, N. S. Malik, M. Bazin, P. Jaffrennou, N. Gregersen, C. Sauvan, P. Lalanne, and J. Gérard, "A highly efficient single-photon source based on a quantum dot in a photonic nanowire," *Nature Photonics*, vol. 4, pp. 174–177, 2010.

[37] W. Langbein, P. Borri, U. Woggon, V. Stavarache, D. Reuter, and A. D. Wieck, "Control of fine-structure splitting and biexciton binding in $in_xga_{1-x}as$ quantum dots by annealing," *Physical Review B*, vol. 69, p. 161301, 2004.

[38] R. M. Stevenson, R. J. Young, P. See, D. G. Gevaux, K. Cooper, P. Atkinson, I. Farrer, D. A. Ritchie, and A. J. Shields, "Magnetic-field-induced reduction of the exciton polarization splitting in inas quantum dots," *Physical Review B*, vol. 73, p. 033306, 2006.

[39] A. J. Bennett, M. A. Pooley, R. M. Stevenson, M. B. Ward, R. B. Patel, A. B. de la Giroday, N. Sköld, I. Farrer, C. A. Nicoll, D. A. Ritchie, and A. J. Shields, "Electric-field-induced coherent coupling of the exciton states in a single quantum dot," *Nature Physics*, vol. 6, pp. 947–950, 2010.

[40] J. Wang, M. Gong, G. C. Guo, and L. He, "Eliminating the fine structure splitting of excitons in self-assembled inas/gaas quantum dots via combined stresses," *Applied Review Letters*, vol. 101, p. 063114, 2012.

[41] M. Zeeshan, N. Sherlekar, A. Ahmadi, R. L. Williams, and M. E. Reimer, "Proposed scheme to generate bright entangled photon pairs by application of a quadrupole field to a single quantum dot," *Physical Review Letters*, vol. 122, p. 227401, 2019.

[42] P. E. Kremer, A. C. Dada, P. Kumar, Y. Ma, S. Kumar, E. Clarke, and B. D. Gerardot, "Strain-tunable quantum dot embedded in a nanowire antenna," *Physical Review B*, vol. 90, p. 201408, 2014.

[43] C. L. Chuang, *Physics of Optoelectronic Devices*. New York: John Wiley & Sons, Inc., 1995.

[44] R. S. Weis and T. K. Gaylord, "Lithium niobate: Summary of physical properties and crystal structure," *Applied Physics A*, vol. 37, pp. 191–203, 1985.

[45] J. P. Campbell and W. H. Steiner, "Rotating-waveplate optical-frequency shifting in lithium niobate," *IEEE Journal of Quantum Electronics*, vol. qe-7, no. 9, pp. 450–475, 1971.

[46] S. Daley, "Electro-optic rotating half-waveplate for a quantum dot fine-structure eraser," Master's thesis, University of Waterloo, 2019.

[47] M. Kobierski, "Frequency shifting a single photon by electro-optic modulation," Master's thesis, University of Waterloo, 2020.

[48] M. Zeeshan, "Quadrople electric field for erasing fine structure splitting of a nanowire quantum dot entangled photon source," Ph.D. dissertation, University of Waterloo, 2020.

[49] S. Sanna and W. G. Schmidt, "$LiNbO_3$ surfaces from a microscopic perspective," *Journal of Physics: Condensed Matter*, vol. 29, p. 413001, 2017.

[50] A. Fognini. (2018) Pydualdds. [Online]. Available: https://github.com/afognini/PyDualDDS

[51] J. S. Kilby, "Miniaturized electronic circuits," U.S. Patent 3 138 743, June, 1964. [Online]. Available: https://image-ppubs.uspto.gov/dirsearch-public/print/downloadPdf/3138743

[52] P. S. Peercy, "The drive to miniaturization," *Nature*, vol. 406, pp. 1023–1026, 2000.

[53] A. Liu, R. Jones, L. Liao, D. Samara-Rubio, D. Rubin, O. Cohen, R. Nicolaescu, and M. Paniccia, "A high-speed silicon optical modulator based on a metal-oxide-semiconductor capacitor," *Nature*, vol. 427, pp. 615–618, 2004.

[54] A. Politi, M. J. Cryan, J. G. Rarity, S. Yu, and J. L. O'Brian, "Silica-on-silicon waveguide quantum circuits," *Science*, vol. 320, no. 5876, pp. 646–649, 2008.

[55] Bent waveguide analysis. Ansys. [Online]. Available: https://optics.ansys.com/hc/en-us/articles/360042799933-Bent-waveguide-analysis

[56] A. Ahmadi, "Towards on-demand generation of entangled photons with quantum dots," Ph.D. dissertation, University of Waterloo, 2019.

[57] J. Phoenix, "Investigation of photon interactions with semiconductor quantum dot devices for quantum communication applications," Master's thesis, University of Waterloo, 2019.

[58] G. J. S. Varo and E. Pelucchi, "An intuitive protocol for polarization-entanglement restoral of quantum dot photon sources with non-vanishing fine-structure splitting," *Scientific Reports*, vol. 12, p. 4723, 2022.

[59] M. A. Nielsen and I. L. Chuang, *Quantum Computation and Quantum Information*. Cambridge: Cambridge University Press, 2010.

[60] B. A. Saleh and M. C. Teich, *Fundamentals of Photonics*. New York: John Wiley & Sons, Inc., 2019.

[61] L. Chrostowski and M. Hochberg, *Silicon Photonics Design: From Devices to Systems*. Cambridge: Cambridge University Press., 2015.